



저작자표시-비영리-변경금지 2.0 대한민국

이용자는 아래의 조건을 따르는 경우에 한하여 자유롭게

- 이 저작물을 복제, 배포, 전송, 전시, 공연 및 방송할 수 있습니다.

다음과 같은 조건을 따라야 합니다:



저작자표시. 귀하는 원저작자를 표시하여야 합니다.



비영리. 귀하는 이 저작물을 영리 목적으로 이용할 수 없습니다.



변경금지. 귀하는 이 저작물을 개작, 변형 또는 가공할 수 없습니다.

- 귀하는, 이 저작물의 재이용이나 배포의 경우, 이 저작물에 적용된 이용허락조건을 명확하게 나타내어야 합니다.
- 저작권자로부터 별도의 허가를 받으면 이러한 조건들은 적용되지 않습니다.

저작권법에 따른 이용자의 권리는 위의 내용에 의하여 영향을 받지 않습니다.

이것은 [이용허락규약\(Legal Code\)](#)을 이해하기 쉽게 요약한 것입니다.

[Disclaimer](#)

공학박사학위논문

**A Study on Noise Sources Identification and
Characteristics Deduction of High-speed Vehicles using
Sound Visualization and Resolution Optimization**

음장가시화와 분해능 최적화를 통한

고속주행체의 소음원 및 음향특성 도출에 관한 연구

2014년 2월

서울대학교 대학원

산업조선공학부

노 희 민

**A Study on Noise Sources Identification and
Characteristics Deduction of High-speed Vehicles using
Sound Visualization and Resolution Optimization**

음장가시화와 분해능 최적화를 통한
고속주행체의 소음원 및 음향특성 도출에 관한 연구

지도교수 홍 석 윤

이 논문을 공학박사 학위논문으로 제출함

2014년 2월

서울대학교 대학원
산업조선공학부
노 희 민

노희민의 공학박사 학위논문을 인준함

2014년 1월

위 원 장 _____ (인)
부 위 원 장 _____ (인)
위 원 _____ (인)
위 원 _____ (인)
위 원 _____ (인)

Abstract

A Study on Noise Sources Identification and Characteristics Deduction of High-speed Vehicles using Sound Visualization and Resolution Optimization

Noh, Hee-Min

Dept. of Industrial Engineering and Naval Architecture

The Graduate School

Seoul National University

This dissertation presents a study of the localization of major noise sources in a moving vehicle and the deduction of their noise characteristics. In order to localize noise sources in a moving vehicle, a new microphone array was designed on the basis of the beamforming method. The resolution of the array was analyzed from sound-source localization simulations. Validation tests were conducted to identify the locations of noise sources were with a moving vehicle passing-by with horns at specific positions. After the test with the moving vehicle was successfully performed, the process was applied to high-speed trains; the noise map results showed that the majority of noise produced by high-speed trains originates from the front nose, pantograph, inter-coach spacing, and bogie. Then, an improved algorithm was developed for microphone array signal processing to localize the low-frequency noise sources of high-speed trains. The beamforming method does not have high resolution at low frequencies; therefore, it was difficult to derive the aerodynamic noise of the pantograph in the low frequency

region. Thus, a deconvolution method was applied to improve the resolution in the low frequency region, and non-negative constraints and iteration methods were developed to solve the inverse optimization. From the resolution improvement method, the detailed noise sources of the pantograph were derived. Finally, the sound characteristics of the major noise sources in the frequency domain were deduced by transforming the noise maps into the beamforming power spectrum. In order to use the measurement data from the high resolution region, weighting factors were derived with high values in the high resolution region and low values in the low resolution region. The noise characteristics of the front nose were dominant in the low frequency range less than 1000 Hz, and the major difference between the pantograph and its cover occurred at high frequencies greater than 2000 Hz. The noise of the inter-coach spacing section was a tonal sound at frequencies less than 500 Hz. The noise characteristics of the bogies in the leading power car and between car sections were derived; the dominant noise of the bogies was less than 1000 Hz. In conclusion, effective measures that reduce the noise of the main noise sources were proposed on the basis of the results obtained from this research.

***Keywords:* High-speed vehicles, Multiple microphone array, Beamforming, Inverse problem optimization, Sound characteristics deduction, Noise mitigation measures**

***Student Number:* 2009-30282**

Contents

Abstract	i
Contents	iii
List of Tables	v
List of Figures	vi
Nomenclature	xii
1. Introduction	1
1.1 Research background	1
1.2 Review of previous researches	7
1.3 Structure of research	16
2. Noise sources identification of high-speed vehicles	19
2.1 Delay-and-sum beamforming	30
2.2 Microphone array design	54
2.3 Applications and discussions	93
3. Resolution improvement by inverse problem optimization	109
3.1 Resolution improvement algorithm	113
3.2 Algorithm development	127
3.3 Applications and discussions	129

4. Characteristics deduction of main noise sources	141
4.1 Array resolution analysis	146
4.2 Characteristics deduction algorithm	165
4.3 Applications and discussions	171
5. Conclusions	187
5.1 Conclusions	187
5.2 Future works	190
References	193

국문초록

List of Tables

Table 2-1	3 dB bandwidth and maximum side-lobe levels of 96 channel microphone array	92
Table 2-2	Measurement sites and speeds of high-speed trains	99
Table 2-3	Identified noise sources of high-speed trains	108
Table 3-1	Improved source positions of pantograph and bogie	139
Table 4-1	Noise characteristics of main noise sources of high-speed trains at speed of 300 km/h	185

List of Figures

Figure 1-1 Evolution of maximum speed on rails	2
Figure 1-2 Relative strength and speed dependence of railway noise source	3
Figure 1-3 Sound barriers of high-speed rail	6
Figure 1-4 Generation, transmission and radiation of rolling noise	8
Figure 1-5 Configuration of high-speed trains	9
Figure 1-6 Computational fluid-dynamics simulations of high-speed trains	9
Figure 1-7 Microphone array measurement for high-speed trains in wind tunnels test	11
Figure 1-8 On-board measurement of inter-coach spacing and bogie	12
Figure 1-9 Noise measurement of high-speed trains with microphone array	14
Figure 2-1 Time-reversal method	25
Figure 2-2 Inverse method	26
Figure 2-3 Sound propagation and data measurements	30
Figure 2-4 Delay-and-sum of measured data	31
Figure 2-5 Plane wave propagation model	32
Figure 2-6 General beamforming system	33
Figure 2-7 Beamforming power distribution	37
Figure 2-8 Spherical wavefront model	38
Figure 2-9 Moving monopole and Doppler effect	39
Figure 2-10 Moving source driving in straight lines	40
Figure 2-11 Data source and measured data	41
Figure 2-12 Two impulses generated by moving source	42

Figure 2-13 Propagation produced by moving source	46
Figure 2-14 De-Dopplerization concept	49
Figure 2-15 Beamforming problem with sources in moving frame	52
Figure 2-16 Cross array configuration	56
Figure 2-17 Characteristics of cross array	56
Figure 2-18 Planar array configuration	57
Figure 2-19 Characteristics of planar array	57
Figure 2-20 Nested linear arrays	58
Figure 2-21 Vertical nested array	58
Figure 2-22 Cross array for measurements	59
Figure 2-23 Noise map of ICE front power car measured by cross array	59
Figure 2-24 X-shaped microphone array installed beside high-speed railway lines	60
Figure 2-25 Sound map of noise radiation from pantograph	60
Figure 2-26 T-array for measurement	61
Figure 2-27 Sound map picked up by T-array	61
Figure 2-28 Deutsche Bahn spiral array in front of ICE	63
Figure 2-29 Noise map of ICE 3 travelling left to right	63
Figure 2-30 SNCF star-like, double nested microphone array consisting of 73 microphones	64
Figure 2-31 Noise map of Duplex TGV travelling right to left	64
Figure 2-32 3 dB bandwidth and maximum side-lobe level	67
Figure 2-33 Geometry used in deriving far-field beam pattern of simple line array	69
Figure 2-34 Beam patterns for line array	71
Figure 2-35 Amplitude weighting factors as function of position	73
Figure 2-36 Commonly used window functions	74
Figure 2-37 Fourier transform of rectangular window	74

Figure 2-38 Fourier transform of Bartlett window	75
Figure 2-39 Fourier transform of Hanning window	75
Figure 2-40 Fourier transform of Hamming window.....	76
Figure 2-41 Fourier transform of Blackman window	76
Figure 2-42 96-channel rectangular array	78
Figure 2-43 96-channel radial microphone array with same spacing	79
Figure 2-44 96-channel radial microphone array with centralized shapes	79
Figure 2-45 96-channel radial microphone array with dispersed shapes	80
Figure 2-46 Source positions used for performance simulations	81
Figure 2-47 Resolution simulations of 96-channel rectangular array	82
Figure 2-48 Resolution simulations of 96-channel radial array with same spacing	84
Figure 2-49 Resolution simulations of 96-channel radial array with centralized shapes	85
Figure 2-50 Resolution simulations of 96-channel radial array with dispersed shapes	86
Figure 2-51 Design of 96-channel microphone array	87
Figure 2-52 Co-array pattern of 96-channel microphone array	88
Figure 2-53 96-channel microphone array setup	90
Figure 2-54 Resolution test setup	90
Figure 2-55 Results of resolution test at various frequencies	91
Figure 2-56 Workflow chart of noise mapping method	93
Figure 2-57 Vehicle validation test	94
Figure 2-58 Noise maps of moving vehicle	95
Figure 2-59 Microphone array measurement setup	96
Figure 2-60 Microphone locations for noise measurements	98

Figure 2-61	Maximum A-weighted sound pressure levels of high-speed trains at speeds from 150 to 300 km/h	99
Figure 2-62	Differences in A-weighted sound pressure levels of high-speed trains	100
Figure 2-63	Time-history of sound pressure level from pass-by high-speed trains	102
Figure 2-64	Noise sources in sections between cars	102
Figure 2-65	Vertical distribution of sound pressure levels	104
Figure 2-66	Noise maps of leading power car	105
Figure 2-67	Noise maps of between-cars section	105
Figure 2-68	Noise maps of trailing power car	106
Figure 3-1	Concept of point input in source plane and beamformer output in prediction plane	113
Figure 3-2	Concept of deconvolution with nonnegative variables and point spread function	123
Figure 3-3	Sources and prediction planes	123
Figure 3-4	Beamforming method and inverse problem optimization ...	126
Figure 3-5	Resolution improvement process	127
Figure 3-6	Low-frequency noise sources of leading power car	129
Figure 3-7	Low-frequency noise sources of trailing car	129
Figure 3-8	Beampower distribution of high-speed trains	130
Figure 3-9	Distribution of point spread function	131
Figure 3-10	Point spread function at various positions	131
Figure 3-11	Beampower image contours of power car	132
Figure 3-12	Iteration method at initial state	132
Figure 3-13	Iteration method at convergence state	132
Figure 3-14	Number of iterations required for convergence iterations at various frequencies	133
Figure 3-15	Number of iterations for various frequencies	134

Figure 3-16 Comparison of noise maps obtained from beamforming and resolution improvement methods	136
Figure 3-17 Pantograph configuration	137
Figure 3-18 Wind tunnel test results	138
Figure 3-19 Improved resolution of pantograph	138
Figure 4-1 Microphone array measurement of signal from source	153
Figure 4-2 Array and prediction planes	155
Figure 4-3 Resolution in off-axis	156
Figure 4-4 Measurement of passing-by noise	160
Figure 4-5 Weighting factors over distances	161
Figure 4-6 Array response function of 96-channel microphone array	161
Figure 4-7 Microphone array resolution regions	162
Figure 4-8 3 dB bandwidth of degrees off-axis from 0° to 60°	162
Figure 4-9 3 dB bandwidth of degrees off-axis from bottom to top	163
Figure 4-10 Directivity patterns of dipole and quadrupole	166
Figure 4-11 Source positions for simulations	166
Figure 4-12 96-channel microphone array response of monopole source at frequency of 2000 Hz	167
Figure 4-13 96-channel microphone array response of dipole source at frequency of 2000 Hz	168
Figure 4-14 96-channel microphone array response of quadruple source at frequency of 2000 Hz	168
Figure 4-15 Array responses of sound source types	169
Figure 4-16 Workflow of obtaining beampower spectrum	170
Figure 4-17 Microphone array measurement setup	172
Figure 4-18 Aerodynamic noise positions of high-speed trains	174
Figure 4-19 Pass-by noise data of high-speed train	175
Figure 4-20 20 Hz high-pass filtered signal	175
Figure 4-21 Weighting factors at inter-coach spacing	175

Figure 4-22 Weighted signal at inter-coach spacing	175
Figure 4-23 Noise characteristics of front nose of power car	177
Figure 4-24 Aerodynamic drags of frontal nose of high-speed trains	178
Figure 4-25 Noise characteristics of pantograph sections	179
Figure 4-26 Pressure contour in inter-coach spacing	181
Figure 4-27 Noise characteristics of inter-coach spacing	181
Figure 4-28 Side barriers in inter-coach spacing	183
Figure 4-29 Noise reduction in inter-coach spacing	183
Figure 4-30 Noise characteristics of bogie sections	184

Nomenclature

ω	frequency
θ	angle
φ	phase change
α	parameter
λ	wave length
k	wave number
v	speed of moving vehicle
v_0	constant speed
c	speed of sound
M_0	Mach number
$\Delta\tau$	elapsed time
Δt	sampling interval
τ_j	emission time
$\delta(t)$	Dirac delta function
E	expected value
R	correlation matrix
h_m	transfer function
r_m	distance between source and m th microphone
q	source excitation signal
p_m	measured pressure from m th microphone
P	measured pressure in vector form
w_m	scan parameter from m th microphone
w	scan parameter in vector form
b	beamformer output
β	beamforming power
$*_s$	convolution operator
$*_s^{-1}$	deconvolution operator
\circ	Hadamard product
T	point spread function
$\Delta L_{A,eq}$	A-weighted equivalent sound pressure level
$L_{Amax}(v)$	A-weighted sound pressure level at speed of v

1. Introduction

1.1 Research background

High speed rail encompasses a complex reality involving many technical aspects such as infrastructure, rolling stock and operations, as well as strategic and cross-sector issues including human factors and financial, commercial, and managerial aspects. In addition, the high speed rail system combines all these various elements by using the highest level of technology and the most advanced conception for each of them. High speed is a rapidly expanding new transport mode and is often described as the “transport mode of the future”. This is due to the three main characteristics offered to customers and society: safety, capacity and sustainability. In this sense, many countries have developed high-speed rail to connect major cities, including South Korea, China, France, Germany, Italy, Taiwan and Spain. Moreover, the advance of technology leads the increase of the maximum speed in test over 400 km/h as shown in Figure 1-1 [1.1]. In South Korea, the next generation of the high-speed train named HEMU-430X achieved the speed of 421.4 km/h in 2013,

making South Korea the world's fourth country after France, Japan and China to develop a high-speed train running on conventional rail above 420 km/h. However, the maximum operational speed on most high-speed lines is approximately 300 km/h. The environmental noise of a high-speed train is one of the main reasons for the limitation of the maximum speed in operation.

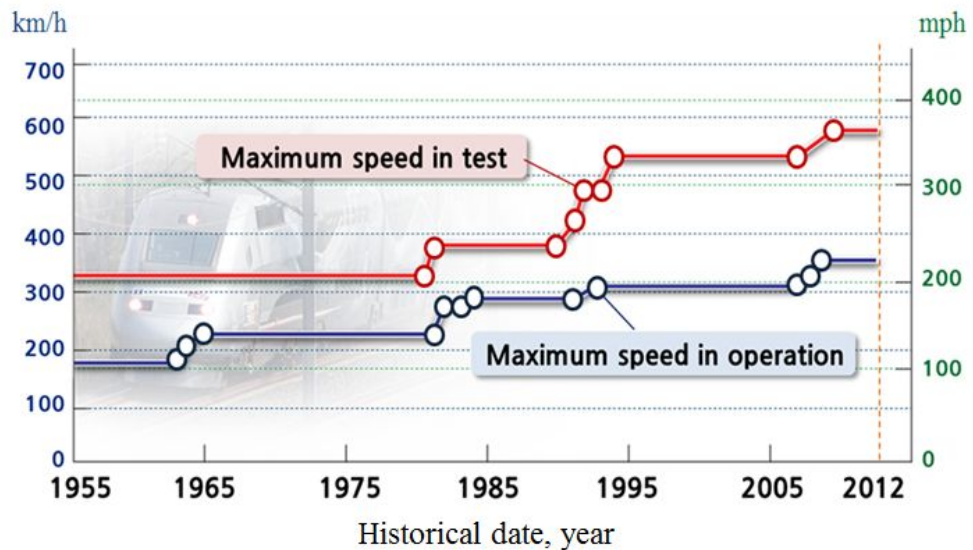


Figure 1-1 Evolution of maximum speed on rails

As train speeds increase, the noise radiation from the trains also increases, eventually leading to unacceptable noise exposure levels to people living near railway lines. Therefore, a better understanding of the noise generating mechanisms is necessary, in order to maintain an environmentally friendly

railway system. Effective noise control measures are only possible with a thorough understanding of the underlying causes of noise generation.

There are two different major noise source mechanisms: rolling noise and aerodynamic noise as shown in Figure 1-2. Rolling noise dominates up to the transition speed, which is approximately 300 km/h; above the transition speed, aerodynamic noise is the more important [1.2]. In other words, aerodynamic noise must be addressed to control noise from high-speed trains.

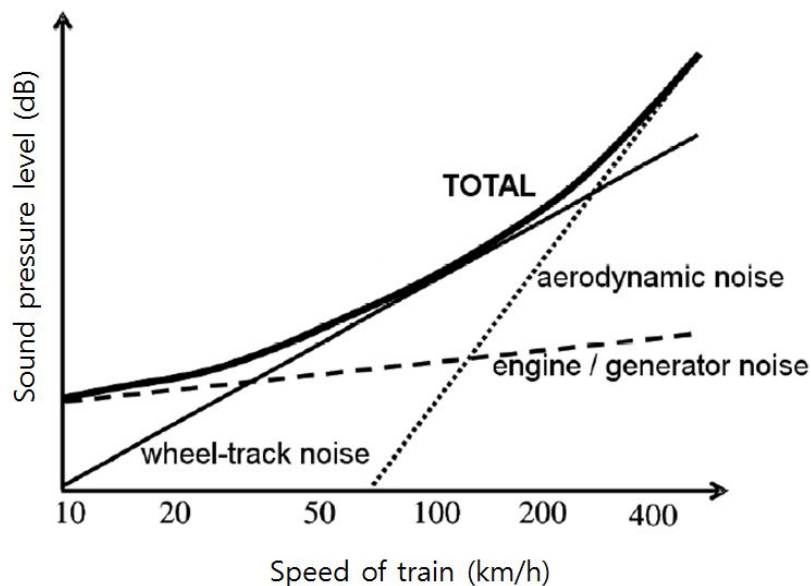


Figure 1-2 Relative strength and speed dependence of railway noise source

The transition speed occurs somewhere between 250 to 340 km/h depending on the train and track system. For instance, a system with very

smooth rail and wheel running surfaces generates less rolling noise than a system with rough running surfaces, emphasizing the importance of aerodynamic noise. Therefore, such a train and track system has a lower transition speed than one with rough running surfaces. The reason why the transition speed may fall within a broad range may also be due to a lack of knowledge of the nature and speed dependence of different noise sources. A noise level increase $\Delta L_{A,eq}$ due to an increase of the speed v may be defined as

$$\Delta L_{A,eq} \sim 10 \log \left(\frac{v}{v_0} \right)^x \quad (1-1)$$

where v_0 is a reference train speed and x is the speed exponent. The speed exponent of rolling noise is approximately 3 and the speed exponent of aerodynamic noise is approximately 6, however, different investigations come up with different values of the speed exponent: Rolling noise: $x = 2.6 - 5.6$, Aerodynamic noise: $x = 4.8 - 7$.

Since the transition speed occurs approximately 300 km/h, where aerodynamic noise becomes predominant, and the speed exponent of

aerodynamic noise is around 6, a speed increase from 300 km/h to 400 km/h leads to a noise level increase of about 8 dB. At high speeds the prediction errors can become substantial if wrong values of the speed exponents are used. So, prediction models describing noise from high-speed trains need to be improved in order to use them at speeds up to 400 km/h. Therefore, studies on rolling and aerodynamic noise are necessary in order to deduce the sound characteristics of a high-speed train.

The first step in noise reduction of a high-speed train is to identify the dominant noise source. There are many different noise sources from a high-speed train, and the dominant source may vary in different situations. After identifying the dominant noise source, the next step is to deduce the noise characteristics to obtain effective noise mitigation measures.

Noise barriers are used for reducing the noise from a high-speed train as shown in Figure 1-3. Noise barriers are an exterior structure designed to protect the inhabitants of sensitive land-use areas from noise pollution and are based on the transmission losses between the incident and transmitted waves

[1.3-1.5]. However, noise barriers may not be effective mitigation measures for a high-speed train for the following reasons. A high-speed train has various airborne low-frequency noise sources. However, the effect of the transmission loss decreases for low frequency noise [1.6]. Therefore, noise barriers are not effective for the low frequency noise of a high-speed train. In this sense, effective noise mitigation measures are required on the basis of the operational noise characteristics generated by a high-speed train



Figure 1-3 Sound barriers of high-speed rail

1.2 Review of previous researches

The various researches about rolling noise, one of the main noise sources of a high-speed train, have been carried out [1.7]. The researches presented about rolling noise mechanisms and sound characteristics. Surface irregularities on wheel and rail running surfaces (roughness) vibration during the wheel/rail contact as shown in Figure 1-4. Vibration of the wheel appears from 1600 Hz, according to its dynamic modal basis. Contribution of the wheel on the acoustic radiation appears mainly between 2000 to 4000 Hz. Wave propagation in the rail induces radiation. Contribution of the rail on the acoustic radiation appears mainly around 1000 Hz. Sleeper radiation appears in a low frequency range up to 400 Hz. The vibration is transmitted by the pads between rail and sleeper. Rolling noise is now well understood and described by simulation software such as TWINS and RIM [1.8]. Due to a large number of model parameters, it is possible to perform detailed studies of the influence of changes of track and wheel designs with respect to the acoustic performance.

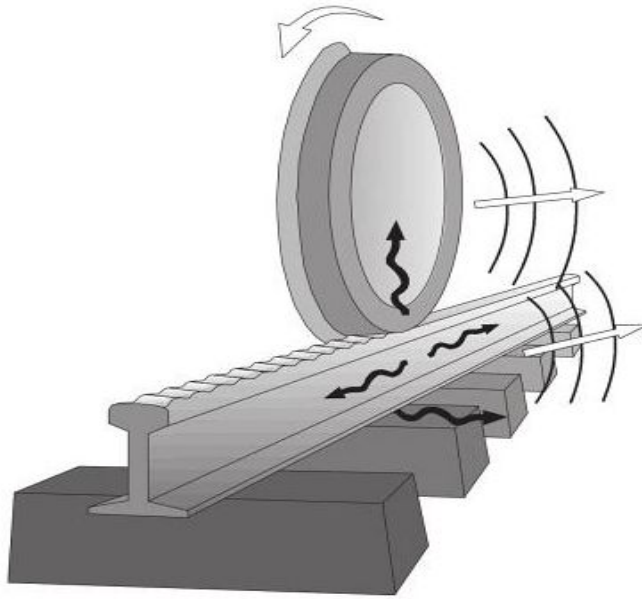


Figure 1-4 Generation, transmission and radiation of rolling noise

However, past studies of aerodynamic noise for high-speed trains are insufficient in contrast to rolling noise. The aerodynamic noise of a high-speed train is scattered in various positions, and its characteristics vary depending on the driving speeds as shown in Figure 1-5. Analytical and experimental approaches were conducted for deriving the sound characteristics of a high-speed train. Computational fluid-dynamics simulations are representative of the analytical method. Wind tunnel tests, on-board measurement, and microphone array system are representative of the experimental methods.

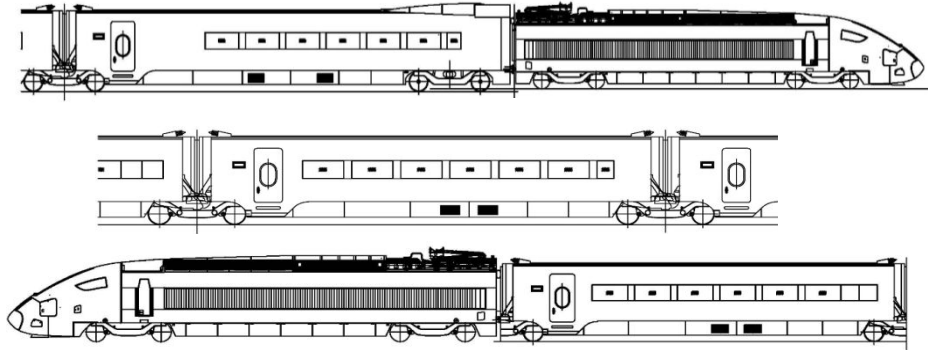


Figure 1-5 Configuration of high-speed trains

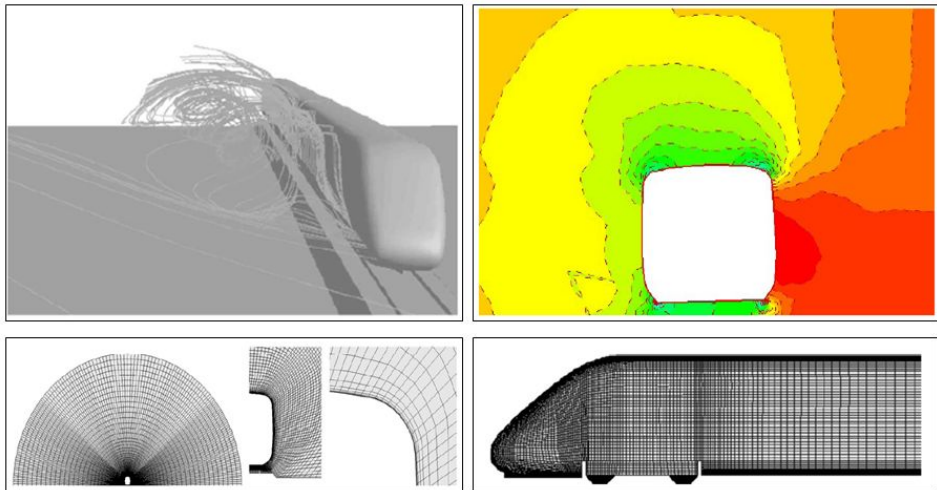


Figure 1-6 Computational fluid-dynamics simulations of high-speed trains
(Upper right: simulation of turbulent flows around the vehicle,
Upper left: simulation of cross-wind effects for high-speed
rolling stock, Lower right and left: grids for the simulation)

Computer fluid dynamics is a branch of fluid mechanics that uses numerical methods and algorithms to solve and analyze problems that involve fluid flows. In addition, computer fluid dynamics is used to perform the calculations required to simulate the interaction of fluids with complex surfaces defined by boundary conditions. Ongoing research has yielded improvements in the accuracy and speed of the complex simulation of turbulent flow, as shown in Figure 1-6 [1.9]. In this sense, this method visualizes flows around a high-speed train; however, it poorly predicts the acoustic characteristics. In order to predict noise with high accuracy, it is necessary to improve the computational techniques on the basis of the noise data obtained from a carefully conducted wind-tunnel experiment that studies basic flow patterns with simple models. Moreover, it is difficult to include the information regarding rolling noise. Therefore, there are significant differences between the operational noise and the predicted noise from computational fluid-dynamics simulations.

A wind tunnel test is a tool used in aerodynamic research to study the effects of the moving solid objects such as a high-speed train. Stable acoustic

signals can be obtained from the wind tunnel test as shown in Figure 1-7 [1.10]; however, it does not contain the rolling noise, as in computer fluid dynamics. Moreover, the maximum speed of a wind tunnel is limited by the laboratory equipment. For example, the maximum speed in the open fields of the wind tunnel in the Korea Aerospace Research Institute is approximately 65 m/s. Therefore, it is difficult to obtain actual operational data from a high-speed train at speeds greater than 65 m/s (234 km/h) from the wind-tunnel test.

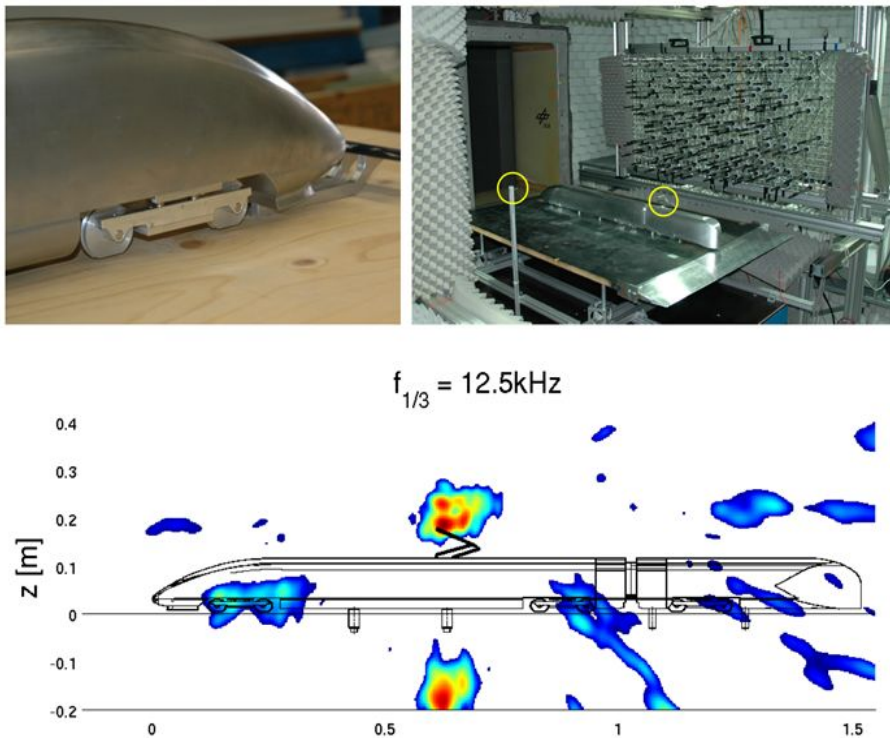


Figure 1-7 Microphone array measurement for high-speed trains in wind tunnel test

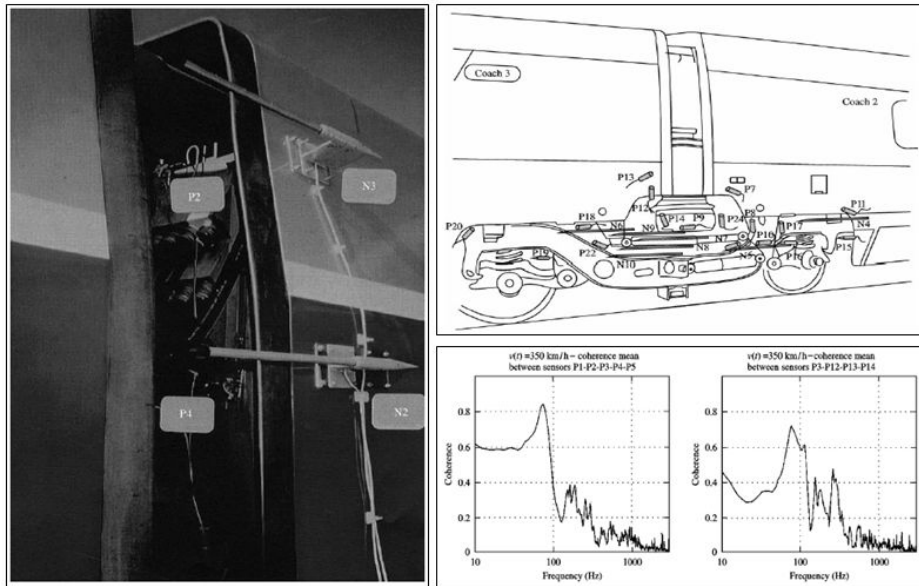


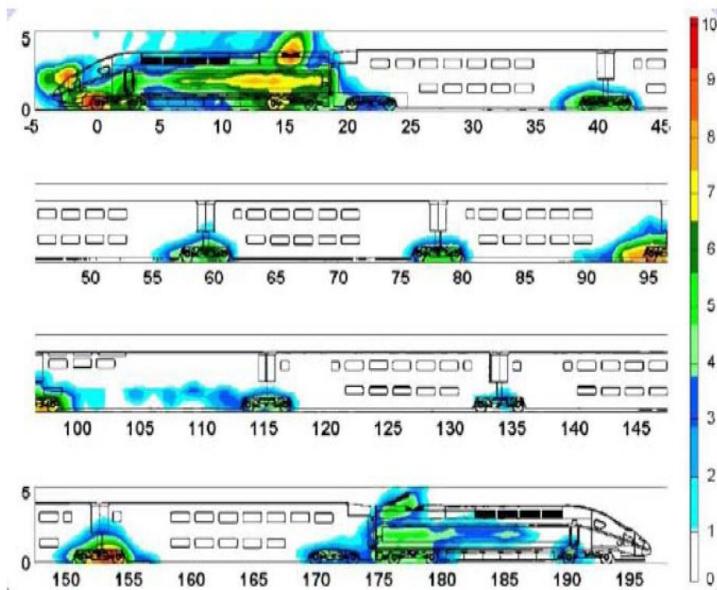
Figure 1-8 On-board measurement of inter-coach spacing and bogie

On-board measurement is a method attaching multiple sensors in a specific position of a high-speed train. It was useful for measuring noise in the specific position such as inter-coach spacing of a high-speed train as shown in Figure 1-8 [1.11]. This method provides effective noise information in various operational environments such as open fields and tunnels. However, the measured noise at a position does not reflect the actual propagation noise at a distance from the measurement position. In the other words, microphones located too close to a source cause errors. Near a large source, the acoustic field will not be representative of the sound propagating to a far field. To avoid

this effect, it is generally found that the source-to-microphone distance should be equal to at least one acoustic wavelength. Moreover, the pantograph has no available position for attaching sensors owing to high voltages greater than 25 kV and high dynamic pressures. The pantograph is the element of the train that collects electrical current from the cable system above catenary to the train motors. The contact force variation can cause contact losses, electric arc formations and sparking.



(1) Noise measurement with microphone array



(2) Noise map of high-speed train

Figure 1-9 Noise measurement of high-speed trains with microphone array

Sound visualization with microphone arrays provides actual noise sources including rolling and aerodynamic noises of a high-speed train. The main advantage of this method used actual operational data including rolling and aerodynamic noises from a high-speed train as shown in Figure 1-9 [1.12]. However, the method did not provide the detailed noise sources of the pantograph owing to various noise sources in close positions. In order to improve the resolution of the noise maps based on the beamforming method, a larger size and more sensors are required, which requires additional cost. In addition, this method only provides the positions of the noise sources and not their characteristics. It is important to know the noise source characteristics as well as their positions in order to establish effective noise reduction measures.

1.3 Structure of research

The purpose of this study is to derive the major noise sources and noise characteristics of a high-speed train to obtain effective noise mitigation measures. At first, a beamforming method was applied to determine the noise sources in a high-speed train. From this method, the main noise sources of a high-speed train were derived. The beamforming method is useful for identifying the locations of the noise sources because the method is based on actual measured noise data. However, the beamforming method has poor resolution at low frequencies; thus, it is difficult to obtain clear noise source images at locations close to noise sources, such as the pantograph. To resolve this problem, the beamforming method was converted into a deconvolution method, which uses additional information such as point spread function that indicates the relationship between the actual sources and the beamforming sources. In addition, resolution weighting functions were deduced to obtain the noise characteristics of the main sources. The weighting function derived from the array response function analysis was applied to the measured signal. The

noise characteristics of the main noise sources were obtained from the frequency conversion. From this process, the noise characteristics of the main sources such as the front, pantograph, inter-coach spacing, and bogie areas were derived. Finally, the measures for noise abatement were proposed on the basis of the results.

1) Originality

The originality of this research is as follows. First, the design of a new microphone array with a radial shape was conducted to identify the noise sources in the high-speed vehicle. An apparatus combined with microphones and a nested array was devised, and the microphone array measurement system including the train speeds was developed. Second, an inverse problem optimization method was applied to obtain an improvement in the resolution for a high-speed train. In this process, the application methods for non-negative constraints were proposed, and iteration equations were derived. Finally, a new method for deducing the noise characteristics at a specific position from pass-by noise measurement was developed. In the process,

weighing factors for the decrease in resolution with respect to distance were applied.

2) Contributions

The contributions of this research are as follows. Noise source identification was conducted for a high-speed train by using beamforming and the resolution improvement. In the process, the main noise sources of a high-speed train at a speed of 300 km/h were presented as the front, pantograph, inter-coach spacing, and bogie areas. Further, more detailed noise sources of the pantograph were proposed from the application of inverse problem optimizations. From this research, the pan head was the main noise source of the pantograph at a speed of 300 km/h. Finally, the noise characteristics were deduced for the main sources of the high-speed trains by using weighting factors. From the results, effective noise mitigation measures were proposed.

2. Noise sources identification of high-speed vehicles

As high-speed trains travel at increasingly higher speeds, the noise that they produce also increases. The noise from aerodynamic sources increases more rapidly with increasing speed. Aerodynamic noise sources are present in various parts of a high-speed train, such as the pantograph and inter-coach spacing.

Wind tunnel tests were widely used in order to study the characteristics of the aerodynamic noise generated from the high-speed train [2.1, 2.2]. The effects of aerodynamic flows moving the train were investigated from small-scaled models in the wind tunnel test. However, real phenomena should be inferred by the similarity theory in the wind tunnel test, which causes errors. For example, rolling noise from the wheel/rail contacts and aerodynamic noise from the turbulent flows are mixed in the bogie area; therefore, the exact noise characteristics of the bogie were not confirmed from the wind tunnel test.

The experimental approaches such as direct and indirect measurements methods were used in order to identify the information about the noise

generated from a high-speed train. The direct measurement method is to attach a microphone-type probe to a vehicle, to record a stationary signal with this probe and to analyze this signal in order to extract its acoustic part. The advantage of this approach is the availability of long time series and thus the statistical advantage. However, its main disadvantage is that the measured signal is not purely acoustic. It has an aerodynamic component generated from the fluctuating part of velocity field. Moreover, the positions that can be measured are limited in a high-speed train. For example, it was not possible to install sensors in the frontal and pantograph areas of the high-speed vehicle owing to the high-voltage power and turbulent flows, respectively. In this sense, the direct measurement method was only used to identify noise characteristics in bogie and inter-coach spacing regions. N.Fremion *et al.* [2.3] proposed spectral characteristics of the inter-coach spacing and the bogie region. In order to compensate for the measured results, the coherent output power spectrum and the noise-to-signal ratio analysis were conducted in this paper. However, as mentioned above, the measurement positions from direct

methods are restricted; thus, the information regarding the other main noise sources was not mentioned. Moreover, the measured results close to the source of noise exhibited only the local characteristics around the source; therefore, the actual characteristics were not identified in the direct measurement method.

In order to overcome the limitations of the direct measurement method, the indirect measurement method was used. The indirect measurement approach consists of placing a microphone or an antenna on the ground to measure the noise level when the vehicle is passing. The indirect measurement with a microphone provides sound pressure levels and characteristics at the measurement position, but does not information about locations of the source on the vehicle. Therefore, the sound visualization technique is useful in order to derive the location and characteristics of the noise source in the moving vehicle.

The near-field acoustic holography, beamforming, inverse, and time-reversal methods can all be used to visualize noise by using multiple microphones. Near-field acoustic holography is a method that is used to

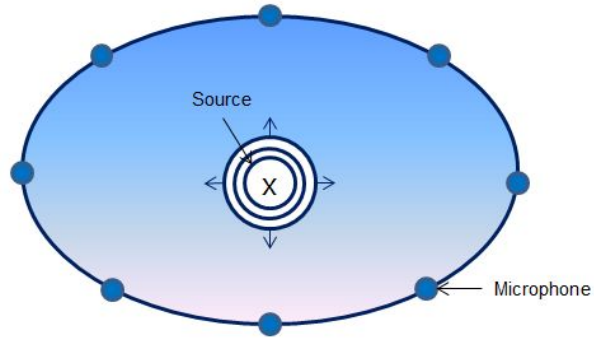
estimate the sound field near a source by measuring acoustic parameters away from the source via an array of pressure and/or particle velocity transducers [2.4, 2.5]. The measuring techniques included in acoustic holography are becoming increasingly popular in various fields, most notably in those of transportation, vehicle and aircraft design, and NVH (noise, vibration, and harshness). C.Pezerat *et al.* [2.6] identified vibration sources from radiated noise measurements by using acoustic holography and the force analysis technique. J.H.Jeon *et al.* [2.7] proposed a mean to use the method to localize moving periodic impulsive source that is embedded by noise by using the moving frame acoustic holography method. However, the measured signals would be affected by the turbulent flow if microphones were installed in the near field at the source. Therefore, it is not reasonable to use this method because the noise sources in a high-speed train are distributed throughout the train.

Beamforming is a signal processing technique that is used in sensor arrays for directional signal transmission or reception [2.8, 2.9]. This is achieved by

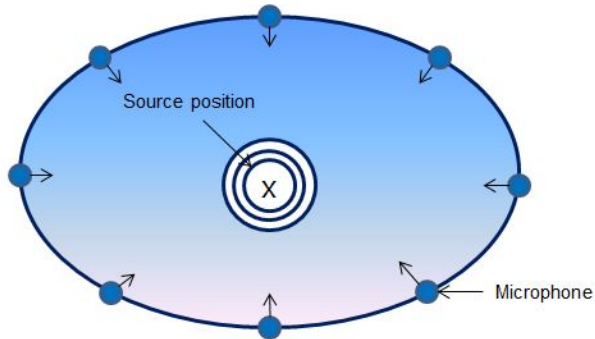
combining elements in the array in such a way that signals at particular angles experience constructive interference while others experience destructive interference. Beamforming can be used at both the transmitting and receiving ends for achieving spatial selectivity. H.Kook *et al.* [2.10] used a delay-and-sum beamformer approach to detect noise source locations on a vehicle. Moreover, the beamforming method is widely used because of its robustness to noise and the ability to locate microphone antennas in the far-field of the source region. However, application of the beamforming method in practice is time-consuming and costly because many sensors are usually required to improve the resolution. Moreover, this method has a lower resolution in the low frequency region.

In a non-dissipate, heterogeneous propagation medium, the pressure field satisfies the acoustic wave equation, which is time-reversal invariant as shown in Figure 2-1. Time-reversal uses the fact that the time-reversed sound wave is also a solution of the wave equation [2.11, 2.12]. The time-reversal process generates the superposition of a convergent wave, which is the exact time-

inverted replica of the initial sound pressure, and a divergent wave emitted at the initial source position after the focus of the convergent wave. Because both the spherical converging and diverging waves are singular at the sound source, this interference places a fundamental limit on the spatial resolution achievable by the classical time-reversal method. The time-reversal acoustic sink concept has the potential to overcome this limitation. The idea is to superimpose the sound field of an “acoustic sink” on the sound pressure. This acoustic sink acts to continuously cancel the emission of the diverging wave. One advantage of the time-reversal approach is that it requires a limited number of sensors in the case of reverberant environments. On the other hand, the numerical models needed to simulate the back-propagation process need to be fairly elaborate. Inverse methods and time-reversal approaches can be implemented with relatively few sensors but generally require a fairly elaborate source.



(1) Propagation step



(2) Reconstruction step

Figure 2-1 Time-reversal method

The inverse method is used to calculate an optimization problem to estimate the location of a source based on the measured signals and microphone locations as shown in Figure 2-2 [2.13-2.15]. However, it is known that the inverse problem is easily ill-conditioned and is sensitive to measurement results. To prevent this sensitivity to errors and uncertainties, it is possible to

regularize the inverse problem using Tikhonov regularization. However, the selection of the regularization parameter is one of the main difficulties in Tikhonov regularization. Several approaches have been proposed to properly choose the regularization parameter in the Tikhonov regularization method, based on singular value decomposition [2.16], the G matrix condition number [2.17], Picard condition [2.18], and L-curve [2.19]. An application of the inverse solution was shown in a case involving unsteady blade lift and unsteady velocity distributions on the surface of a subsonic axial fan [2.20].

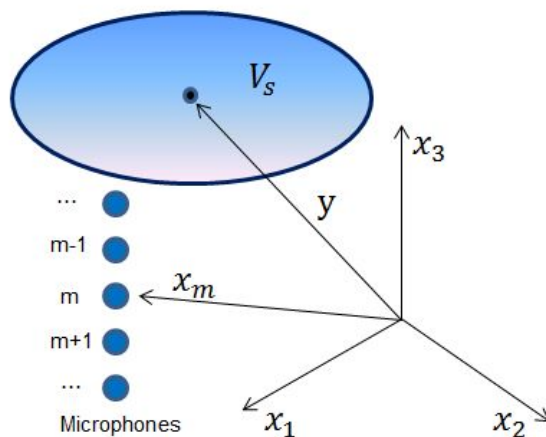


Figure 2-2 Inverse method

Noise source visualization provides useful information for reducing noise measures in a variety of fields. For example, the sound visualization of complex equipment is useful for reducing noise by monitoring system in shipbuilding engineering. The sound visualization for moving objects is also a useful way for indicating the location of noise generated from the vehicles, which is essential for obtaining effective noise reduction measures. The majority of the research on the noise from high-speed trains and the development of the microphone array measurement technique were conducted in the German-French projects DEUFRAKO K and K2 during the 1990s [2.21, 2.22]. At the beginning of the 2000s, multichannel data acquisition systems had become relatively inexpensive, which allowed for the use of microphone arrays and configurations with more channels and complex configurations. The higher channel count of these systems allowed them to produce much higher quality sound maps, owing to a better resolution and spatial dynamic range. These properties are crucial for characterizing the noise sources on high-speed trains.

Recently, Deutsche Bahn developed a microphone array consisting of 90 microphones in a spiral-like configuration with a diameter of 4 m [2.23]. This irregular microphone configuration was chosen to optimize the resolution and dynamic range of the noise sources from a passing high-speed train in the frequency range of interest, roughly 200 ~ 3150 Hz. SNCF also developed a star-like microphone configuration [2.24]. They reported results using 73 microphones in a nested double star to cover a frequency range of 315 ~ 4000 Hz. Both systems used classical delay-and-sum beamforming, which was necessary for focusing on the high-speed moving sound sources.

The need for research regarding the noise of the high-speed train in South Korea is increasing. Thus, the development of an efficient and appropriate array is necessary for the operating environment of South Korea, which has tunnels and short distances between stations. Therefore, in this chapter, noise sources identification of a moving vehicle with multiple noise sources was conducted. The theory of the delay-and-sum beamforming method about moving sources was introduced in Section 2.1. The Doppler effect about

measurement signals should be corrected in order to visualization about the moving sources. To obtain an effective sound visualization for a moving source, a formula derivation for the beam power of the source in the time domain was conducted. Effective microphone array design from the resolution concept was explained in Section 2.2. Optimal array configuration was derived from resolution simulations about various array shapes for design of a new microphone array. Verification of the sound visualization algorithm was performed in Section 2.3. Resolution of designed microphone arrays was investigated with a specific stationary monopole noise and sound visualization test for a moving vehicle attached with specific noise sources was conducted. After the verification test, noise sources identification of the high-speed train was conducted.

2.1 Delay-and-sum beamforming

Beamforming is an array-based measurement technique for sound source localization from the medium to long measurement distance. The principle of beamforming is best introduced through of the basic delay-and-sum beamformer. When we measures the noise generated from a sound source with multiple microphones, the time delay for each sensor should be considered. This method is called delay and sum beamforming method. In this section, the theory of the delay-and-sum beamforming method was presented specifically.

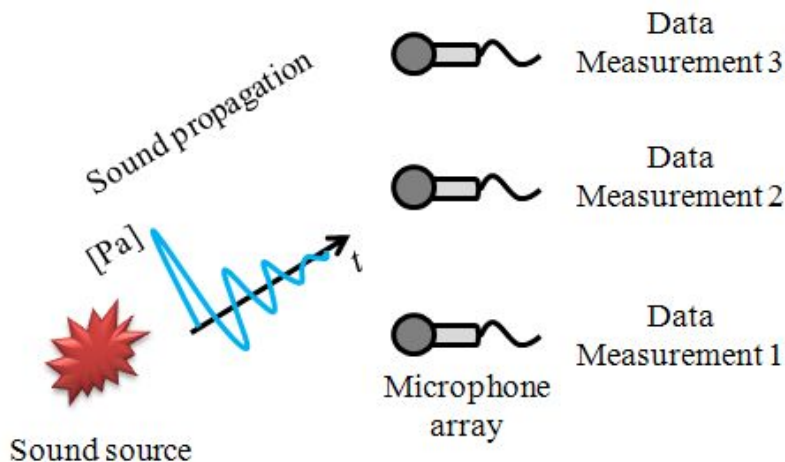


Figure 2-3 Sound propagation and data measurements

When propagated signal from an arbitrary source is measured by sensors of an array as shown in Figure 2-3, the output signals from sensors may be

aligned with specific time delays. Those time delays are determined by distance between the positions of source and sensors. If the delay is adjusted by the position of source, the sum of output signals is reinforced and their wave form is similar that of source as shown in Figure 2-4. This sum is called delay and sum beamformer output.

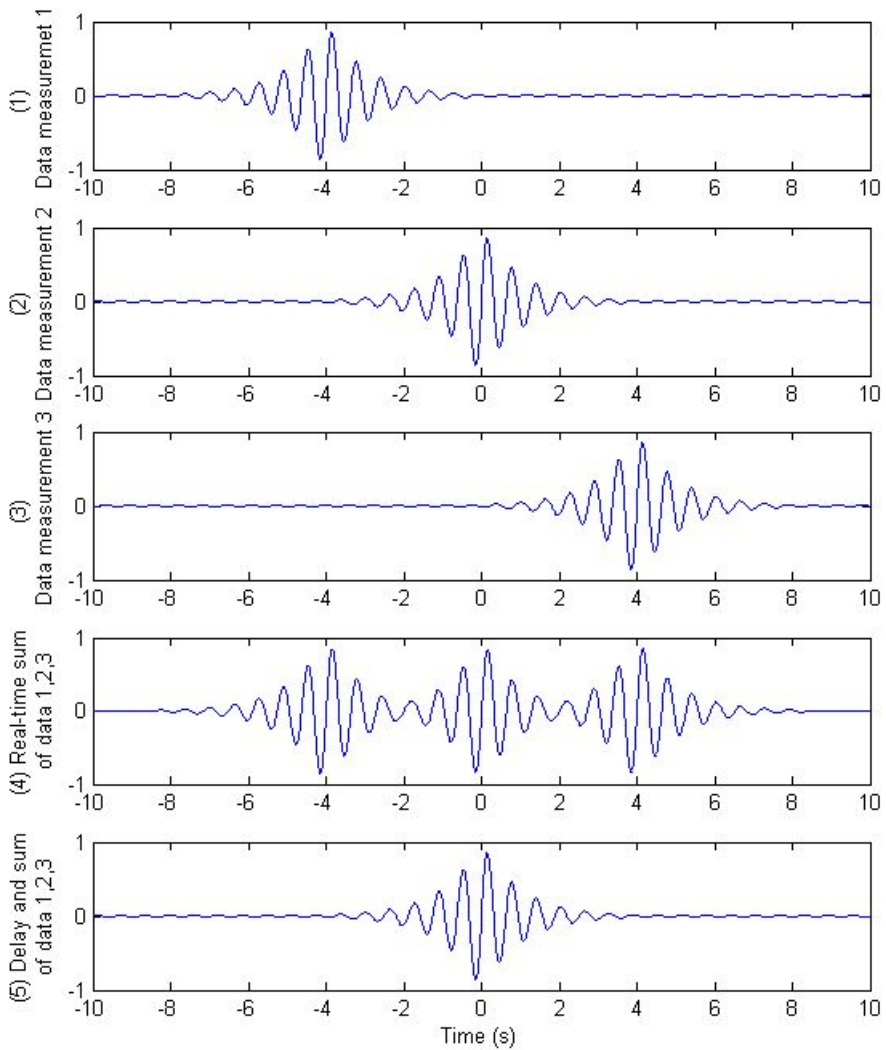


Figure 2-4 Delay-and-sum of measured data

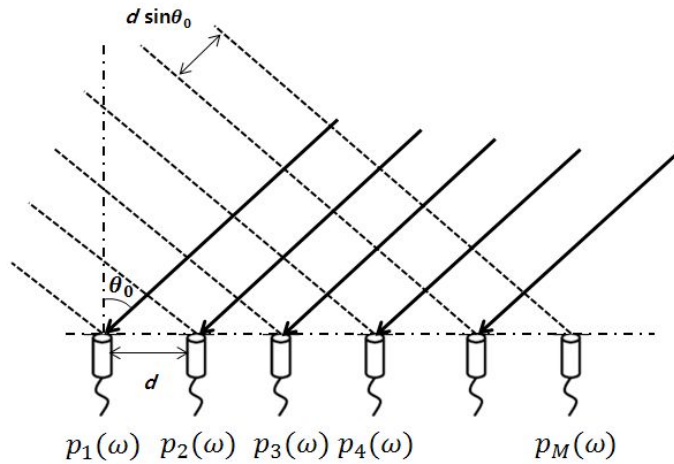


Figure 2-5 Plane wave propagation model

To explain the delay-and-sum concept [2.25] in more detail, consider a pure-tone sound field of frequency ω that is measured by M microphones linearly arranged in space as shown in Figure 2-5. The measured complex pressure field can be expressed in vector form as

$$\mathbf{p}(\omega) = [p_1(\omega) \ p_2(\omega) \ \cdots \ p_M(\omega)]^T \quad (2-1)$$

where the superscript T represents the transpose of a vector or matrix.

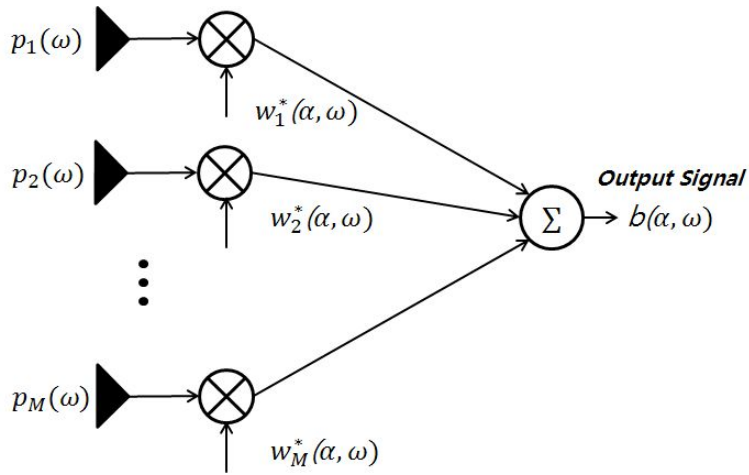


Figure 2-6 General beamforming system

This field contains information about the wavefront propagated from a single sound source or a set of sources as shown in Figure 2-6. The beamforming method assumes that the wavefront can be expressed by a combination of parameters. A simple way to extract a certain parameter α from the given measurement data is to utilize a scan vector that depends on α :

$$\mathbf{w}(\alpha, \omega) = [w_1(\alpha, \omega) \ w_2(\alpha, \omega) \ \cdots \ w_M(\alpha, \omega)]^T \quad (2-2)$$

Using the defined scan vector and measured pressure signals, the beamformer output can be defined as

$$b(\theta, \omega) = \mathbf{w}(\theta, \omega)^H \mathbf{p}(\omega) \quad (2-3)$$

with superscript H being the Hermitian transpose (complex-conjugate transpose) of a matrix.

The expected value of the squared beamformer output is called the beamforming power. The beamforming power is a useful measure for visualizing the sound power distribution at the assumed source locations. From (2-3), the beamforming power can be written as

$$\begin{aligned}\beta(\theta, \omega) &= E[|b(\theta, \omega)|^2] \\ &= \mathbf{w}(\omega)^H \mathbf{R}(\omega) \mathbf{w}(\omega), \quad \text{where } \mathbf{R}(\omega) = E[\mathbf{p}(\omega) \mathbf{p}(\omega)^H] \quad (2-4)\end{aligned}$$

The expectation operator E is introduced here to express the expected value when the measured signal is a random variable.

It is also noteworthy that the structure of \mathbf{R} in (2-4) also determines the performance of the selected beamforming. Each element \mathbf{R} represents the correlation of two microphone signals in the frequency domain. That is,

$$[\mathbf{R}(\omega)]_{(m,n)} = E[p_m(\omega) p_n(\omega)^*] \quad (2-5)$$

which is equivalent to the correlation of two random process p_m and p_n .

Accordingly, the $M \times M$ matrix \mathbf{R} is called a correlation matrix of the

measured signal.

The scan vector is designed such that the assumed that wavefront can be generated by a model source at a specific location. The parameter α can be any variable related to the location of a modeled sound source. For example, if we want to know the angle of a plane wave source, then such a scan vector could be

$$w_m(\theta, \omega) = \frac{1}{\bar{w}} e^{-ik(m-1)d\sin\theta} = \frac{1}{M} e^{-i\omega\Delta\tau(m-1)\sin\theta} \quad (2-6)$$

where m is the index of each microphone ($m=1, \dots, M$). Here, $\Delta\tau = d/c$ indicates the time elapsed for a sound wave to travel one microphone spacing d . Therefore, the scan vector represents a time delay operator that delays each microphone signal by a different amount ($\tau = \Delta\tau(m-1)\sin\theta$). Dividing by the total number of microphones ($\bar{w} = M$) normalize the scan vector such that the beamforming result is invariant with respect to M .

The complex pressure signal of a plane signal of a plane wave source measured at the m th microphone is given by

$$p_m(\omega) = q(\omega) e^{-i\omega(m-1)\left(\frac{d}{c}\right)\sin\theta_0}$$

$$= q(\omega)h_m(\theta_0, \omega) \quad (2-7)$$

where $q(\omega)$ is the amplitude of a plane wave source and often called the source excitation signal. The transfer function between the m th microphone signal and the source excitation q is denoted by $h_m(\theta_0, \omega)$. When the measured signal is multiplied by the scan vector of (2-6) and (2-7), the beamformer output in the direction θ can be written as

$$b(\theta, \omega) = \sum_{m=1}^M p_m(\omega)w_m(\theta, \omega)^* = \frac{q(\omega)}{M} \sum_{m=1}^M e^{-i\omega(m-1)\left(\frac{d}{c}\right)(\sin\theta_0 - \sin\theta)} \quad (2-8)$$

Using the trigonometric identity

$$\sum_{m=0}^{M-1} e^{-im\Omega} = \frac{\sin\left(\frac{M\Omega}{2}\right)}{\sin\left(\frac{\Omega}{2}\right)} e^{-\frac{i(M-1)\Omega}{2}}, \quad (2-9)$$

the beamformer output can be reduced to

$$b(\theta, \omega) = \frac{q(\omega)}{M} \frac{\sin(M(\sin\theta - \sin\theta_0)\varphi)}{\sin((\sin\theta - \sin\theta_0)\varphi)} e^{-i(M-1)(\sin\theta - \sin\theta_0)\varphi} \quad (2-10)$$

where $\varphi = \frac{\omega d}{2c}$ is the phase change after the wave had traveled a distance $d/2$. If φ is small, i.e., d is much smaller than wavelength, then the beamformer output can be approximated by

$$b(\theta, \omega) \approx q(\omega) \text{sinc}(M(\sin\theta - \sin\theta_0)\varphi) e^{i(M-1)(\sin\theta - \sin\theta_0)\varphi} \quad (2-11)$$

The corresponding beamforming power is given by

$$\beta(\theta, \omega) \approx |q(\omega)|^2 \text{sinc}^2(M(\sin\theta - \sin\theta_0)\varphi) \quad (2-12)$$

Therefore, the beamforming power is maximized when the steering angle θ of the scan vector coincides with the direction of the plane wave source as shown in Figure 2-7.

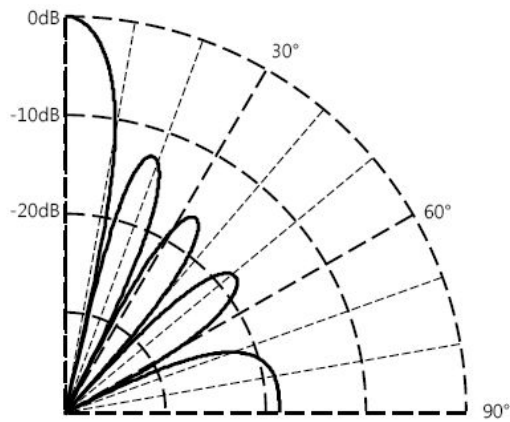


Figure 2-7 Beamforming power distribution

From (2-11), we can derive the identity

$$b(\theta, \omega) \approx q(\omega) \quad (2-13)$$

When $\theta = \theta_0$. Equation (2-13) implies that the output of the delay-and-sum beamformer can be regarded as a source signal. In this regard, the microphone array is considered to a virtual microphone that can reconstruct the source signal as if the microphone is just in front of the source.

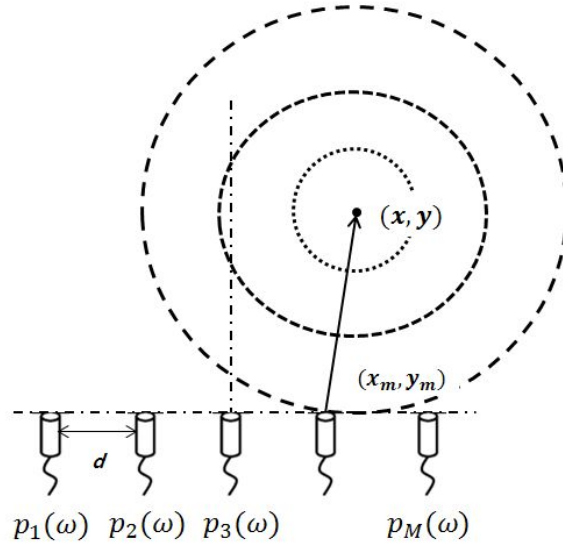


Figure 2-8 Spherical wavefront model

If a source is located close to the array, however, the wavefront from the source is perceptively curved when observed over the array as shown in Figure 2-8. In this case, the spherical wavefront model is well suited to the measurement data. The received sound pressure signal can be written as

$$p_m(\omega) = \frac{q(\omega)e^{i\omega r_m/c}}{r_m} \quad (2-14)$$

where r_m is the distance between the source and the m th microphone. The weighting function has to be modified to handle spherical wavefronts. That is,

$$\mathbf{w}(x, y, \omega) = \frac{1}{M} [w_1(x, y, \omega) w_2(x, y, \omega) \cdots w_M(x, y, \omega)]^T, w_m(x, y, \omega) = e^{i\omega r_m/c} \quad (2-15)$$

where $r_m = \sqrt{(x - x_m)^2 + (y - y_m)^2}$ is the distance between the

assumed source location (x, y) and the m th microphone. The beamforming power of the spherical model can be calculated in the same way as the plane wave case.

The wave propagation simulation of stationary and moving sources are shown in Figure 2-9. If the source moves at a high speed, the frequency distortion occurs, which is called Doppler effect. The frequency domain beamforming method about a moving source needs considerable computation due to the frequency shift by Doppler effect [2.26]. Therefore, the time domain beamforming method was considered in this paper.

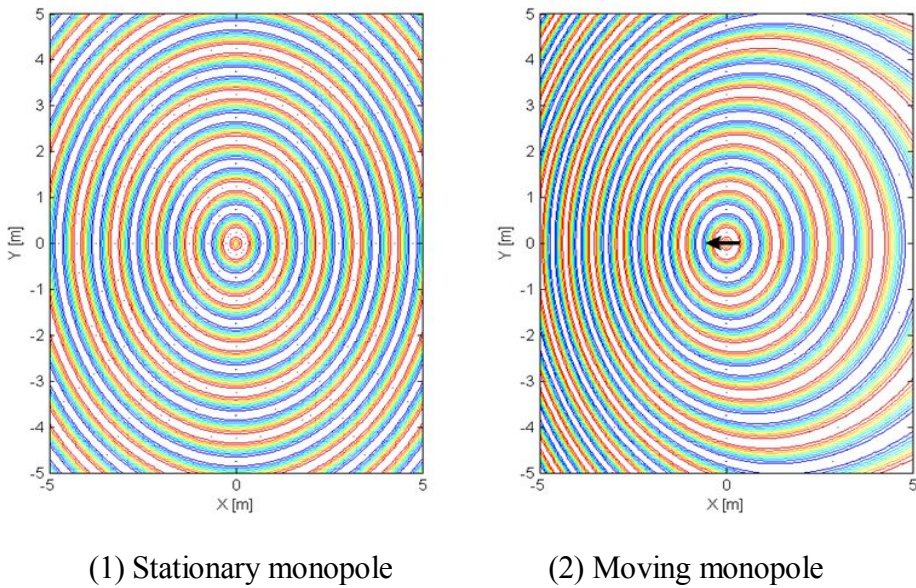


Figure 2-9 Moving monopole and Doppler effect

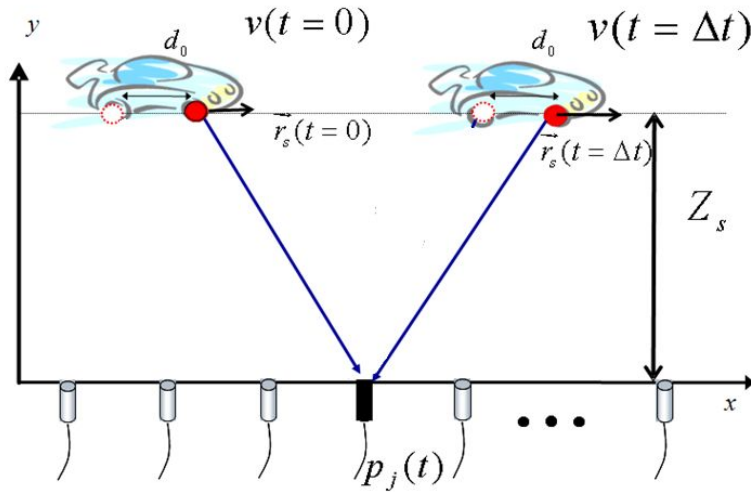


Figure 2-10 Moving source driving in straight lines

The beamforming equation was derived in the time domain. When a radiating source moves at a constant speed as shown in Figure 2-10, the propagating wave measured in frequency contents differ from the produced by the source. This phenomenon has been known as Doppler effect. At the same time, because of changes in the distance between the sound source and the measuring microphone, pressure reduction of the signal over distance occurs.

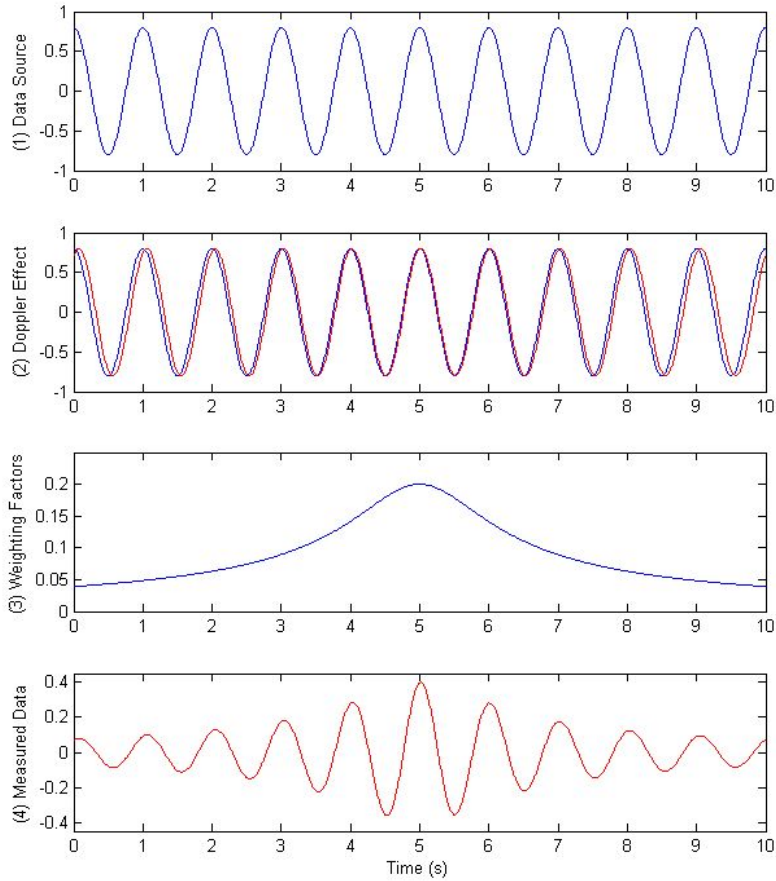


Figure 2-11 Data source and measured data

Therefore, measured signals are influenced by Doppler effect and reduction over the distance as shown in Figure 2-11. When a monopole moves at a constant speed as shown in Figure 2-11 (1), frequency change occurs based on the measurement location as shown in Figure 2-11 (2). Because signal reduction due to distance changes from the source and the measurement sensor also occurs as shown in Figure 2-11 (3), measured signal is affected by

Doppler effect and pressure reduction. Consequently, in order to determine exact location of moving signals, delay and sum beamforming, Doppler effect, and pressure reduction should be considered as shown in Figure 2-11 (4).

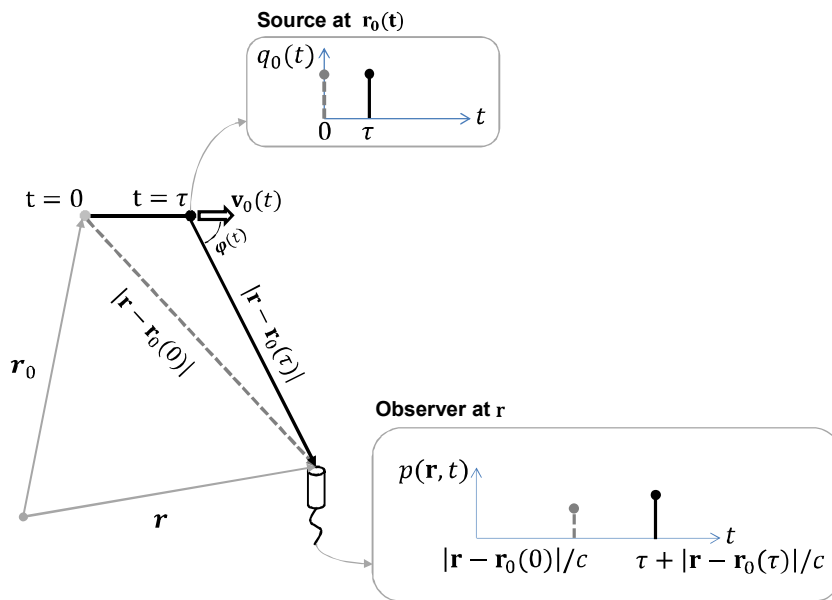


Figure 2-12 Two impulses generated by moving source

For a moving source whose position is continuously changing with respect to time, the output of the time-domain beamformer will only show a blurred image of the sound source along the source trajectory. To find an accurate position of a moving source, the beamformer has to be modified such that moving-source effects, such as the Doppler effect, can be compensated.

To begin, consider a source signal q defined in space and time. For a moving source, the source signal is represented as a multiplication of the time signal $q_0(\tau_s)$ and the Dirac delta function expressing the change in the source position with respect to time:

$$q(\mathbf{r}_s, \tau_s) = q_0(\tau_s)\delta(\mathbf{r}_s - \mathbf{r}_0(\tau_s)) \quad (2-16)$$

The source signal then propagates in space and time. The wavefront emitted at time τ_s and position \mathbf{r}_s arrives at the observer position \mathbf{r} after a time delay of $t = \tau_s + |\mathbf{r} - \mathbf{r}_s|/c$ as shown in Figure 2-12, and hence the transfer function of a moving source is given by

$$h(\mathbf{r}, t | \mathbf{r}_s, \tau_s) = \frac{\delta(t - \tau_s - \frac{|\mathbf{r} - \mathbf{r}_s|}{c})}{4\pi|\mathbf{r} - \mathbf{r}_s|} \quad (2-17)$$

for a monopole sound source. The sound field produced by a moving monopole can be obtained by integrating the product of (2-16) and (2-17) over space and time. That is,

$$\begin{aligned} p(\mathbf{r}, t) &= \int_{-\infty}^{\infty} \int_V \frac{q_0(\tau_s)\delta(\mathbf{r}_s - \mathbf{r}_0(\tau_s))\delta\left(t - \tau_s - \frac{|\mathbf{r} - \mathbf{r}_s|}{c}\right)}{4\pi|\mathbf{r} - \mathbf{r}_s|} dV(\mathbf{r}_s) d\tau_s \\ &= \int_{-\infty}^{\infty} \frac{q_0(\tau_s)\delta\left(t - \tau_s - \frac{|\mathbf{r} - \mathbf{r}_0(\tau_s)|}{c}\right)}{4\pi|\mathbf{r} - \mathbf{r}_s|} d\tau_s \end{aligned} \quad (2-18)$$

The integral with respect to τ_s can be simplified by exploiting the following Dirac delta identity:

$$\delta[q(\tau)] = \sum_j \frac{\delta(\tau)}{|dq/d\tau|_{\tau=\tau_j}}, \text{ where } q(\tau_j) = 0, \quad (2-19)$$

which is a generalization of $\delta(a\tau) = \delta(\tau)/a$.

From (2-19), the integral of (2-18) can be replaced by a finite sum:

$$p(\mathbf{r}, t) = \sum_j \frac{q_0(\tau_j)}{4\pi|r-r_0(\tau_j)| |1-M_0(\tau_j)|}, \quad (2-20)$$

where the τ_j are the roots of

$$\tau_j = t - \frac{|r-r_0(\tau_j)|}{c}. \quad (2-21)$$

The relative velocity of the source in the direction of the observer M_0 (in terms of the Mach number) is given by

$$\begin{aligned} M_0(\tau_j) &= -\frac{1}{c} \left. \frac{d|r-r_0(\tau_s)|}{d\tau_s} \right|_{\tau_s=\tau_j} \\ &= \frac{\mathbf{v}_0(\tau_j) \cdot \mathbf{r}-\mathbf{r}_0(\tau_j)}{c |r-\mathbf{r}_0(\tau_j)|} \\ &= \frac{|\mathbf{v}_0(\tau_j)|}{c} \cos \varphi(\tau_j), \text{ where } v_0(\tau_j) = \left. \frac{d\mathbf{r}_0}{d\tau} \right|_{\tau_s=\tau_j} \end{aligned} \quad (2-22)$$

If we only consider a single τ_j and neglect the $1 / |1 - M_0(\tau_j)|$ term, then (2-20) just explains how the monopole sound field emitted by the source

at time τ_j propagates to the listener position at time t . Here, the measurement time t is often referred to as the reception time, and τ_j is called the emission time. The amplitude of the wavefront decays according to the distance between the position where the wavefront is excited ($\mathbf{r}_s(\tau)$) and the observation point \mathbf{r} .

The extra magnitude scaling of $1 / |1 - M_0(\tau_j)|$ is due to the time-varying delta function $\delta\left(t - \tau_s - \frac{|\mathbf{r} - \mathbf{r}_s|}{c}\right)$ of (2-18). The physical meaning of this scale factor can be understood by comparing the Dirac delta functions at two different observation points (observer I and II of Figure 2-13). Note that the delta function can be derived from reducing the duration of a rectangular pulse to zero while its area is held constant. Since the delta functions at the positions of observer I and II have different arguments with respect to τ_s , the amplitudes of the Dirac delta function (or the area of a rectangular pulse of infinitesimal time duration) are different. If we consider the density of discrete pulses of Figure 2-13 as the total area of the delta function, we can infer that the pulse density at observer II will be higher than at observer I. Therefore, the

area under the same infinitesimal time duration will be larger at observer II, and the corresponding amplitude of the delta function will be higher. This kind of change in the amplitude that occurs due to a moving (convective) monopole is called convective Doppler amplification.

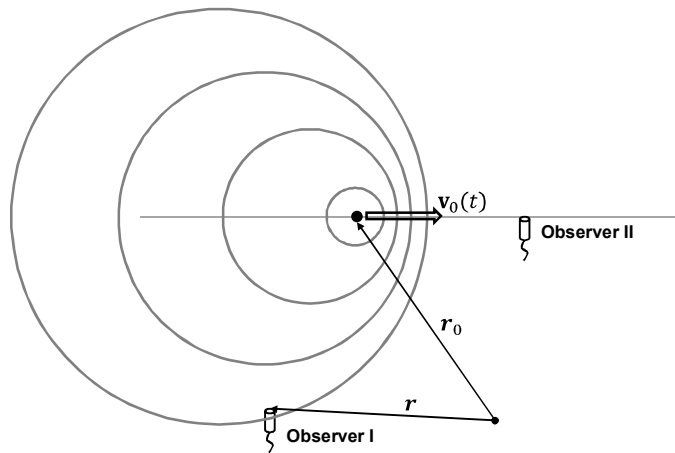


Figure 2-13 Propagation produced by moving source

The conversion between the reception and emission times can be accomplished through (2-21). For example, if a source is moving in the positive x direction at a constant speed v_0 , then the source and receiver positions can be described as

$$\mathbf{r}_0 = [v_0\tau_j, 0, 0], \quad \mathbf{r} = [x, y, z], \quad (2-23)$$

and the roots of (2-21) can be found by solving the following equation with respect to τ_j :

$$\tau_j = t - \frac{\sqrt{(x-v_0\tau_j)^2 + y^2 + z^2}}{c}. \quad (2-24)$$

The solutions of (2.24) are given by

$$\tau_{1,2} = \frac{ct - M_a x \pm \sqrt{(x - cM_a t)^2 + (1 - M_a^2)(y^2 + z^2)}}{c(1 - M_a^2)}, \text{ with } M_a = \frac{v_0}{c} \quad (2-25)$$

For a source moving at a speed less than the speed of sound ($M_a < 1$), the positive root cannot be a physical solution since the emission time is delayed more than the reception time. As a consequence, the emission time can be related to the reception time as

$$\tau = \frac{ct - M_a x - \sqrt{(x - cM_a t)^2 + (1 - M_a^2)(y^2 + z^2)}}{c(1 - M_a^2)} \quad (2-26)$$

and the measured pressure field at \mathbf{r} is simply given by

$$p(\mathbf{r}, t) = \frac{q_0(\tau)}{4\pi|\mathbf{r} - \mathbf{r}_0(\tau)|} \frac{1}{|1 - M_0(\tau)|} \quad (2-27)$$

Therefore, the moving source produces two types of distortions as compared to a stationary source. The first is the change in the arrival time of a source signal $q_0(\tau)$, and the second is Doppler amplification. For linear motion of the source, M_0 is given by

$$M_0(\tau) = -\frac{1}{c} \frac{d}{d\tau} \left(\sqrt{(x - v_0\tau)^2 + y^2 + z^2} \right)$$

$$= M_a \frac{(x-v_0\tau)}{\sqrt{(x-v_0\tau)^2+y^2+z^2}} \quad (2-28)$$

Consequently, a source approaching the microphone ($x > v_0\tau$) produces an increased measured amplitude, and a source moving away from the microphone decreases the measured amplitude.

The measured pressure signal of (2-20) is distorted by the movement of the source. The compensation of the distortion, often called de-Dopplerization, is accomplished by transforming the signal measured by an microphone array fixed in space to one that moves with the same speed as the source. The concept of de-Dopplerization is illustrated in Figure 2-14. In this section, we investigate how the pressure signal of a microphone moving with the source can be reconstructed as if the measurement was taken by a microphone fixed in space.

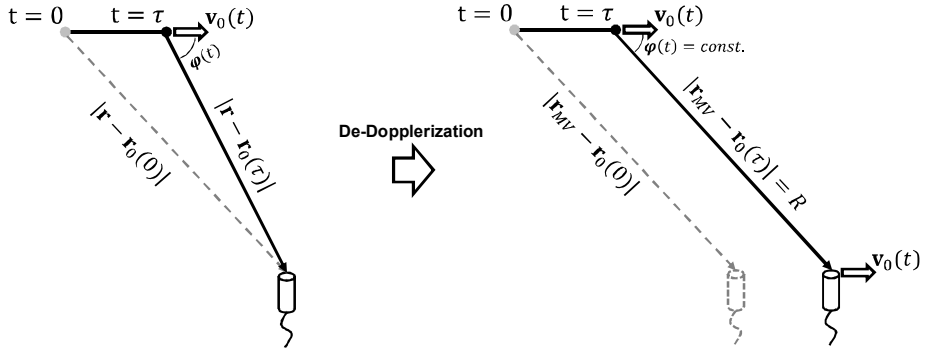


Figure 2-14 De-Dopplerization concept

De-Dopplerization can be implemented as follows: first, using the relation of (2-20), the pressure data measured by a fixed microphone array is converted to the source signal $q_0(\tau)$. Next, from the estimated source signal, the pressure signal at a microphone array moving with the source is reconstructed.

For the estimation of the source signal, we first need to relate the temporal axis defined for the reception time with that defined for the emission time. If the temporal axis for the emission time is defined with a regular sampling interval of Δt , it can be written as

$$\tau[n] = n\Delta t, n = 0, \dots, N - 1 \quad (2-29)$$

and we can calculate the location of a sound source $\mathbf{r}_0(\tau)$ and $M_0(\tau)$ over the defined temporal axis. The reception time can be expressed in terms

of the emission time as

$$t = \tau + |r - r_0(\tau)|/c \quad (2-30)$$

and the pressure signal takes the form

$$p(\mathbf{r}, \tau[n] + \frac{|r - r_0(\tau[n])|}{c}) \quad (2-31)$$

However, the pressure signal $p(\mathbf{r}, t)$ measured by the fixed microphone array might have uniform temporal sampling with respect to the reception time t and not to the emission time τ . Therefore, to calculate (2-31), the measured data has to be resampled. A resampling technique with a fractional delay filter can be employed for this procedure. Once the pressure signal at the reception time is obtained, then the source signal $q(\tau)$ can be derived from (2-27). That is,

$$q_0(\tau) = 4\pi|\mathbf{r} - \mathbf{r}_0(\tau)||1 - M_0(\tau)| p(\mathbf{r}, \tau + \frac{|\mathbf{r} - \mathbf{r}_0(\tau)|}{c}) \quad (2-32)$$

We now have an estimation of the source signal but no information about the location of the source. To estimate the source location, we reconstruct the pressure signal at the location of a microphone moving with the sound source. By denoting the position of the moving microphone as $\mathbf{r} = \mathbf{r}_{MV}(\tau)$, the

pressure signal measured by the moving microphone can be written as

$$p(\mathbf{r}_{MV}(\tau), t) = \frac{q_0(\tau)}{4\pi|\mathbf{r}_{MV}(\tau) - \mathbf{r}_0(\tau)|} \quad (2-33)$$

Note that the Doppler amplification $1 - M_0(\tau)$ disappears because the relative motion between the microphone and moving source is zero. Without this relative motion, the distance between the microphone and source $|\mathbf{r}_{MV}(\tau) - \mathbf{r}_0(\tau)| = R$ is time invariant, and the relation between the reception and emission times is just given by a pure time delay, that is,

$$t = \tau + R/c \quad (2-34)$$

To summarize, the de-Dopplerized microphone signal can be written as

$$p\left(\mathbf{r}_{MV}(\tau), \tau + \frac{R}{c}\right) = |1 - M_0(\tau)| \frac{|\mathbf{r} - \mathbf{r}_0(\tau)|}{R} p\left(r, \tau + \frac{|\mathbf{r} - \mathbf{r}_0(\tau)|}{c}\right) \quad (2-35)$$

The de-Dopplerization procedure described in (2-35) assumes a single source and single microphone. Extending the concept to multiple sources and microphones, beamforming of a moving object can be accomplished.

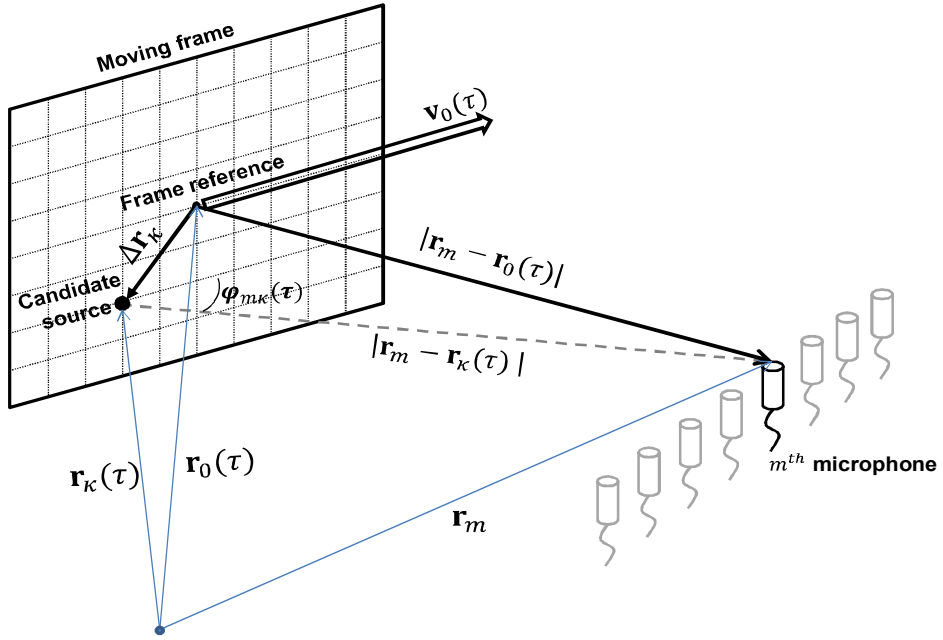


Figure 2-15 Beamforming problem with sources in moving frame

Suppose a number of grid points representing the candidate source locations are attached to a frame with a center $\mathbf{r}_0(\tau)$ that moves with a speed v_0 as shown in Figure 2-15. Denoting each position of the candidate source as $\mathbf{r}_k(\tau) = \mathbf{r}_0(\tau) + \Delta\mathbf{r}_k$ ($\kappa = 1, \dots, K$), the source signal of the κ th source can be estimated from the m th microphone signal $p(r_m, t)$. From (2-32), the source signal estimated by the m th microphone (q_{mk}) is given by

$$q_{mk}(\tau) = 4\pi|\mathbf{r}_m - \mathbf{r}_k(\tau)||1 - M_{mk}(\tau)|p(\mathbf{r}_m, \tau + |\mathbf{r}_m - \mathbf{r}_k(\tau)|c) \quad (2-36)$$

where r_m is the position of the m th microphone. The variable M_{mk} represents the relative speed of the κ th sound source with respect to the m th

microphone and is given by

$$M_{mk}(\tau) = \frac{|v_0(\tau)|}{c} \cos \varphi_{mk}(\tau) \quad (2-37)$$

with φ_{mk} being the angle between the direction of velocity vector v_0 and $\mathbf{r}_m - \mathbf{r}_k(\tau)$.

Since we have K source signals each of which is estimated from each microphone, the de-Dopplerized source signal calculated from multiple microphones are averaged to yield the beamformer output:

$$b(\Delta r_\kappa, \tau) = \frac{1}{M} \sum_{m=1}^M q_{mk}(\tau) \quad (2-38)$$

This procedure can be likened to the delay-and-sum beamformer. The major difference with the stationary case is that the extra time delay due to the source movement and the Doppler amplification are compensated.

2.2 Microphone array design

In this section, the array performance indication factors were introduced and effective microphone array design was investigated. Microphone array measurements are the only possible method to localize, separate, and measure the source strengths of the different noise sources on a by-passing high-speed train.

1) Microphone array design review

Research on aero-acoustic noise from high-speed trains and development of the microphone array measurement technique has mainly been carried out through the German-French cooperation DEUFRAKO K and K2, during the 90s [2.27-2.31]. The projects extended over many years and included theoretical as well as practical work. The characteristics of some simple array configurations are shown from Figure 2-16 to Figure 2-19. To localize sound sources in two dimensions, also the microphone configuration has to be 2-D, for example, cross or planar. The shape of the microphone configuration can be seen in the array output as side-lobes, or ghost images. This spatial noise

can also be seen in the sound maps resulting from a microphone array measurement. Therefore, a regular, or periodic, microphone configuration should be avoided. However, to build a microphone array with an irregular configuration requires a great number of microphones, increasing the cost of the system. At the beginning of the 90s, multi-channel data acquisition systems were rather expensive. Figure 2-20 shows a nested linear array, an array consisting of several sub-arrays, in order to cover a broader frequency range without suffering from aliasing (increased spatial noise), which may occur if the distance between the microphones is greater than a half sound wavelength. High frequencies are analyzed with the innermost sub-array, with the shortest microphone distance, while the lowest frequencies in the range of interest are analyzed with the outermost sub-array. Measurements carried out in DEUFRAKO K and DEUFRAKO K2 as shown from Figure 2-21 to Figure 2-27. It is interesting to note that the X-shape of the microphone array configuration can be seen in the sound map as increased side-lobe levels. Measurements on the German Transrapid, the magnetically levitated train

show that most aero-acoustically generated noise propagated from the area just in front of the nose of the front power car.

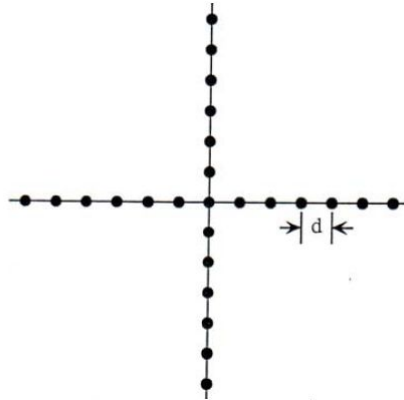


Figure 2-16 Cross array configuration

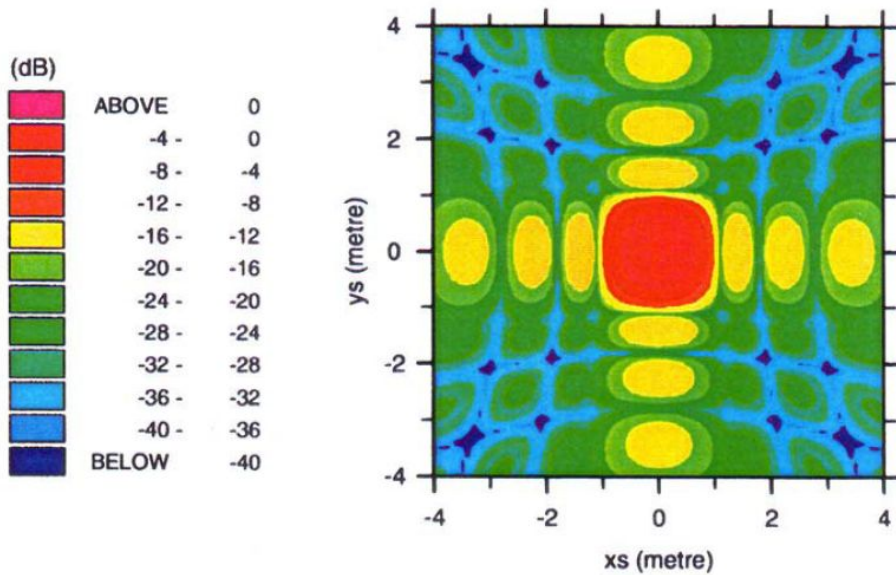


Figure 2-17 Characteristics of cross array

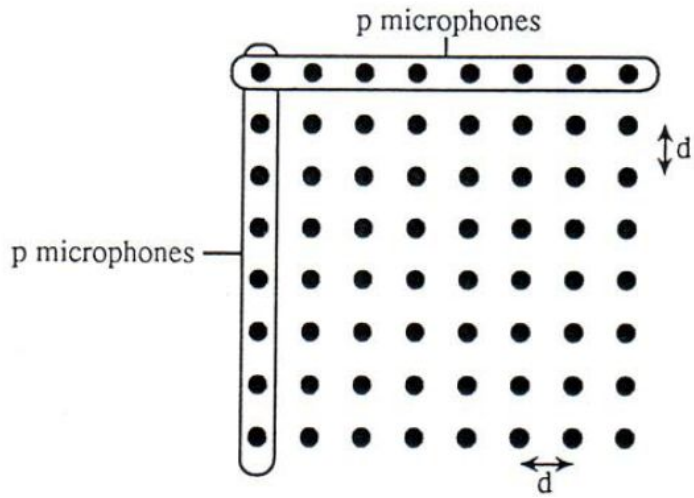


Figure 2-18 Planar array configuration

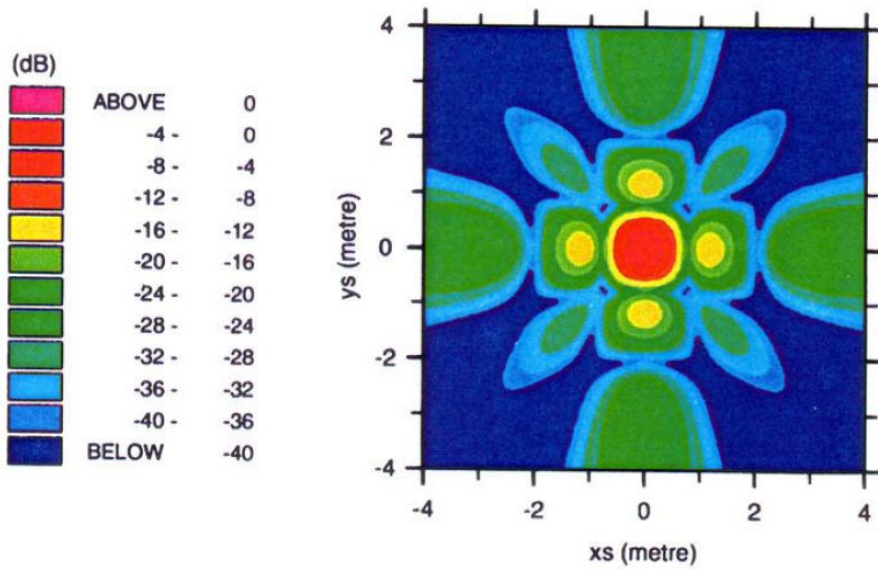


Figure 2-19 Characteristics of planar array

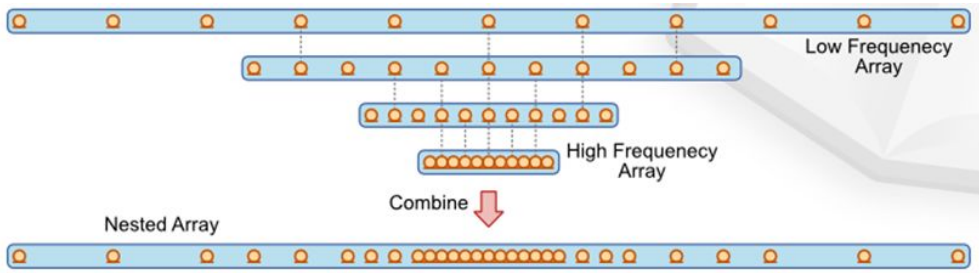


Figure 2-20 Nested linear arrays

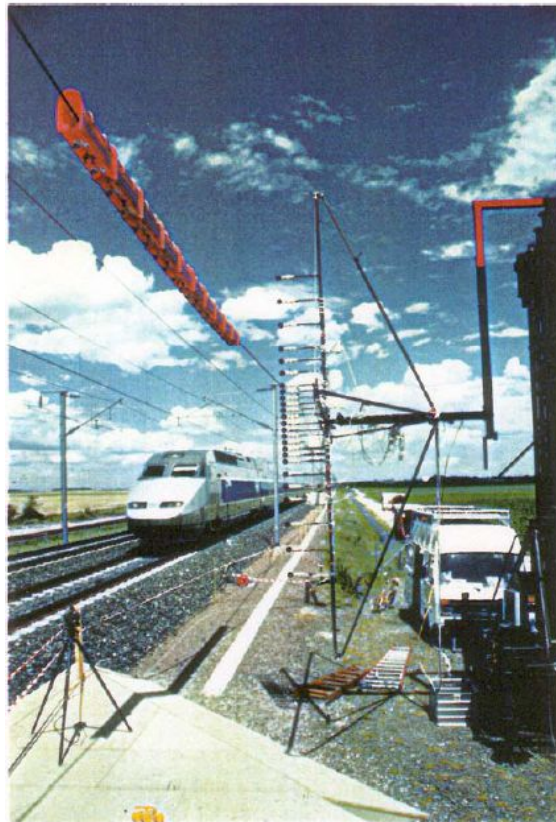


Figure 2-21 Vertical nested array

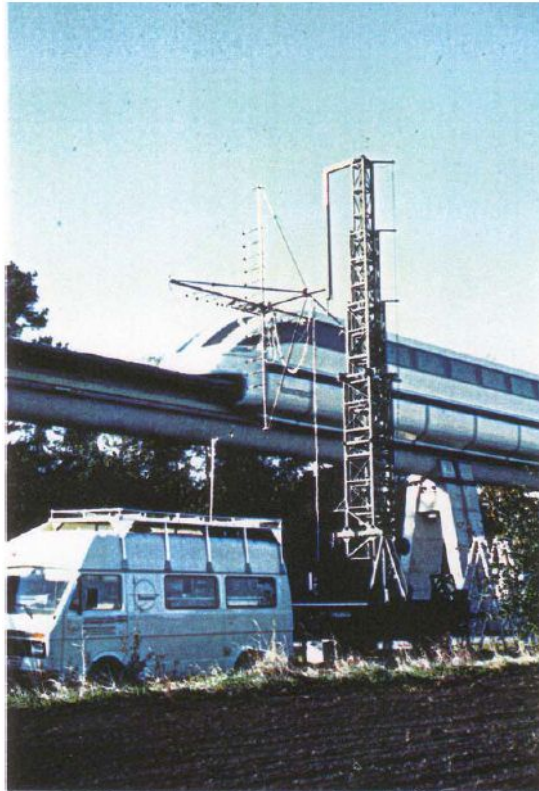


Figure 2-22 Cross array for measurements

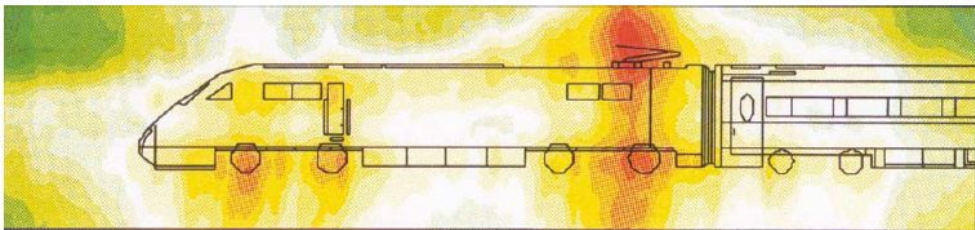


Figure 2-23 Noise map of ICE front power car measured by cross array

(Relative level (dB): $-10 \leq$  ≤ 0)



Figure 2-24 X-shaped microphone array installed beside high-speed railway line.

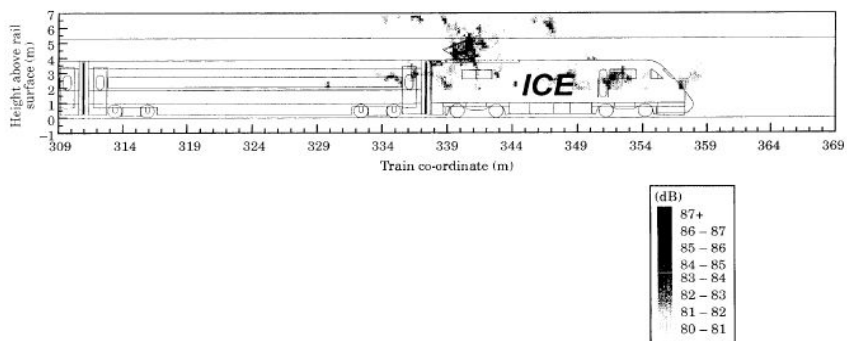


Figure 2-25 Sound map of noise radiation from pantograph

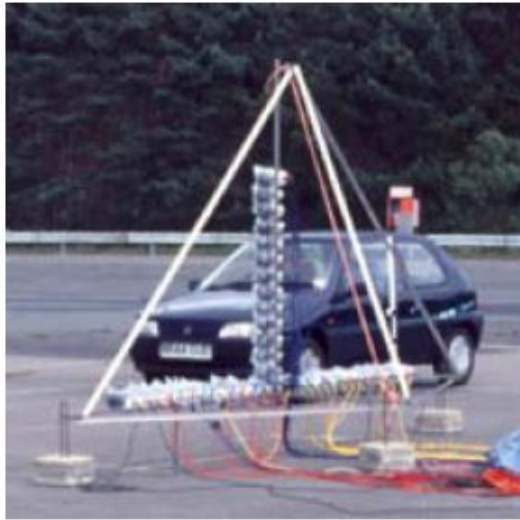


Figure 2-26 T-array for measurement

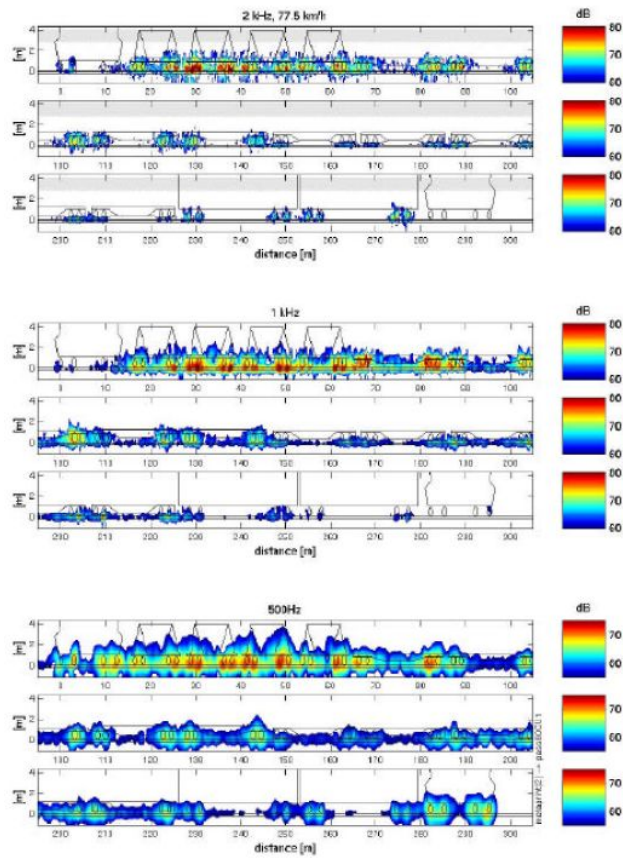


Figure 2-27 Sound map picked up by T-array

At the beginning of the 2000s, multi-channel data acquisition systems had become relatively more inexpensive, enabling microphone arrays and configurations with more channels such as irregular configurations. These results exhibit much higher sound map quality, thanks to better resolution and spatial dynamic range, as a result of a higher channel count. These are properties crucial in characterizing noise sources on high-speed trains.

Deutsche Bahn has developed a microphone array consisting of 90 microphones in a spiral-like configuration, with a diameter of 4 m as shown in Figure 2-28 [2.32]. This irregular microphone configuration is chosen in order to optimize resolution and dynamic range of noise sources on a by-passing high-speed train in the frequency range of interest, roughly 200 Hz ~ 3150 Hz as shown in Figure 2-29. SNCF have developed a star-like microphone configuration as shown in Figure 2-30 [2.33, 2.34]. They have reported results using 73 microphones in a nested double star, in order to cover the frequency range of 315 ~ 4000 Hz as shown in Figure 2-31. Since a spiral configuration is more irregular than a star configuration, a spiral configuration probably is

the one with the best dynamic range (lowest side-lobe levels). It would be easy to show this with the help of a simulation calculation. Both systems use classical delay-and-sum beamforming, which is necessary in order to focus on moving sound sources.



Figure 2-28 Deutsche Bahn spiral array in front of ICE 3

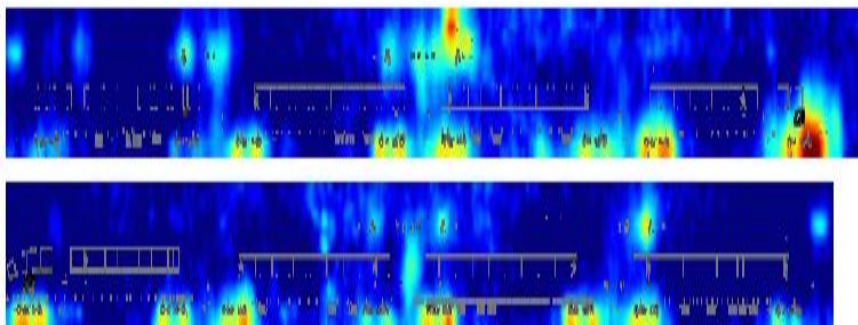


Figure 2-29 Noise map of ICE 3 travelling left to right
(Relative level (dB): $-10 \leq$  ≤ 0)



Figure 2-30 SNCF star-like, double nested microphone array consisting of 73 microphones

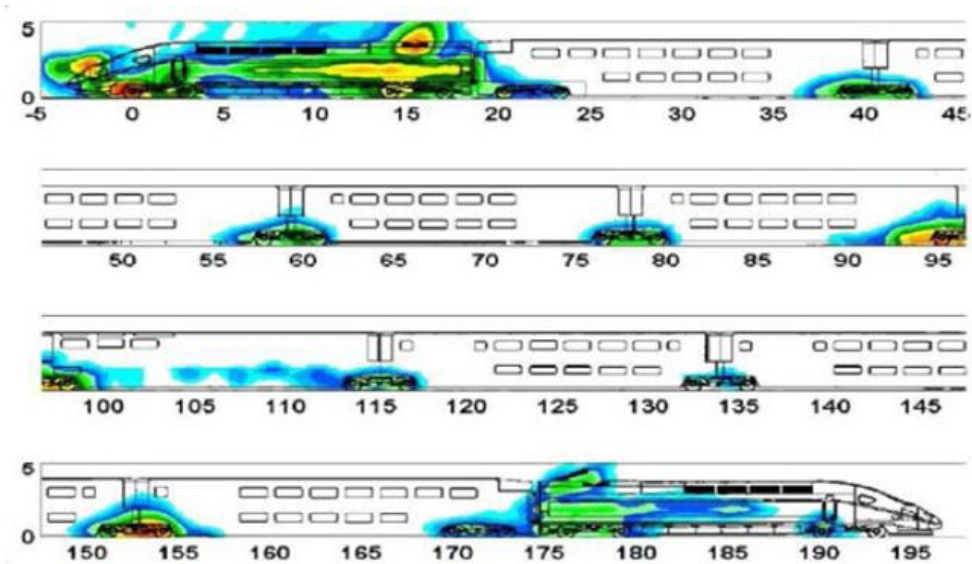


Figure 2-31 Noise map of Duplex TGV travelling right to left

(Relative level (dB): $-10 \leq$  ≤ 0)

Sound images of a whole high-speed train pass-by clearly show that the two most important noise sources are the first bogie and the pantograph. The great number of wheels generating rolling noise, and also equipment on the roof can also be seen.

All practical array measurement results necessarily suffer from deviations from results obtained by a perfect array, i.e. one with very small microphone spacing, and very large length/diameter. Unfortunately, it is difficult to satisfy both at the same time with a limited number of microphones. Therefore, interpretation of measurement results, often colorful source distribution image, is not obvious.

2) Array resolution indicators

Sound images such as these above show the relative importance of different noise sources. However, it is not obvious how to transform the sound maps to absolute sound power levels of the different sources. The reason is that the microphone array has a limited resolution and dynamic range, which may be improved by an increase of the number of microphones. Another problem is that the beam width, and thus the resolution, depends on the frequency, and the angle and position of the sound source relative the microphone array. A source at the outskirts of the image looks much bigger than the same source in the center. Therefore, frequency and space dependent transfer functions transforming sound maps to sound power levels need to be developed. They may be found either through numerical simulations or comparison with measurements on known reference sources.

To exactly separate scattered sounds, an array should have good resolution. The resolution of the array can be assessed by 3 dB bandwidth and maximum side-lobe level (MSL) [2.8, 2.9] as shown in Figure 2-32. The 3 dB bandwidth

is the most common measure of bandwidth. It is defined as the width of the main lobe between two points that are 3 dB below the peak. The width of the main lobe represents the minimum distance we can distinguish between two closely located sound sources. In addition, the presence of side lobes in the directivity pattern implies that waves from non-focus directions will leak into the measurement of the main lobe direction.

On the decibel scale, the MSL can be represented as

$$\text{MSL} = 10 \log_{10} \left(\frac{\beta(\theta_{max})}{\beta(\theta_{max,s})} \right) \quad (2-39)$$

where θ_{max} is the angle (or location) of the mainlobe, and $\theta_{max,s}$ denotes the angle of the maximum side-lobe.

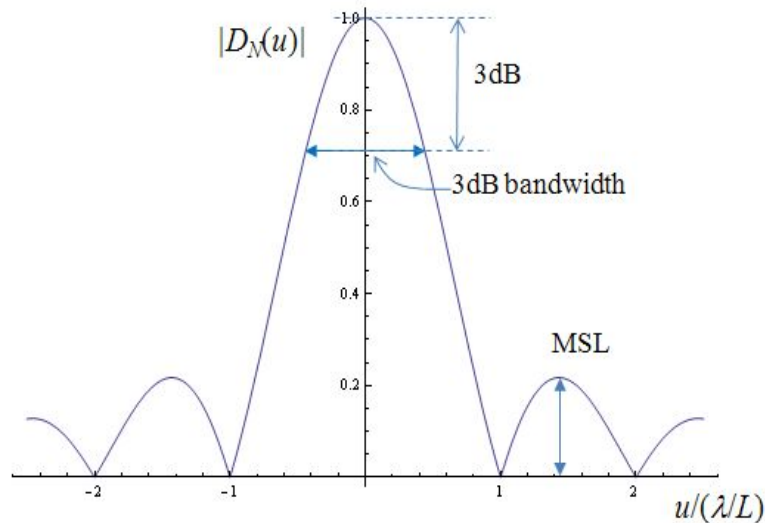


Figure 2-32 3 dB bandwidth and maximum side-lobe level

The MSL represents the ability to detect a secondary sound source of small power in the presence of a strong primary source. If the secondary source power is smaller than the MSL multiplied by the primary source power, then the secondary source is indistinguishable from the side-lobes of the primary source beamforming power distribution. This will produce false peaks or sources in the directional source map. Even an ideal point source, because it is measured with the extent of the width of the source, the smaller 3 dB bandwidth has good resolution. Moreover, the large MSL has bad resolution because it is difficult to distinguish between the actual source position and the position of the side-lobes. The beam shape has 3 dB bandwidth of $\Delta u \approx 0.9\lambda/L$. If we assume the source is at the distance of r_0 and θ is small, the width of the beam shape can be expressed as $b \approx r_0\lambda/L$. Therefore, a good phased array design can therefore be characterized as having a narrow bandwidth and low MSL.

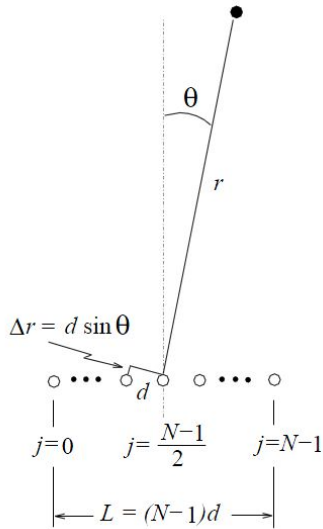


Figure 2-33 Geometry used in deriving far-field beam pattern of simple line array

One of the important factors for the effective array design is spacing of the microphones in the array. The spacing is closely related to the resolution frequency of the array. Consider a line of N microphones with adjacent elements spaced distance d apart, as shown in Figure 2-33. Then, the pressure at the j th element, caused by a sound source in the far field, has the form

$$P_j = \frac{A}{r_j} e^{i(\omega t - kr_j)} \quad (2-40)$$

where r_j is the distance from this element to the source. Now, assume that all microphones are identical, then the sum of all microphone pressures.

$$p(r, \theta, t) = \sum_{j=0}^{N-1} \frac{A}{r_j} e^{i(\omega t - kr_j)} \quad (2-41)$$

If we restrict attention to sources in the far, we can approximate by assuming all r_j are parallel. Then,

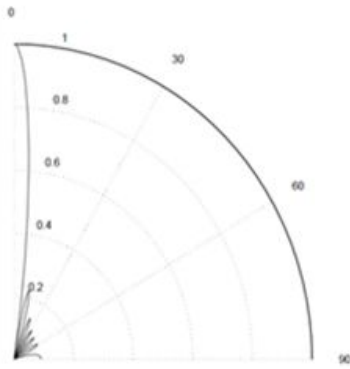
$$r_j = r - \frac{N-1}{2} \Delta r + j \Delta r \quad (2-42)$$

where r is the distance from the source to the center of the array, and $\Delta r = d \sin \theta$. In the far field, r_j in the denominator can be replaced with r and the sum takes the form by using trigonometric identities,

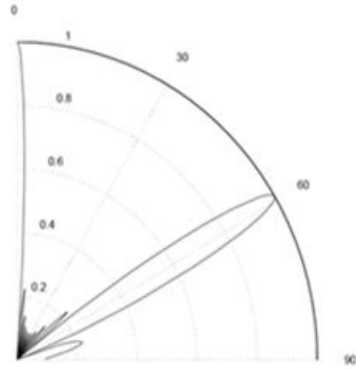
$$p(r, \theta, t) = \frac{A}{r} e^{i(\omega t - kr)} \frac{\sin(\frac{N}{2} kd \sin \theta)}{\sin(\frac{1}{2} kd \sin \theta)} \quad (2-43)$$

The directivity function can be defined as

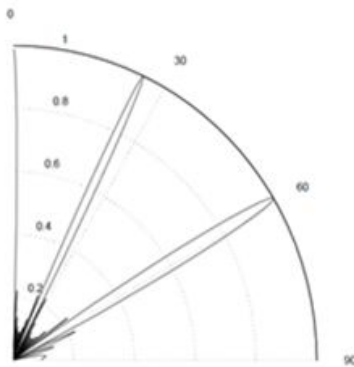
$$D(\theta) = \frac{\sin(\frac{N}{2} kd \sin \theta)}{\sin(\frac{1}{2} kd \sin \theta)} \quad (2-44)$$



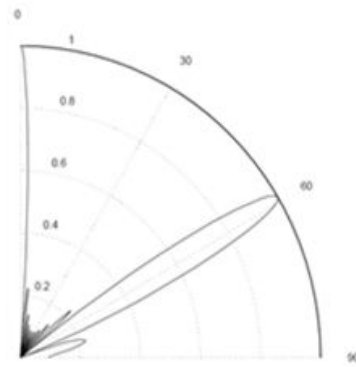
(1) $N = 11, d = 0.4 \text{ m}, f = 500 \text{ Hz}$



(2) $N = 11, d = 0.4 \text{ m}, f = 1000 \text{ Hz}$



(3) $N = 11, d = 0.4 \text{ m}, f = 2000 \text{ Hz}$



(4) $N = 11, d = 0.2 \text{ m}, f = 1000 \text{ Hz}$

Figure 2-34 Beam patterns for line array

The microphone placement in the array is closely related to its resolution. Beam power will appear in the normal form if the spacing of the microphone is smaller than the wavelength of the frequency as shown in Figure 2-34 (1). In a case of the source frequency of 1000 Hz, if the spacing of microphone is greater than the wavelength of the frequency ($d = 0.4 \text{ m} > 0.343 \text{ m} = \lambda$), the maximum side-lobe is equal to the main lobe at about 59.1° as shown in

Figure 2-34 (2). It is not possible to identify the exact location of the sound source when the size of the maximum side-lobe is equal to the size of the side-lobe. There is a ghost image in this case even though the actual source does not exist as shown in Figure 2-34 (3). The ghost image is increased by the frequency increase. Therefore, the microphone spacing should be smaller than the wavelength of the frequency as shown in Figure 2-34 (4). To avoid grating lobes, the microphone spacing must be chosen so that

$$d < \lambda \quad (2-45)$$

In this sense, the microphone placement in the array is closely related to its resolution. To produce the best performance with a limited number of microphones, they should be placed in such a way that aliasing problems caused by duplicate sampling are avoided. Aliasing produces ghost images with the same level as the true sources.

Side-lobes are undesirable consequence of the abrupt truncation at each end of the window. By tapering the window smoothly to zero at each end (shading), the height of the side-lobes can be diminished; however, this is achieved at the

expense of a wider main lobe. A window is realized by multiplying each microphone pressure signal by a weighing factor w_j , of which the amplitude depends on the position within the window as shown in Figure 2-35.

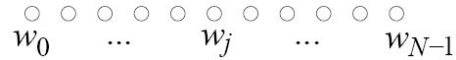


Figure 2-35. Amplitude weighting factors as function of position

Apparently, good array design is a trade-off between main lobe width and sidelobe levels [2.35]. Examples of some commonly used windows are shown in Figure 2-36. These windows are specified by the following equations:

Rectangular:

$$w_j = 1, 0 \leq j \leq N - 1 \quad (2-46)$$

Bartlett (triangular):

$$w_j = \begin{cases} \frac{2j}{N-1}, & 0 \leq j \leq \frac{N-1}{2} \\ 2 - \frac{2j}{N-1}, & \frac{N-1}{2} \leq j \leq N - 1 \end{cases} \quad (2-47)$$

Hanning:

$$w_j = \frac{1}{2} \left[1 - \cos \left(\frac{2\pi j}{N-1} \right) \right], 0 \leq j \leq N - 1 \quad (2-48)$$

Hamming:

$$w_j = 0.54 - 0.46 \cos \left(\frac{2\pi j}{N-1} \right), 0 \leq j \leq N - 1 \quad (2-49)$$

Blackman:

$$w_j = 0.42 - 0.5\cos\left(\frac{2\pi j}{N-1}\right) + 0.08\cos\left(\frac{4\pi j}{N-1}\right), 0 \leq j \leq N-1 \quad (2-50)$$

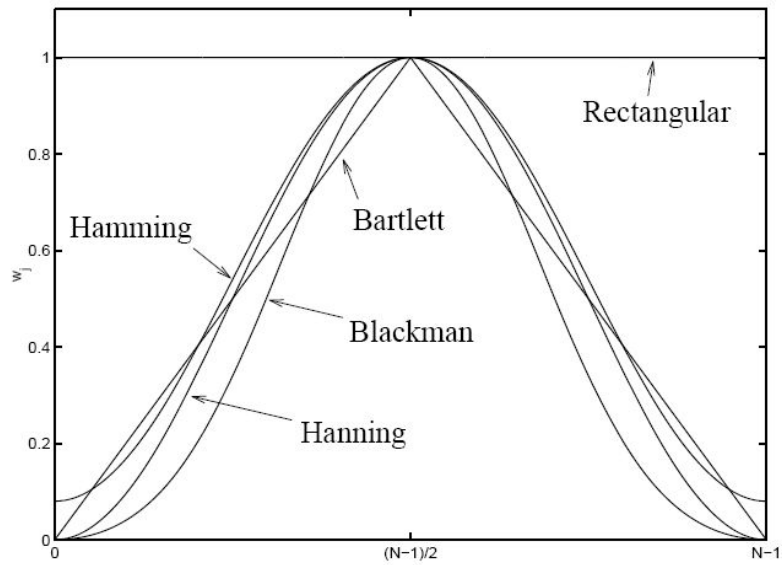


Figure 2-36 Commonly used window functions

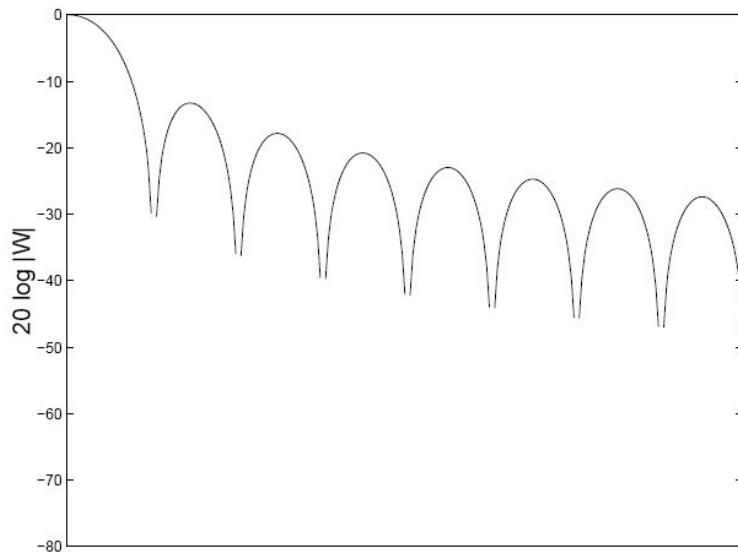


Figure 2-37 Fourier transform of rectangular window

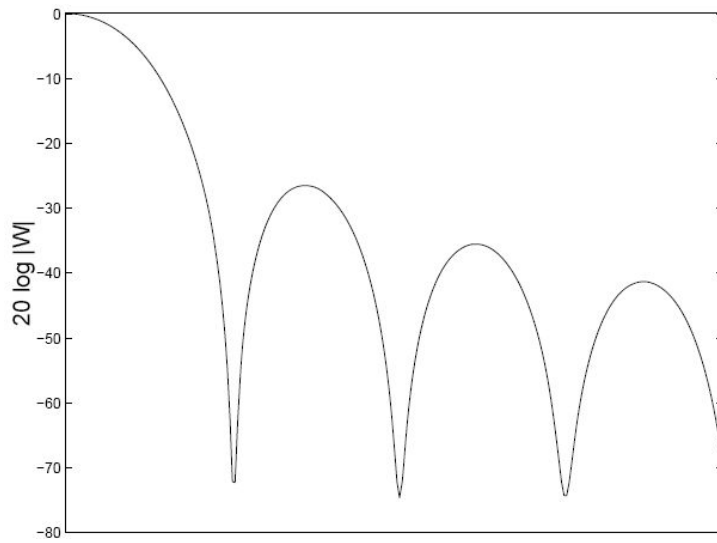


Figure 2-38 Fourier transform of Bartlett window

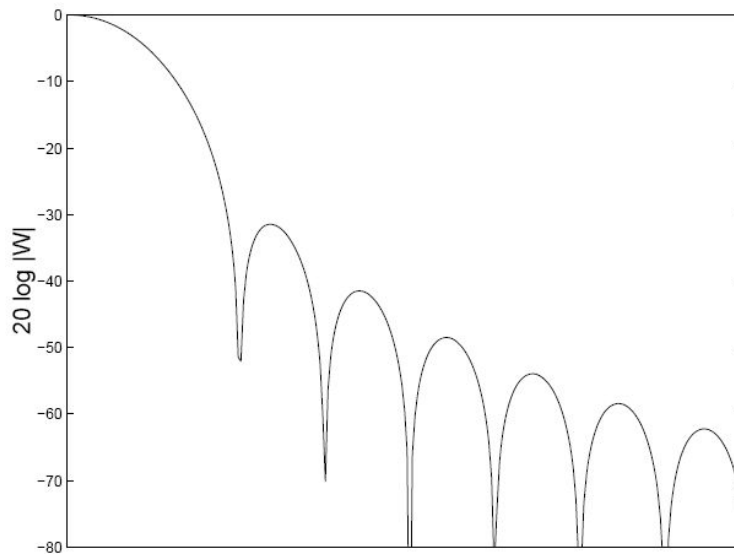


Figure 2-39 Fourier transform of Hanning window

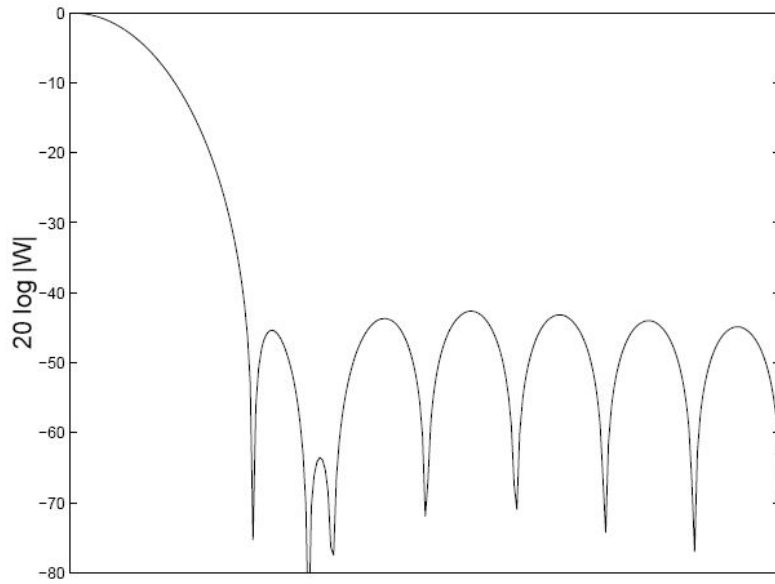


Figure 2-40 Fourier transform of Hamming window

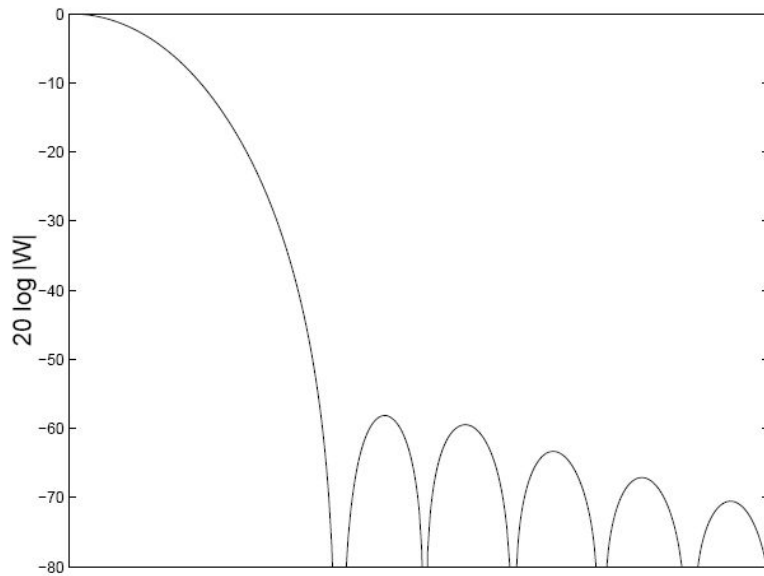


Figure 2-41 Fourier transform of Blackman window

The spatial aliasing problem is eliminated when totally non-redundant array geometry is implemented. Such an arrangement produces less redundancy in the signals measured at each microphone. The redundancy of microphone arrays can be found through a correlation function of the measured signals. The correlation function of the signal obtained at the i th and j th microphones depends on two sensor location as follows [2.8] :

$$R_{i,j}(\tau) = w_i w_j^* R_f(\vec{x}_i - \vec{x}_j, \tau) \quad (2-51)$$

In the equation above, the correlation function depends on $\vec{x}_i - \vec{x}_j$ between two sensor locations. The co-array pattern represents the difference in the position of each microphone based on the microphone array configuration. Therefore, an array having irregular configuration is effective to avoid aliasing problems caused by duplicate sampling. In other words, the co-array pattern represents the difference in the position of each microphone on the basis of the microphone array configuration.

In order to obtain the relation between the microphone geometry and resolution, 96-channel rectangular, radial microphone arrays with different

spacing were investigated. In the rectangular array, configuration and co-array was also rectangular shapes and regular spacing as shown in Figure 2-42. When a co-array pattern has a regular spacing and array spacing is smaller than the wavelength of the sound source, spatial aliasing may occur. In the radial array with same spacing, the array configuration was random, but regular spacing which may cause aliasing problem in the high frequency as shown in Figure 2-43. In the radial arrays with complex spacing, it had irregular configuration and spacing so redundancy and aliasing to be avoided as shown in Figure 2-44 and Figure 2-45, which had centralized shapes and dispersed shapes, respectively.

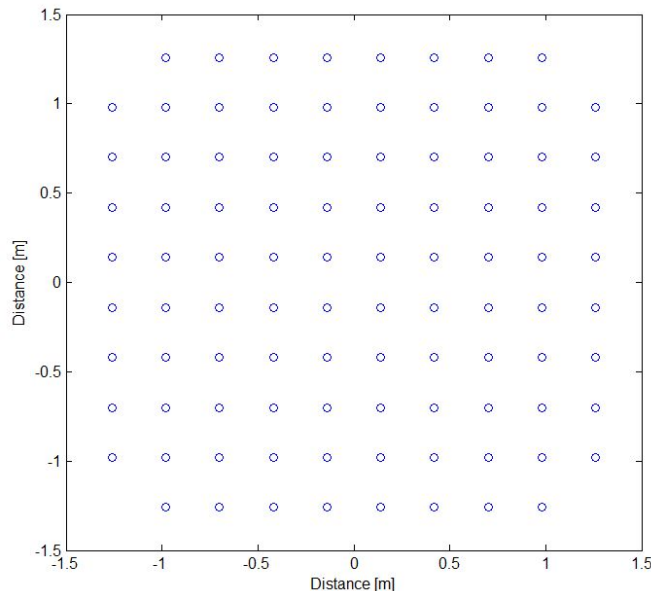


Figure 2-42 96-channel rectangular array

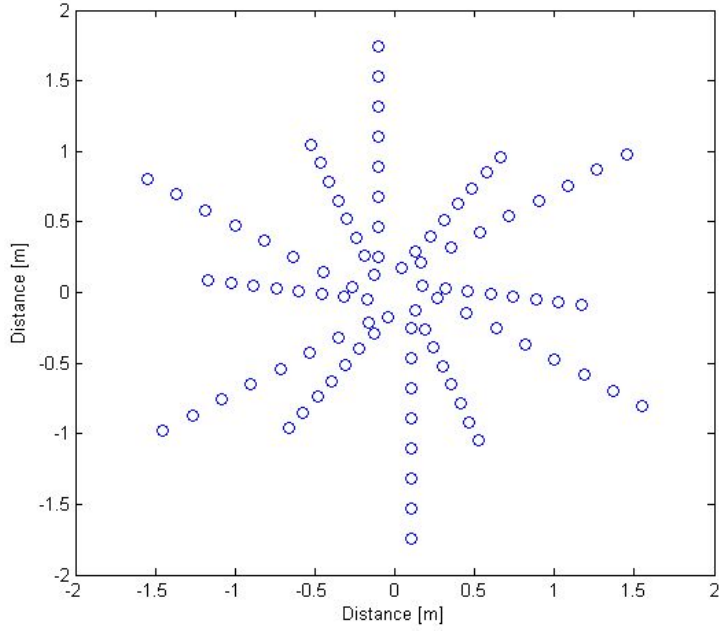


Figure 2-43 96-channel radial microphone array with same spacing

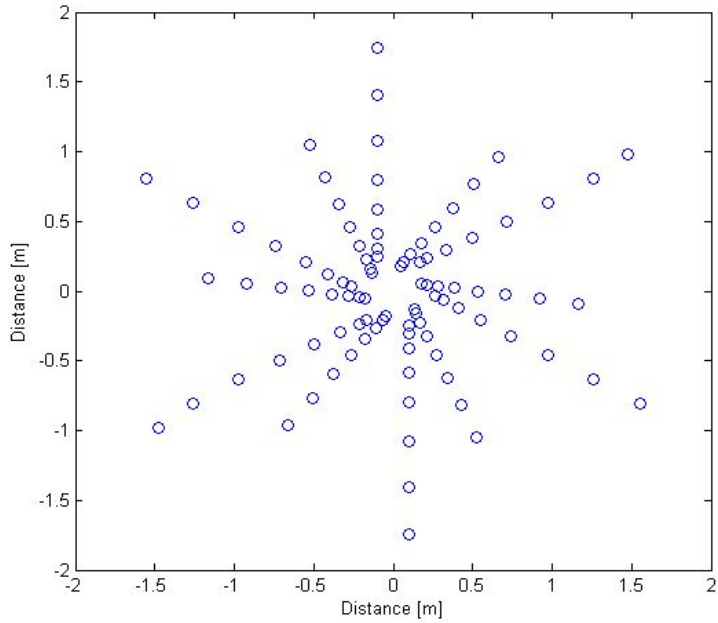


Figure 2-44 96-channel radial microphone array with centralized shapes

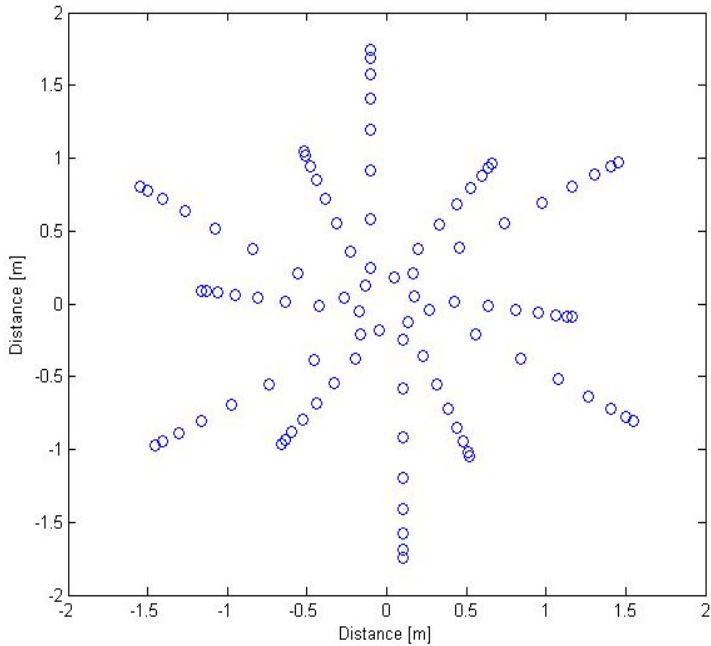


Figure 2-45 96-channel radial microphone array with dispersed shapes

The irregular configuration of the array is an important difference between beamforming and near-field acoustic holograph (NAH). Beamforming can use irregular array geometries such as random array geometries. The use of a discrete set of measurement positions on a plane can be seen as a spatial sampling of the sound field. NAH requires a regular, rectangular grid of points in order to apply a spatial discrete Fourier transform. Outside the near-field region, such a regular grid will suppress spatial aliasing effects very well, if the grid spacing is just less than half a wavelength. When the grid spacing exceeds half a wavelength, spatial aliasing components quickly get very disturbing.

Irregular arrays on the other hand can potentially provide a much smoother transition: spatial aliasing effects can be kept at an acceptable level up to a much higher frequency with the same average spatial sampling density. This indicates why beamforming can measure up to high frequencies with a fairly low number of microphones.

Simulation tests about the various 96-channel arrays were performed in order to verify source identification. First, three sources were located in a prediction plane as shown in Figure 2-46 and source location test at the frequencies of were conducted by using National Instrument's Microphone Array Startup.

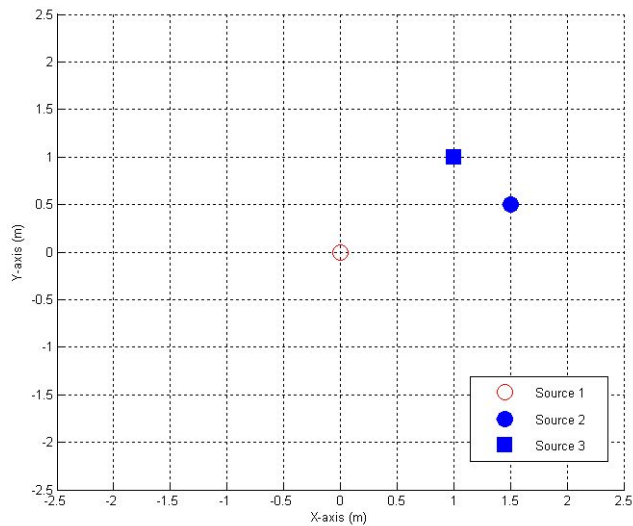


Figure 2-46 Source positions used for performance simulations

Figure 2-47 shows the resolution test result of the 96-channel rectangular array. The advantage of the rectangular array is simple development and installation. However, it has poor resolution in the high frequency by spatial aliasing. At the low frequency of 500 Hz, the three sources were not identified with the array. Moreover, lots of grating lobes were occurred in the high frequency of 2000 Hz.

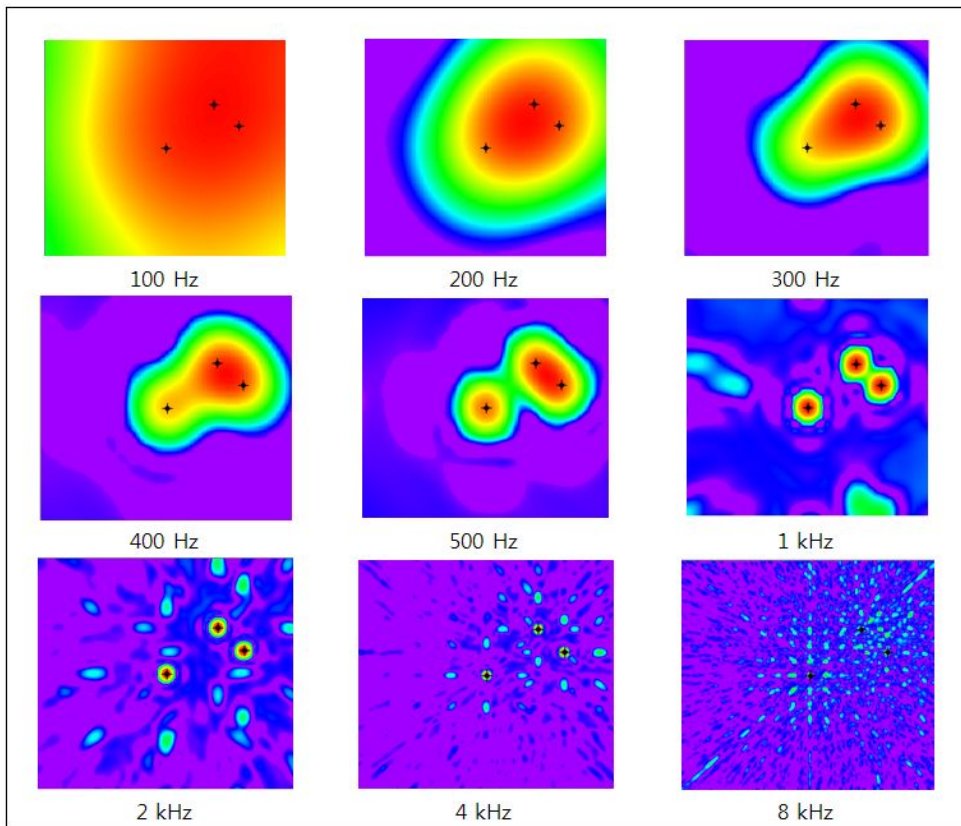


Figure 2-47 Resolution simulations of 96-channel rectangular array

(Relative level (dB): $-10 \leq$  ≤ 0)

The resolution result of the 96-channel radial array with same spacing was shown in Figure 2-48. The three sources were not also identified at the frequency of 500 Hz and some grating lobes were in the high frequency of 2000 Hz.

The 96-channel spiral arrays with centralized and dispersed shapes had little grating lobes at the high frequency of 2000 Hz as shown in Figure 2-49 and Figure 2-50. The 96-channel spiral array with dispersed shaped also had little grating lobes at the high frequency of 2000 Hz. The main difference between the two microphone arrays was the locations of the lobes. The lobes in the centralized shapes were at longer distances from the center. From the array resolution simulation, it was concluded that non-periodic microphone placement, which are the locations of the spatial sampling points, makes the analysis of spatial aliasing difficult. Therefore, it is concluded that the 96-channel spiral array with centralized shape has best resolution among the others. In addition, the various 96-channel spiral arrays were not able to identify three sources in the frequency of 500 Hz, too. This means that

resolution in the low frequency is not related with configuration but overall size of the array.

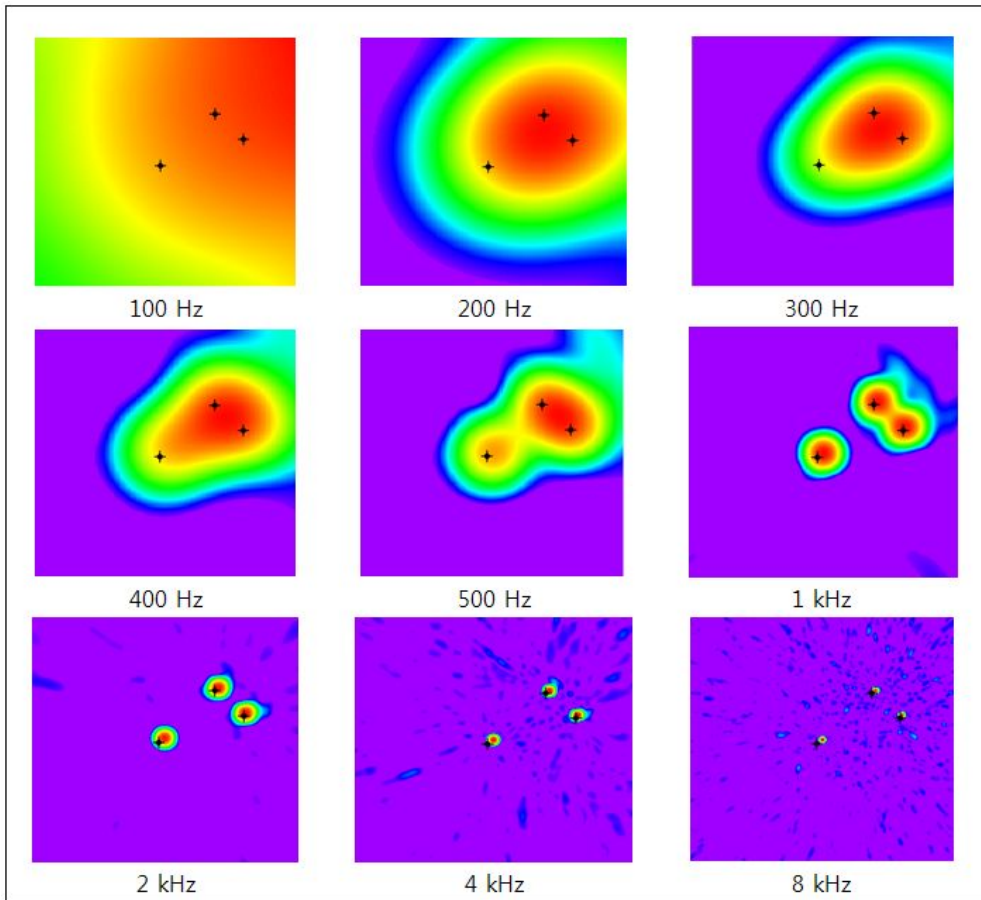


Figure 2-48 Resolution simulations of 96-channel radial array with same spacing (Relative level (dB): $-10 \leq$  ≤ 0)

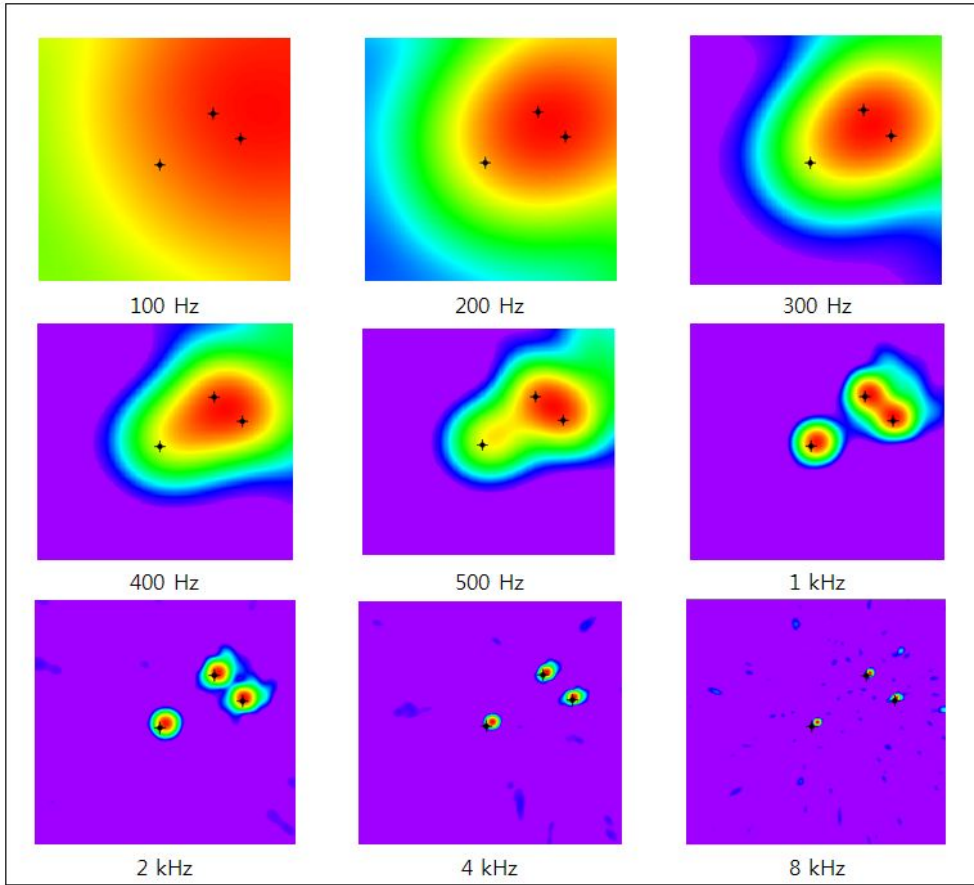


Figure 2-49 Resolution simulations of 96-channel radial array with centralized shapes

(Relative level (dB): $-10 \leq$  ≤ 0)

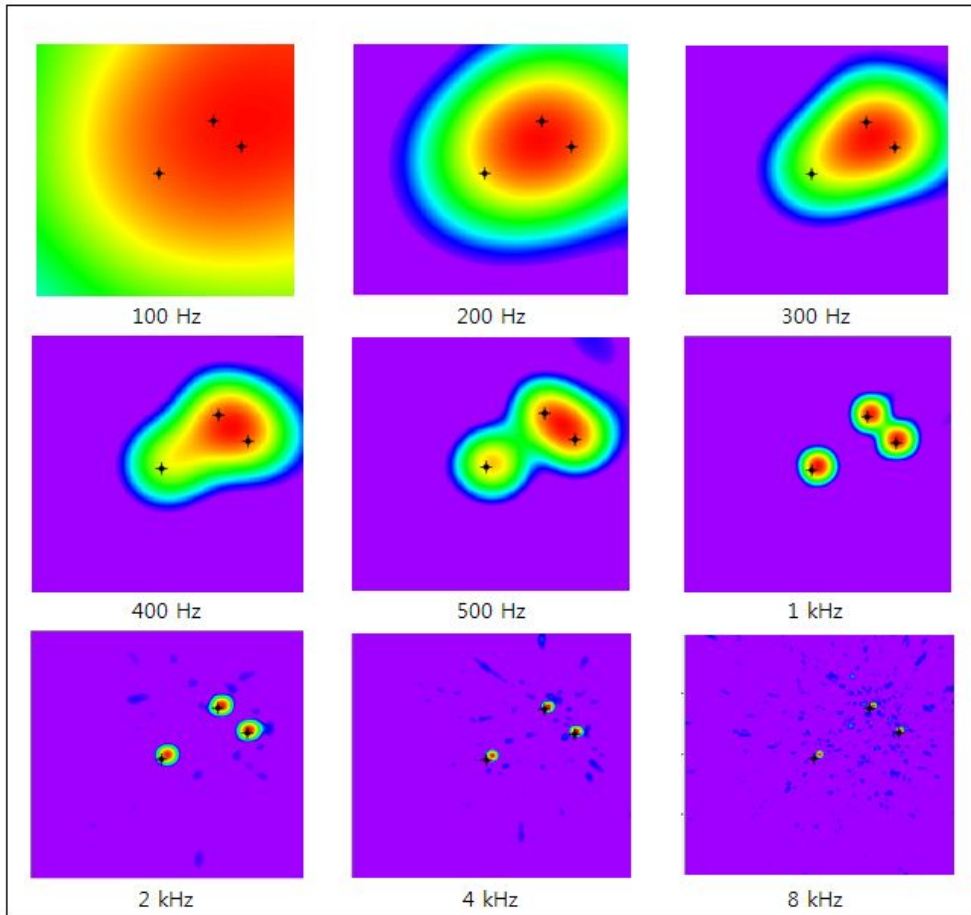


Figure 2-50 Resolution simulations of 96-channel radial array with dispersed shapes

(Relative level (dB): $-10 \leq$  ≤ 0)

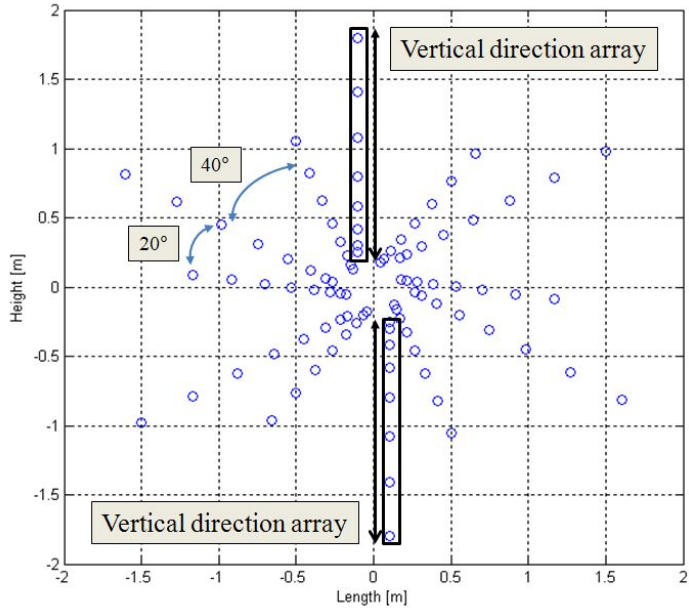


Figure 2-51 Design of 96-channel microphone array

The 96 channel radial array was designed as shown in Figure 2-51, and co-array pattern of the array was investigated as shown in Figure 2-52. The overall array configuration is radial and irregular. The diameter of the array is 3.592 m, and the microphones are spaced at intervals of 0.03575 ~ 3.592 m. Moreover, nested arrays with radii of 1.75 m and 1 m and containing eight microphones each are arranged at 20° and 40° angles, respectively. Via these nested arrays, which enclose a number of measurement cables, the installation time could be considerably reduced. Moreover, the acoustic emission characteristics in the vertical direction can be measured by the vertical

placement of the microphones in the nested array. From the investigation of the co-array pattern of the array configuration, an improved resolution at high frequencies was expected from the high density in the heart of the pattern. The irregular spaces between microphone positions minimized the redundancy of the pattern.

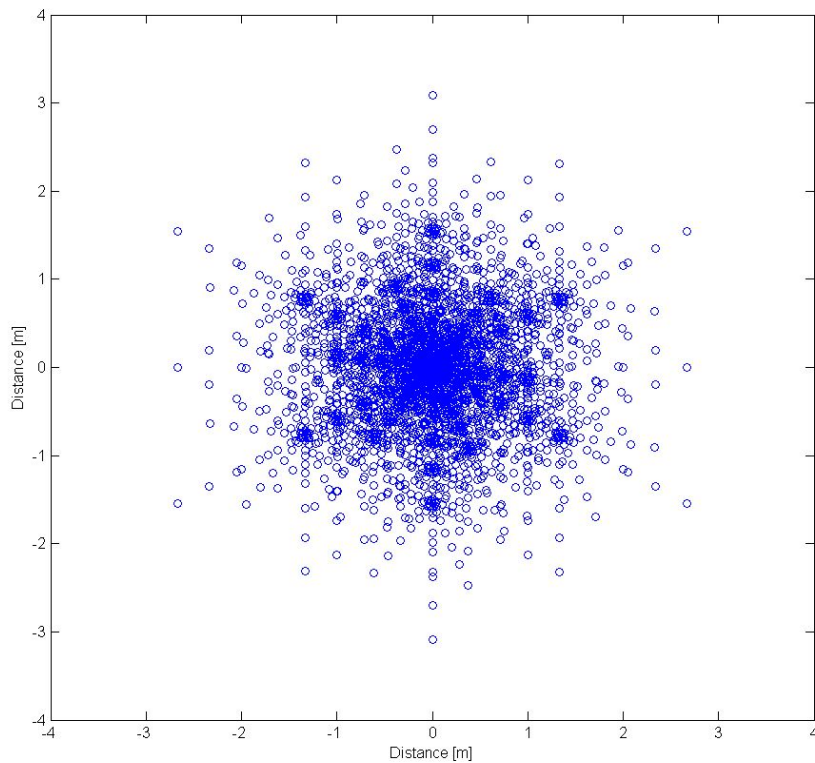


Figure 2-52 Co-array pattern of 96-channel microphone array

A simulation test for an array of sound sources was also performed. In this simulation, three monopoles that generated sound at specific frequencies were

placed at a distance of 5 m from the array. As shown in Figure 2-49, at 2000 Hz, microphone array clearly separated the three sound sources. In addition, ghost images seldom appeared in the overall frequency ranges.

After the simulation test, a resolution performance test was conducted with a manufactured microphone array (BSWA, 1/4") as shown in Figure 2-53. Signals were generated by a signal generator (AFG-320) at specific frequencies and radiated through a power amplifier (ANAM, AA-40) and a speaker (JBL, Control Xtreme) at a distance of 5 m from the array as shown in Figure 2-54. The signals were measured by a DAQ device (National Instruments PXI) with a sampling frequency of 25.6 kHz, and the beam power outputs were calculated over a frequency range of 31.5 ~ 8000 Hz (octave band). The calculated beam powers were projected on a 30 m long prediction square, as shown in Figure 2-55. The beam power output data were used to obtain the 3 dB bandwidth and MSL of the microphone array system. The 3 dB bandwidth decreased rapidly from 100 Hz and had a value of less than 5 m from 200 Hz. The MSL decreased from 63 Hz and had values of less than -10

dB from about 200 Hz.



Figure 2-53 96-channel microphone array setup



Figure 2-54 Resolution test setup

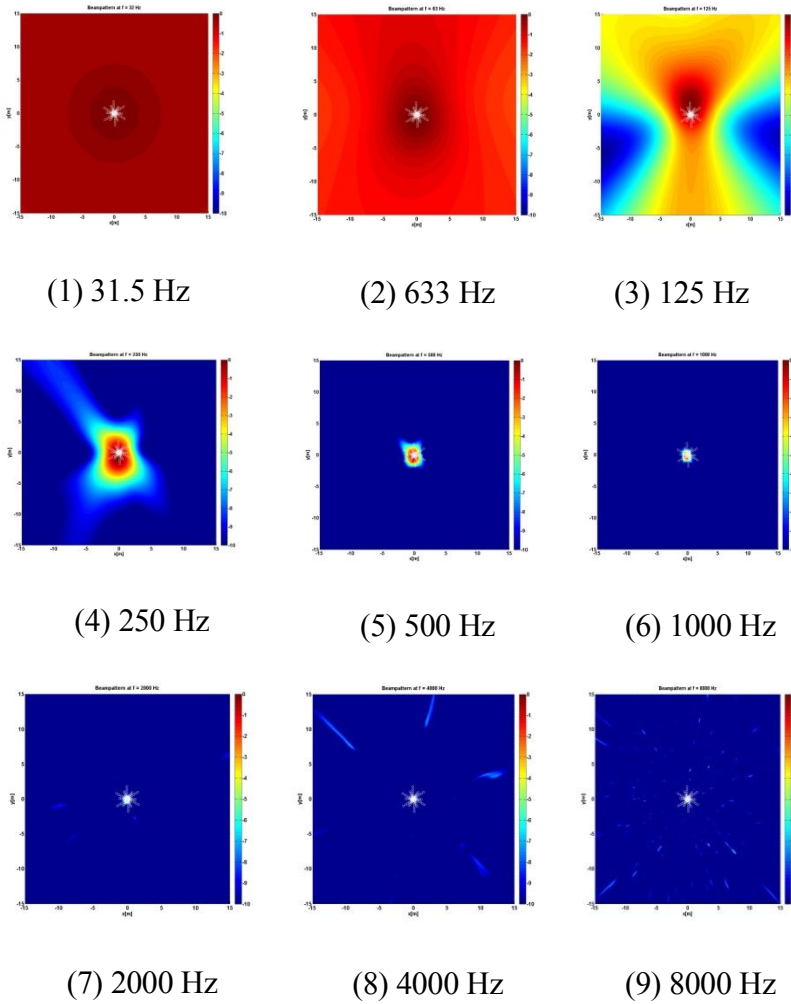


Figure 2-55 Results of resolution test at various frequencies

(Relative level (dB): $-10 \leq$  ≤ 0)

The 3 dB bandwidth and MSL are summarized in Table 2-1. In conclusion, the results of the verification tests show that the 96-channel microphone array created in this study is reliable for sound localization from 200 to 8000 Hz.

Table 2-1 3 dB bandwidth and maximum side-lobe level (MSL) of 96-channel microphone array

	500Hz	1000Hz	2000Hz	4000Hz	8000Hz
3-dB bandwidth	1.90m	0.95m	0.45m	0.15m	0.10m
MSL (Relative dB)	-15.0dB	-9.81dB	-8.10dB	-7.27dB	-5.19dB

2.3 Applications and discussions

In this section, noise sources identification of the vehicle with multiple sources was conducted with the designed microphone array. The sound visualization algorithm was verified with a moving vehicle attached noise sources at specific positions. After verification tests, noise source identification of high-speed trains was conducted. Measured values should be added by delay-and-sum based on the location of each microphone of the array.

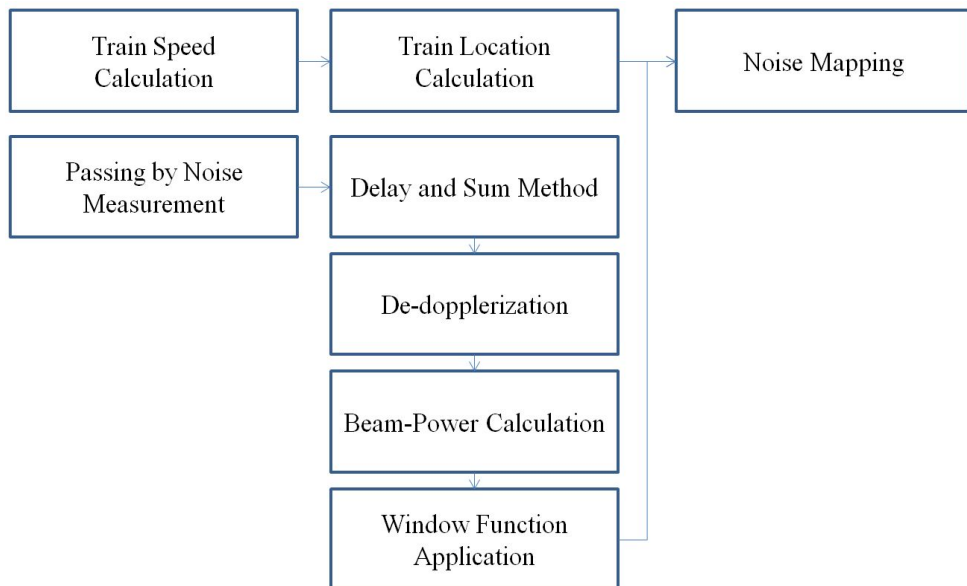


Figure 2-56 Workflow of noise mapping method

The process of sound visualization implemented in this study was summarized in Figure 2-56. As mentioned above, it is important to identify

locations of noise sources in order to derive noise source of moving sources. Moreover, Doppler effect and pressure reduction over the distance should be considered. Sound maps could be obtained from projecting the measured values on the prediction plane.

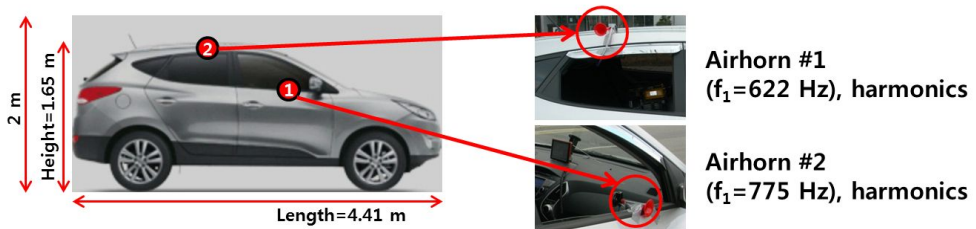


Figure 2-57 Vehicle validation test

Validation tests were conducted, in which the pass-by noise of a moving vehicle was measured to identify the locations of the noise sources. Horns were attached to the vehicle, as shown in Figure 2-57. The horns generated harmonic noise at frequencies of 622 Hz and 775 Hz while the vehicle was in motion. It is important to measure the noise and speed of the moving vehicle for obtaining noise maps. The vehicle traveled at a speed of 40 km/h in a horizontal direction. The 96-channel microphone array measured the noise of the moving vehicle from a distance of 5 m. Then, the delay-and-sum method was applied to compensate for the positions of the microphones. Finally, the

beampower obtained in this method projected onto a prediction plane. As shown in Figure 2-58, the implemented microphone array system performed noise source localization by calculating the exact positions of the horns.

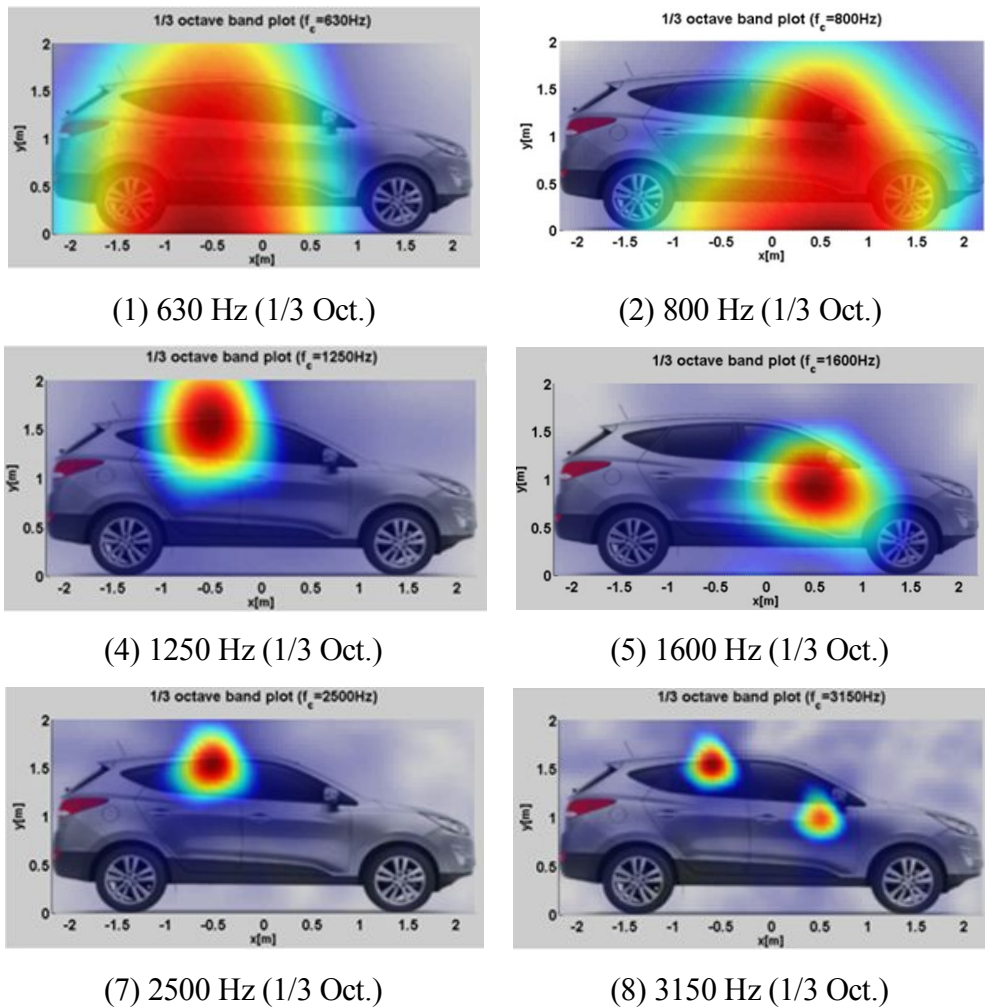


Figure 2-58 Noise maps of moving vehicle

(Relative level (dB): $-10 \leq$  ≤ 0)

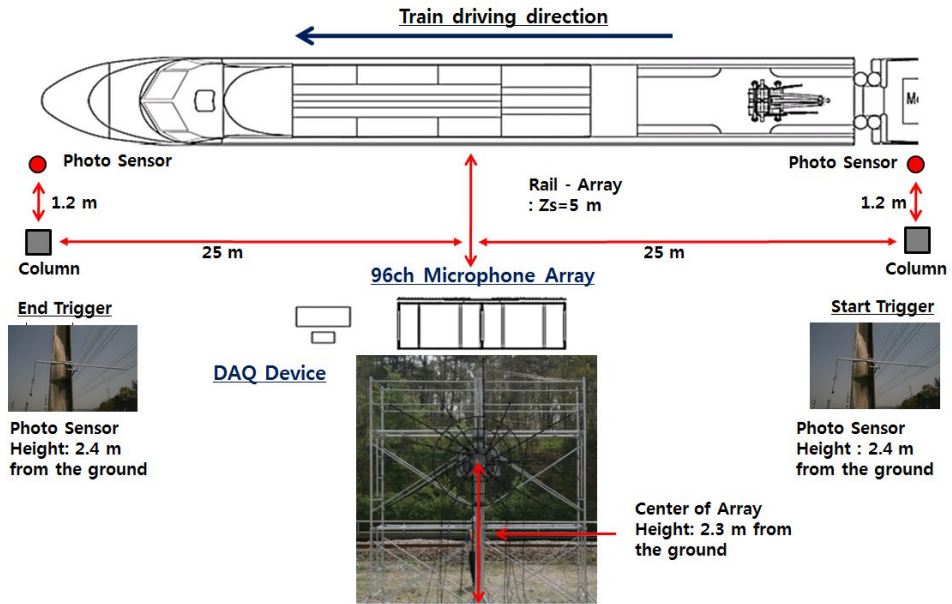


Figure 2-59 Microphone array measurement setup

After this successful test with a moving vehicle, the process was applied to high-speed trains, as shown in Figure 2-59. First, photoelectric sensors to measure the speed of a high-speed train were installed on two pillars of the rail. The speed was determined by calculating the pass-by time and the distance between these two pillars. Then, the 96-channel microphone array was placed at a horizontal distance of 5 m from the outside rail. The height of the center of the array was 2.3 m from the upper surface of the rail. Data measurement and analysis were conducted using PXI devices (DAQ board: PXIe-1065, controller: PXIe-8133, data streaming: NI 8260) from National Instruments.

Data from a KTX-Sancheon travelling at a speed of 300 km/h was measured on the Gyeongbu high-speed line.

The microphone array placement in the vicinity of the rails has practical constraints. First, there is a time constraint for the installment of the measurement equipment because of railway safety laws. In general, the installation of 70 to 100 microphones can take a long time, which could cause serious accidents. Therefore, measurement devices that can be quickly installed should be considered. In addition, operational speeds range from 150 to 300 km/h because the high-speed lines in Korea have various route distances from 30.0 to 73.0 km. Therefore, the radiation noise from various operational speeds should be measured using a microphone array.

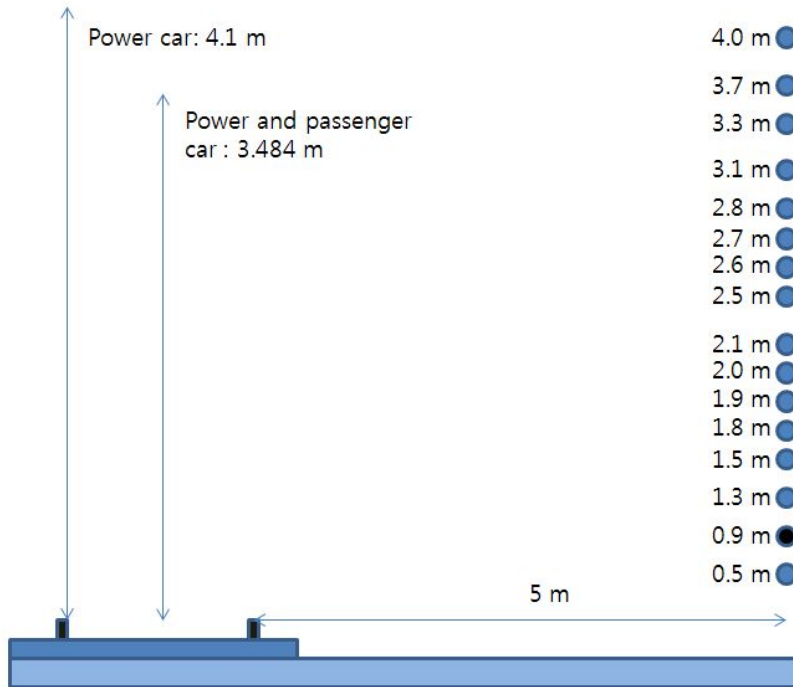


Figure 2-60 Microphone locations for noise measurements

Noise measurement at a position and directivity pattern in the vertical direction were investigated. A microphone placed at 0.9 m from the ground was used for noise measurement and 16 microphones were used for investigation of vertical directivity pattern of the high-speed train as shown in Figure 2-60. Table 2-2 shows the information about the measurement locations and the speeds of high-speed trains.

Table 2-2 Measurement sites and speeds of high-speed trains

NO	Speed (Km/h)	Site	NO	Speed (Km/h)	Site
1	148.4	Gangok Station	17	260.1	Cheonna-Asan
2	156.8	Gangok Station	18	260.5	Cheonna-Asan
3	157.1	Gangok Station	19	262.8	Cheonna-Asan
4	157.1	Gangok Station	20	263.1	Cheonna-Asan
5	176.3	Cheonna-Asan	21	265.5	Cheonna-Asan
6	218.1	Cheonna-Asan	22	266.2	Songna-ri
7	223.4	Cheonna-Asan	23	270.0	Cheonna-Asan
8	230.8	Cheonna-Asan	24	271.2	Cheonna-Asan
9	233.7	Cheonna-Asan	25	295.5	Songna-ri
10	237.7	Cheonna-Asan	26	298.8	Songna-ri
11	238.9	Cheonna-Asan	27	301.0	Songna-ri
12	242.1	Cheonna-Asan	28	301.5	Songna-ri
13	243.3	Cheonna-Asan	29	301.5	Songna-ri
14	244.2	Cheonna-Asan	30	301.5	Songna-ri
15	246.0	Cheonna-Asan	31	303.3	Songna-ri
16	252.7	Cheonna-Asan	32	306.6	Songna-ri

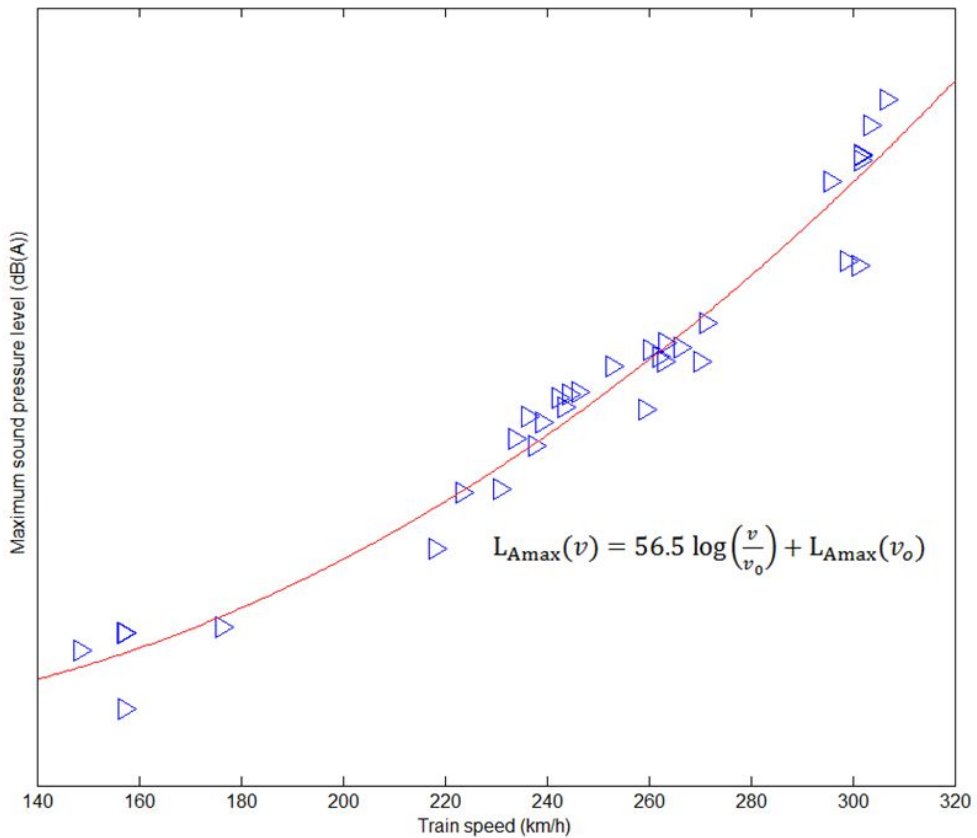


Figure 2-61 Maximum A-weighted sound pressure levels of high-speed trains at speeds from 150 to 300 km/h

Maximum sound pressures were increased with the speeds increase as shown in Figure 2-61. From the results, regression law can be derived as follows:

$$L_{Amax}(v) = 56.5 \log\left(\frac{v}{v_0}\right) + L_{Amax}(v_0) \quad (2-52)$$

where $L_{Amax}(v)$ means A-weighted sound pressure level at the speed of v km/h and v_0 is the reference speed of 150 km/h.

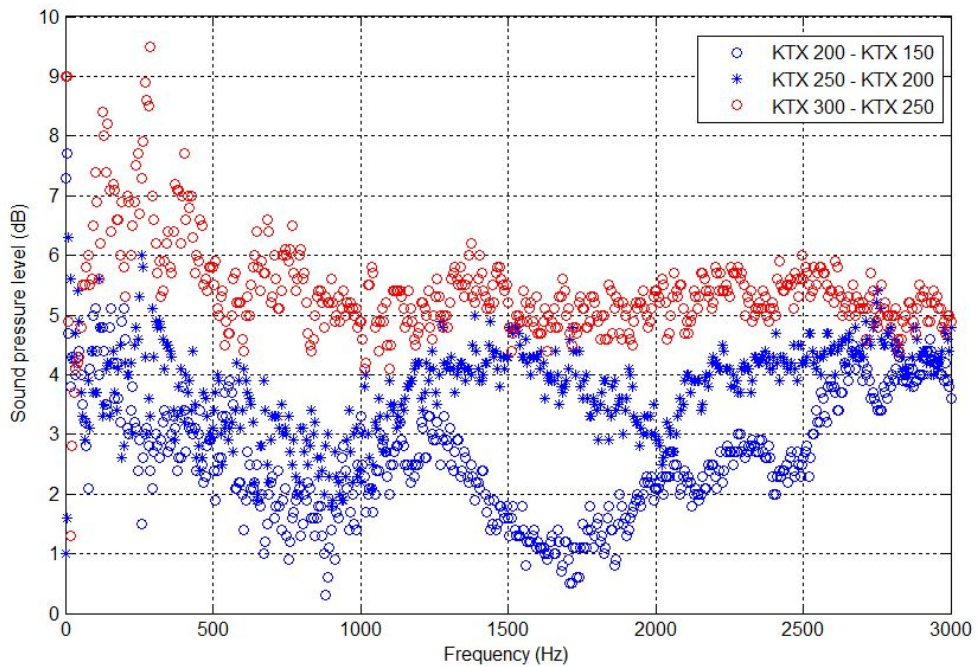


Figure 2-62 Difference in A-weighted sound pressure levels of high-speed trains

To examine the sound characteristics according to speed increases in the frequency domain, pressure difference at speeds from 150 to 300 km/h was obtained from 0 to 3000 Hz as shown in Figure 2-62. The pressure values of 300 km/h, 250 km/h and 150 km/h were used as the measured signals in Songra tunnel, Cheonan-Asan station and Gamgok station, respectively. The pressure value of 200 km/h was interpolated from data of 176.3 and 218.1 km/h. Sound pressure levels of 1 ~ 4 dB was increased by examining the results from 150 to 200 km/h and the high increases of the pressure were in the 200 Hz, 1300 Hz and 2500 ~ 3000 Hz. Sound pressures of 2 ~ 5 dB were increased from 200 to 250 km/h and the increase was in the frequency of below 500 Hz, 1500 Hz and 3000 Hz. Moreover, 5 ~ 6 dB sound pressures were increased from 250 to 300 km/h and the increases in the over frequency from 500 to 3000 Hz. From the results, the noise generation of the high-speed train increased exponentially, and the noise characteristics were also changed according to the speed increase. However, with a single microphone measurement, the exact noise source could not be identified.

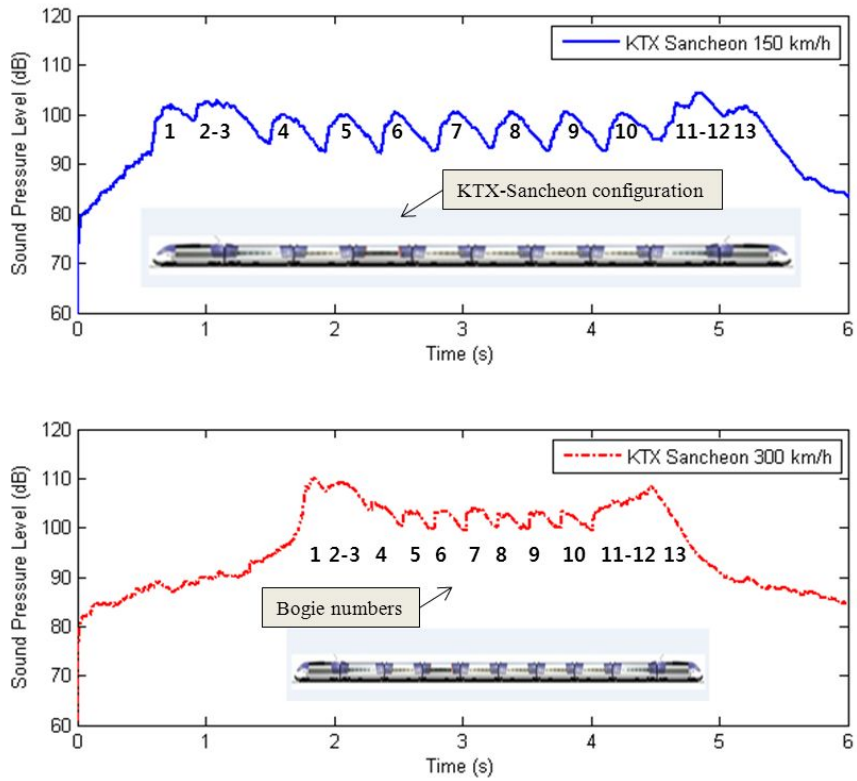


Figure 2-63 Tim-history of sound pressure level from pass-by high-speed trains

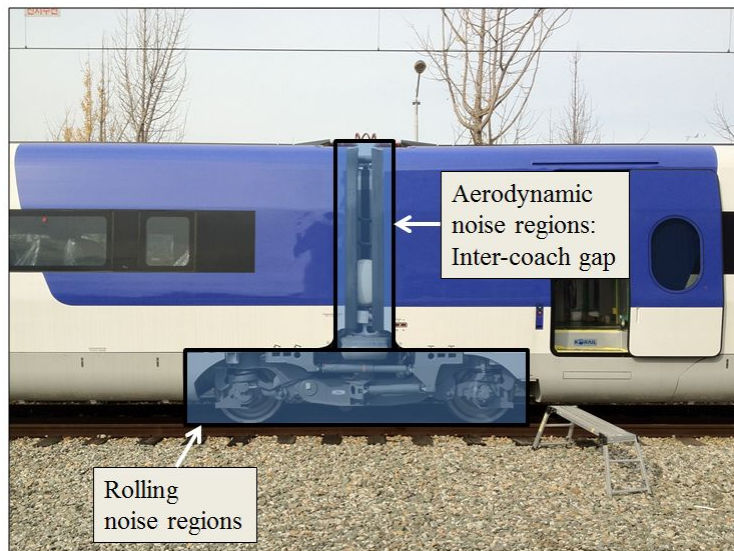


Figure 2-64 Noise sources in section between cars

The time-history of the sound pressure level during a pass-by of a high-speed train at speeds between 150 and 300 km/h was drawn to identify the noise sources, as shown in Figure 2-63. The measurement was conducted with a microphone of the array, which placed at 0.9 m from the rail. From the fact that the number of sound pressure peaks is equal to that of the bogies and inter-coach spacing of the high-speed train, it was confirmed that the noise peaks were generated dominantly from the areas of the bogies or inter-coach spacing as shown in Figure 2-64. From the results, the between-cars section such as inter-coach spacing and bogies are dominant noise generating areas for the high-speed train. The high sound pressure at the bogie areas was considered as rolling noises of wheel and rail contact. The noise from first and second power cars was higher than the other bogies.

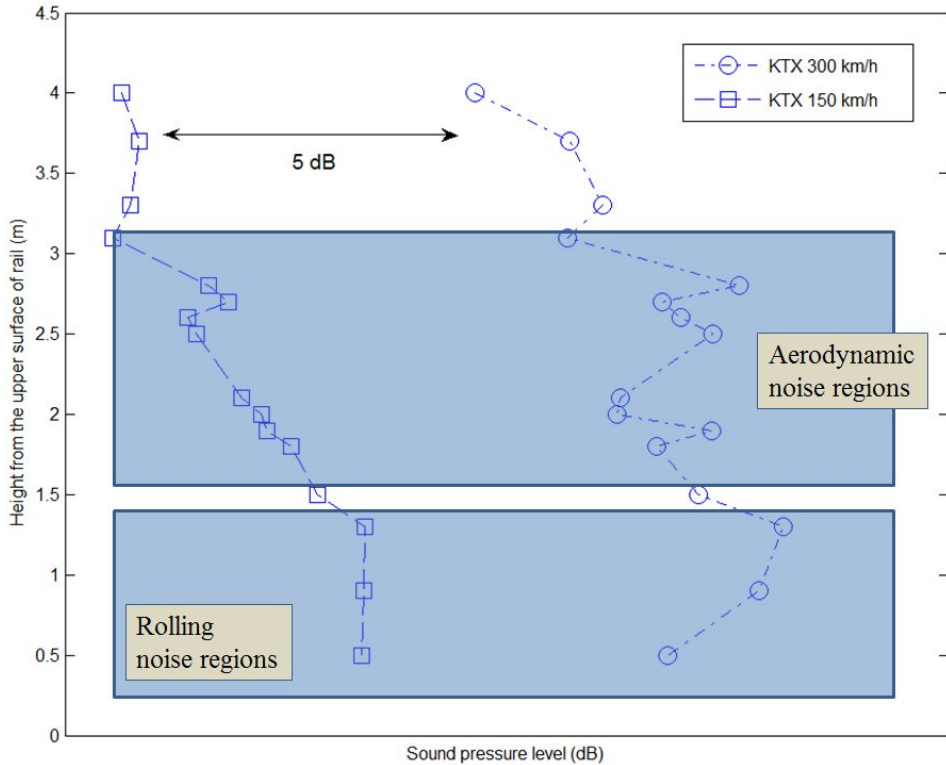


Figure 2-65 Vertical distribution of sound pressure levels

Furthermore, from an observation of the vertical distribution of the sound pressure level measured from the microphones placed in the vertical direction. Not only the rolling noise from the bogies, but also the aerodynamic noises from the pantograph and inter-coach spacing were the main noise source areas with an increase in speed as shown in Figure 2-65. The simple estimation of the source was conducted with a 1-dimension line array. However, for the exact noise source localization, 2-dimension array analysis needs.

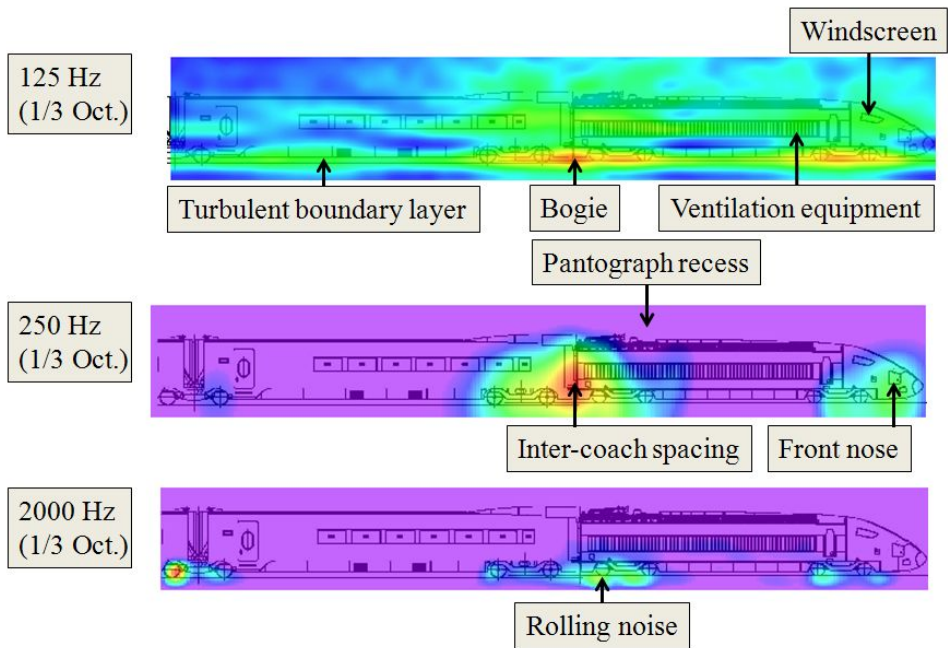


Figure 2-66 Noise maps of leading power car

(Relative level (dB): $-10 \leq$  ≤ 0)

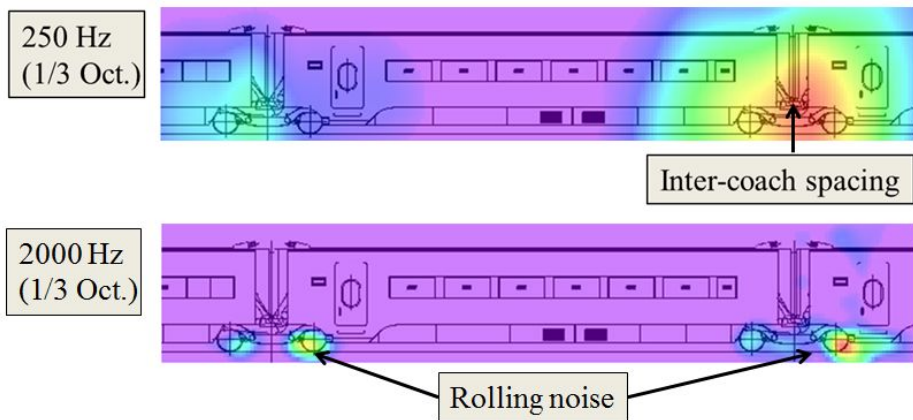


Figure 2-67 Noise maps of between-cars section

(Relative level (dB): $-10 \leq$  ≤ 0)

From noise maps, the noise sources from the leading power car to trailing power car were specifically proposed. In the leading power car with the cab

(or first car) of a high-speed train, the first bogie, second bogie, windscreen, front nose, pantograph, and ventilation equipment were noise sources as shown in Figure 2-66. In the leading power and passenger car (or second car), the first bogie, bogie area, and cavity between cars were main noise sources. In the between-cars section, inter-coach spacing was a main noise source in the low frequency of 250 Hz and rolling noise in the high frequency of 2000 Hz as shown in Figure 2-67.

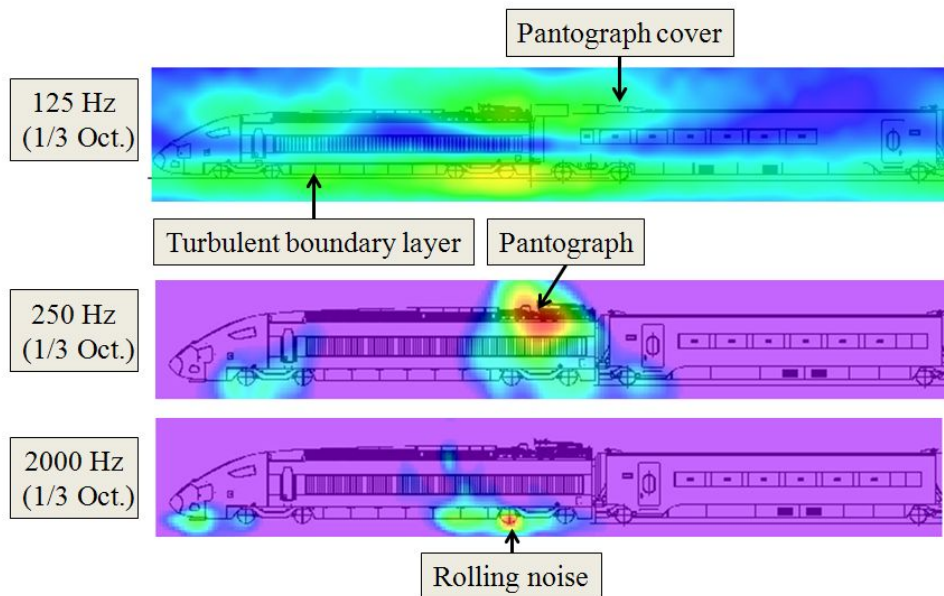


Figure 2-68 Noise maps of trailing power car

(Relative level (dB): $-10 \leq$ [color scale] ≤ 0)

These were also noise sources in the trailing power and passenger car as shown in Figure 2-68. In the passenger cars, the bogies and cavities between cars were noise sources. In the trailing power car, the last and first bogies, and the pantograph were noise sources from noise maps. The detailed investigation of the noise sources in the high-speed trains based on the noise maps by using beamforming method was performed as shown in Table 2-3. In this dissertation, rail noise did not appear because all noise sources were assumed as incoherently monopoles [2.36].

In summary, a noise-source localization algorithm in the time domain was developed, and verification of the moving vehicle was conducted in this chapter. It is difficult to establish effective noise reduction measures because there is a wide range of equipment in a confined space. If we can visualize noise in the space, effective noise measures can be established from the identified noise sources and noise propagation path analysis.

Table 2-3 Identified noise sources of high-speed trains

	Noise sources
Leading power car	First bogie, Second bogie Front glass, Front nose Pantograph, Ventilation
Leading power and passenger car	First bogie Bogie between cars Cavity between cars
Passenger car	Cavity between cars Bogie between cars
Trailing power and passenger car	First bogie Bogie between cars Cavity between cars
Trailing power car	Last bogie First bogie Pantograph

3. Resolution improvement by inverse problem optimization

Generally, the noise signals of a moving vehicle are not stationary and ergodic. Therefore, the estimation of sound source positions is error-prone if we use a sound visualization technique that is sensitive to the measured signals. In this sense, the microphone array system based on the beamforming method is useful for visualizing the sound field in driving vehicles because it is not sensitive to measured signals [3.1-3.3].

However, the poor resolution at low frequencies is the main disadvantage of the beamforming method [3.4], as it does not identify the exact noise source positions of low-frequency noise sources. For example, it is difficult to confirm the location of the noise sources with the beamforming method in the pantograph and pantograph cover of the high-speed train owing to multiple low-frequency noise sources.

To improve the poor resolution in the low frequency region, the inverse method was used in the various researches. The inverse method was used to optimize the location of sources from the inverse problem [3.5]. However, it

was known that the inverse problem is easily ill-conditioned and sensitive to measurement results. To alleviate the limitations of the inverse problem, a number of improved algorithms have been developed, mainly in the context of Astronomy and geophysical, radar, sonar and telecommunication applications [3.6-3.8]. However, effective algorithms for the multiple moving sources are limited.

For example, the ESPRIT [3.9] method is the improved algorithm of the inverse method, but require special array geometries such as the uniform linear array. Therefore, this method may not be applied for arbitrary array geometries as used in acoustic testing. The minimum variance beamformer also provides a better spatial resolution than the conventional beamformer. The improved variants [3.10] of this beamformer were used in aeroacoustic measurements [3.11] and acoustic imaging [3.12-3.14]. However, the performance of these algorithms regarding estimation of absolute levels depends on the number of sources present and on the signal-to-noise ratio. In MUSIC (Multiple Signal Classification) algorithm, an eigenvalue decomposition of the cross spectral

matrix separates signal and noise eigenvectors and the estimation of source position or direction of arrival is solely computed from the noise eigenvectors [3.15]. Thus, amplitude information is lost entirely during the processing and no estimation of absolute source levels is possible.

On the other hand, the deconvolution approach which resolves the divergence or ill-condition in the inverse problem solution is an effective way to visualize moving sources. The deconvolution method had been primarily used for improving the optical images in Astronomy and CLEAN algorithm. The CLEAN algorithm originally introduced in radio astronomy basically removes the side lobes from the beamforming map. It has been used for aeroacoustic measurements [3.16]. Improved variants of this algorithm, namely WB-CLEAN [3.17] and CLEAN-SC [3.18] were also applied in the context of acoustic testing. The methods have been widely applied to a variety of fields such as jet noise visualization in Aviation engineering [3.19-3.25].

This chapter presents the research that was conducted to improve the resolution on the basis of the deconvolution method. First, the formulae of the

deconvolution methods were examined in Section 3.1. In particular, the relationship between the beamformer output and the point spread function was investigated, and the well-conditioned inverse problem with non-negative constraints was verified. Then, the algorithm developed for a moving source was presented in Section 3.2. After deducing the point-spread function from the beamformer output in the prediction plane, the inverse optimization problem was solved by an iterative approach. Generally, the deconvolution approaches for improving the sound visualization of a moving source were conducted in the frequency domain; thus, deducing point spread function requires complex calculations to compensate for Doppler effect. However, in this research, the calculation of the beamformer in the time domain and the deduced point spread function in the frequency domain were conducted for reducing computing times. Finally, the application to a high-speed vehicle was presented, and the exact noise-source locations at low frequencies were identified in Section 3.3.

3.1 Resolution improvement algorithm

In this section, the theoretical background and the algorithm implement for the resolution improvement were introduced. As mentioned in the previous chapter, the advantage of the beamforming method is not sensitive to the measured signal so it is effective to localize noise sources in the moving vehicle. However, its disadvantage of the method is poor resolution in the low-frequency region. Therefore, the theoretical studies were conducted to improve the resolution by using deconvolution method in this section [3.26].

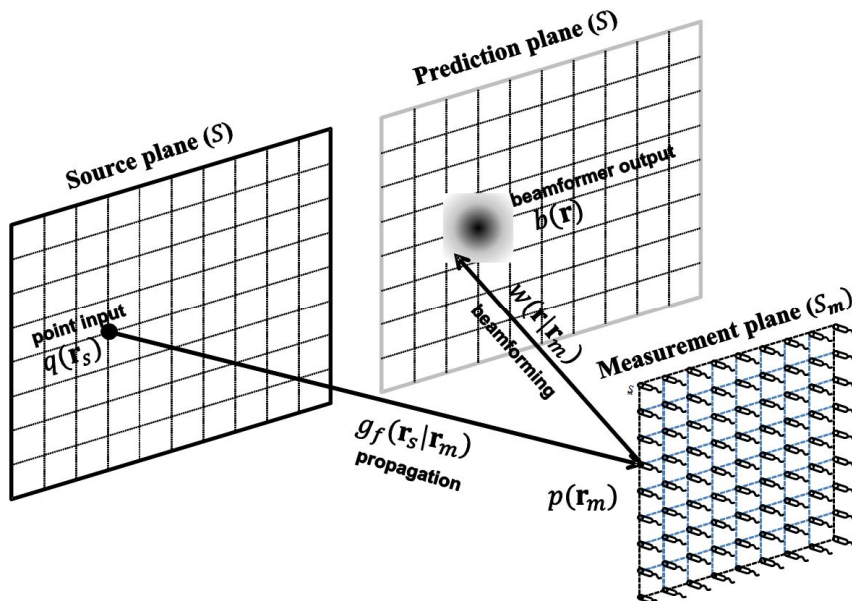


Figure 3-1 Concept of point input in source plane and beamformer output in prediction plane

In this research, post-processing techniques based on the image processing technique of deconvolution were used to enhance the obtained beamforming image. To begin, we assume a single frequency component of the measured sound field, and hence, the frequency dependency ω will be omitted. Suppose that we have monopole sound sources distributed on a source plane shown in Figure 3-1. If the complex amplitudes of the sources are denoted by $q(\mathbf{r}_s)$, then the final goal of beamforming is to find the exact location of the sound sources by predicting the distribution of q . When a single monopole source at \mathbf{r}_s is excited, then a sound field is generated and propagates to the location of the microphone array. The pressure field Green's function from \mathbf{r}_s to the measurement position \mathbf{r}_m . If all the sound fields from all monopoles are superposed, then the sound field can be described as

$$p(\mathbf{r}_m) = \int_{S_m} g_f(\mathbf{r}_m|\mathbf{r}_s)q(\mathbf{r}_s)dS(\mathbf{r}_s) \quad (3-1)$$

where the measurement position \mathbf{r}_m is the finite measurement plane S_m .

To predict the excitation function q from the measurement taken at S_m , the measured pressure field is multiplied by a scan vector to produce the

beamformer output. Our aim is to predict the source distribution in the source plane, and hence the scan vector for predicting the source excitation in S can be denoted as $(\mathbf{r}|\mathbf{r}_m)$;

$$b(\mathbf{r}) = \int_S w(\mathbf{r}|\mathbf{r}_m)p(\mathbf{r}_m)dS_m \quad (3-2)$$

where the prediction point is again in the source plane. The whole beamforming process from the source excitation $q(\mathbf{r}_s)$ to the beamformer output $b(\mathbf{r})$ can be summarized as

$$b(\mathbf{r}) = \int_{S_m} \int_S [w(\mathbf{r}|\mathbf{r}_m)g_f(\mathbf{r}_m|\mathbf{r}_s)q(\mathbf{r}_s)] dS(\mathbf{r}_s)dS_m(\mathbf{r}_m) \quad (3-3)$$

Therefore, the excitation function $q(\mathbf{r}_s)$ experiences two transforms when being converted to the beamformer output $b(\mathbf{r})$.

The transform of (3-3) can be further simplified if the shift invariant properties of the scan vector and free-field Green's function are exploited. The shift invariance, denoted as

$$w(\mathbf{r}|\mathbf{r}_m) = w(\mathbf{r} - \mathbf{r}_m), \quad g_f(\mathbf{r}_m|\mathbf{r}_s) = g_f(\mathbf{r}_m - \mathbf{r}_s) \quad (3-4)$$

implies the function w and g_f are only a function of the relative distance between two positions, rather than the absolute position \mathbf{r}_m or \mathbf{r}_s . It can be

easily shown that the free-field Green's function

$$g_f(\mathbf{r}_m | \mathbf{r}_s) = \frac{e^{ik|\mathbf{r}_m - \mathbf{r}_s|}}{4\pi|\mathbf{r}_m - \mathbf{r}_s|} \quad (3-5)$$

satisfies shift invariance, and the scan vector derived from the planar or spherical wavefront model also fulfills this property. For example, the plane wave model with a wavenumber vector \mathbf{k} can be written as a function of $-\mathbf{r}_m$:

$$w(\mathbf{r} | \mathbf{r}_m) = e^{i\mathbf{k} \cdot (\mathbf{r} - \mathbf{r}_m)} \quad (3-6)$$

If the two transforms satisfy shift invariance, the whole beamforming process of (3-3) can be described as two spatial convolutions:

$$\begin{aligned} b(\mathbf{r}) &= \int_{S_m} \int_S [w(\mathbf{r} - \mathbf{r}_m) g_f(\mathbf{r}_m - \mathbf{r}_s) q(\mathbf{r}_s)] dS(\mathbf{r}_s) dS_m(\mathbf{r}_m) \\ &= w(\mathbf{r}) *_s (g_f(\mathbf{r}) *_s q(\mathbf{r})) \\ &= (w(\mathbf{r}) *_s g_r(\mathbf{r})) *_s q(\mathbf{r}) \end{aligned} \quad (3-7)$$

where $*_s$ denotes the spatial convolution operator defined by

$$f(\mathbf{r}) *_s g(\mathbf{r}) = \int_S f(\mathbf{r} - \mathbf{r}') g(\mathbf{r}') dS(\mathbf{r}') \quad (3-8)$$

It is noteworthy that the whole process to convert the excitation function to the beamformer output is given by the spatial convolution. Therefore, the

beamforming process of (3-7) can be regarded as a system with an impulse response function $psf(\mathbf{r})$ given by

$$psf(\mathbf{r}) = w(\mathbf{r}) *_s g_f(\mathbf{r}) \quad (3-9)$$

When the excitation q is fed into the system, it is convolved with the impulse response $psf(\mathbf{r})$ to produce an output $b(\mathbf{r})$:

$$b(\mathbf{r}) = psf(\mathbf{r}) *_s q(\mathbf{r}) \quad (3-10)$$

Therefore, the unknown input to the system can be readily found from the given beamformer output b by solving an inverse system. Since the output of the system is equal to the spatial convolution of the impulse response and input signals, the inverse problem can be thought as a deconvolution of the impulse response from the output signals. That is,

$$q(\mathbf{r}) = psf(\mathbf{r}) *_s^{-1} b(\mathbf{r}) \quad (3-11)$$

where $*_s^{-1}$ denotes the deconvolution operator. The point spread function is determined primarily by the array design and the frequency, although the choice of weight vector can also be very important.

The convolution in the spatial domain is equivalent to multiplication in the

frequency domain [3.27, 3.28]. Therefore, equation (3-10) can be transposed to

$$\boldsymbol{\beta}(\mathbf{r}) = \mathbf{T}(\mathbf{r}) \mathbf{s}(\mathbf{r}) \quad (3-12)$$

where $\mathbf{s}(\mathbf{r})$, $\boldsymbol{\beta}(\mathbf{r})$ and $\mathbf{T}(\mathbf{r})$ are the spatial Fourier transforms of q , b and psf , respectively. From (3-9), $\mathbf{T}(\mathbf{r})$ can be expanded to

$$\mathbf{T}(\mathbf{r}) = \mathbf{W}(\mathbf{r}) G_f(\mathbf{r}) \quad (3-13)$$

where $\mathbf{W}(\mathbf{r})$ and $G_f(\mathbf{r})$ denotes the spatial Fourier transform of the scan vector w and the free-field Green's function g_f , respectively.

In the case of square matrix and linearly independent, the point spread function $\mathbf{T}(\mathbf{r})$ is invertible, so the source $\mathbf{s}(\mathbf{r})$ can be obtained as

$$\mathbf{s}(\mathbf{r}) = \mathbf{T}^{-1}(\mathbf{r}) \boldsymbol{\beta}(\mathbf{r}) \quad (3-14)$$

However, $\mathbf{T}(\mathbf{r})$ describes the response in a prediction plane to a point source, which is not one-to-one correspondence. Therefore, to obtain source positions with (3-14), optimization problem is applied as follows.

$$\text{Minimize } \|\boldsymbol{\varepsilon}\| = \|\boldsymbol{\beta} - \mathbf{T}\mathbf{s}\| \quad (3-15)$$

For the beamforming of a high-speed train, the measurement is usually taken in the far-field region away from the source, which makes \mathbf{T} relatively

small compared to the source \mathbf{s} . This means that the linear equation in equation (3-15) is ill-conditioned. In order to overcome this problem, non-negativity constraints were applied.

The non-negativity makes the inverse problem well-conditioned for the following reasons [3.29]:

We consider real $m \times n$ linear system of the form

$$\mathbf{Ax} = \mathbf{b} \quad (3-16)$$

where $m \geq n$, \mathbf{A} has full column rank, and subject to the non-negativity constraints.

A standard approach for estimating \mathbf{x} from \mathbf{b} is to compute a regularized approximate solution of the least squares minimization problem.

$$\min_{\mathbf{x}} \|\mathbf{Ax} - \mathbf{b}\|^2 \quad (3-17)$$

Regularized approximate solution methods are typically needed due to the fact that \mathbf{A} is ill-conditioned so replacing (3-17) by the non-negativity constrained least squares problem

$$\min_{\mathbf{x} \geq 0} \|\mathbf{Ax} - \mathbf{b}\|^2 \quad (3-18)$$

We can say that \mathbf{x} is feasible if $\mathbf{x} \geq 0$, and we defined the active set of any feasible x by

$$\mathcal{A}(\mathbf{x}) = \{i | x_i = 0\}, \quad (3-19)$$

We can then define the diagonal matrix by

$$[D(\mathbf{x})]_{ii} = \begin{cases} 0, & i \notin \mathcal{A}(\mathbf{x}) \\ 1, & i \in \mathcal{A}(\mathbf{x}) \end{cases}, \quad (3-20)$$

We now suppose that \mathbf{x}^* is a local solution and define the Karush-Kuhn-Tucker (KKT) conditions have the form [3.30]

$$[\mathbf{A}^T \mathbf{A} \mathbf{x}^* - \mathbf{A}^T \mathbf{b}]_i \geq 0, i = 1, \dots, n \quad (3-21)$$

$$\mathbf{x}^* \cdot [\mathbf{A}^T \mathbf{A} \mathbf{x}^* - \mathbf{A}^T \mathbf{b}]_i = 0, i = 1, \dots, n \quad (3-22)$$

We have the form (3-22) that all i such that $x_i^* > 0$,

$$[\mathbf{A}^T \mathbf{A} \mathbf{x}^* - \mathbf{A}^T \mathbf{b}]_i = 0 \quad (3-23)$$

This implies, using the fact that $\mathbf{D}^* \mathbf{x}^* = \mathbf{x}^*$, that

$$\mathbf{D}^* \mathbf{A}^T \mathbf{A} \mathbf{D}^* \mathbf{x}^* - \mathbf{D}^* \mathbf{A}^T \mathbf{b} = \mathbf{0} \quad (3-24)$$

which are the normal equations for

$$\min_{\mathbf{x}} \|\mathbf{A} \mathbf{D}^* \mathbf{x} - \mathbf{b}\|^2 \quad (3-25)$$

Our objective is to investigate and compare the stability of linear system (3-

17) and (3-25). For this we need to define the singular value decomposition

(SVD) of a matrix. The SVD of \mathbf{A} by

$$\mathbf{A} = \mathbf{U}\Sigma\mathbf{V}^T, \quad \Sigma = \begin{pmatrix} \Sigma_1 \\ \mathbf{0} \end{pmatrix} \quad (3-26)$$

where \mathbf{U} is an orthogonal matrix, \mathbf{V} is an $n \times n$ orthogonal matrix, and

Σ is $\Sigma_1 = \text{diag}(s_1, s_2, \dots, s_n)$ and $s_1 \geq s_2 \geq \dots \geq s_n$.

The pseudo-inverse of \mathbf{A} is given by

$$\mathbf{A}^\dagger = \mathbf{U}\Sigma^\dagger\mathbf{V}^T, \quad \Sigma^\dagger = \begin{pmatrix} \Sigma_1^{-1} \\ \mathbf{0} \end{pmatrix} \quad (3-27)$$

The condition number of \mathbf{A} is defined

$$\text{cond } \mathbf{A} = s_1/s_n \quad (3-28)$$

We say that \mathbf{A} is ill-conditioned if $\text{cond } \mathbf{A}$ is extremely large, which occurs,

we assume, due to the fact that $0 < s_n \ll 1$.

We may assume that

$$\mathbf{D}^* = \begin{pmatrix} \mathbf{I}_r & \mathbf{0} \\ \mathbf{0} & \mathbf{0} \end{pmatrix} \quad (3-29)$$

where $\mathbf{I}_r =$ identity matrix ($r \times r$) and $\mathbf{AD}^* = (\mathbf{A}_1 \ \mathbf{0})$.

This allows us to define both the pseudo-inverse and condition number of

\mathbf{AD}^* ; namely,

$$(\mathbf{AD}^*)^\dagger \stackrel{\text{def}}{=} \begin{pmatrix} \mathbf{A}_1^\dagger \\ 0 \end{pmatrix}, \quad (3-30)$$

and

$$\text{cond } \mathbf{AD}^* \stackrel{\text{def}}{=} \text{cond } \mathbf{A}_1 \quad (3-31)$$

We note that $r \leq n \leq m$. Then if $\mathbf{x} \in \mathbb{R}^r$, and we denote

$$\tilde{\mathbf{x}} = \begin{pmatrix} \mathbf{x} \\ 0 \end{pmatrix}, \quad (3-32)$$

We have

$$s_1(\mathbf{A}_1) = \max_{\mathbf{0} \neq \mathbf{x} \in \mathbb{R}^r} \frac{\|\mathbf{A}_1 \mathbf{x}\|}{\|\mathbf{x}\|} = \max_{\mathbf{0} \neq \mathbf{x} \in \mathbb{R}^r} \frac{\|\mathbf{A} \tilde{\mathbf{x}}\|}{\|\tilde{\mathbf{x}}\|} \leq s_1(\mathbf{A}) \quad (3-33)$$

$$s_r(\mathbf{A}_1) = \min_{\mathbf{0} \neq \mathbf{x} \in \mathbb{R}^r} \frac{\|\mathbf{A}_1 \mathbf{x}\|}{\|\mathbf{x}\|} = \min_{\mathbf{0} \neq \mathbf{x} \in \mathbb{R}^r} \frac{\|\mathbf{A} \tilde{\mathbf{x}}\|}{\|\tilde{\mathbf{x}}\|} \geq s_n(\mathbf{A}) \quad (3-34)$$

Therefore,

$$\text{cond } \mathbf{AD}^* = \frac{s_1(\mathbf{A}_1)}{s_r(\mathbf{A}_1)} \leq \frac{s_1(\mathbf{A})}{s_n(\mathbf{A})} = \text{cond } \mathbf{A} \quad (3-35)$$

Thus the conditioning of \mathbf{AD}^* can be no worse than that of \mathbf{A} [3.29].

This means that the non-negativity makes the inverse problem well-conditioned [3.31].

To make constraints non-negative, the measured sound pressure is squared, which means $\boldsymbol{\beta} \geq \mathbf{0}$. Finally, the optimization problem for a high-speed train was deduced as follows:

$$\text{Minimize } \|\varepsilon\| = \|\beta - Ts\|, \text{ subject to } s \geq 0 \quad (3-36)$$

The parameters β and s are known. Therefore, to solve the equation (3-36), convergence of source s is only considered as shown in Figure 3-2.

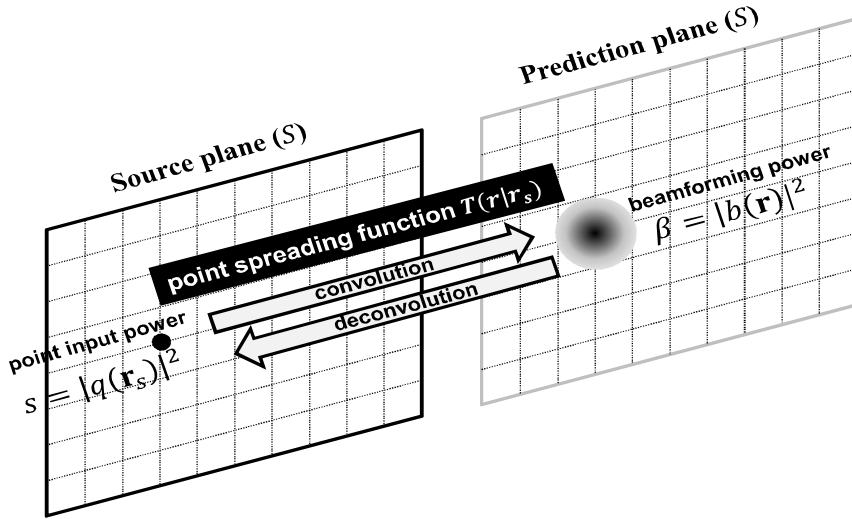


Figure 3-2 Concept of deconvolution with nonnegative variables and point spread function (Prediction plane = Source plane)

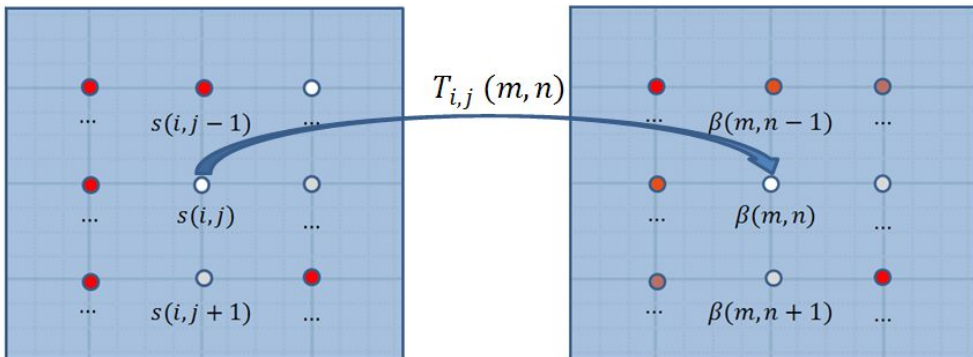


Figure 3-3 Sources and prediction planes

To obtain convergence of the source, iteration method was used to solve the problem. This method is described below.

At first, M by N plane in source and prediction planes are considered as shown in Figure 3-3. The point spread function, $T_{i,j}(m,n)$, is a connecting function from a source at the position (i, j) in the source plane to the beampower at the position (m, n) in the prediction plane.

$$\beta(m, n) = \sum_{i=1}^M \sum_{j=1}^N \beta_{i,j}(m, n), \text{ where } \beta_{i,j}(m, n) = s(i, j) T_{i,j}(m, n) \quad (3-37)$$

The value of the beampower at a position is summed over all possible values of the combinations of sources and point spread functions. Moreover, we can assume that the zero value of the beampower at a position means that there is no source. Therefore, we should consider the case where the value at a source is not zero.

The maximum value of a source is the beampower divided by the point spread function; therefore, we can derive the initial states of each source with equation (3-38). Then, the iteration is carried out as shown in equation (3-39) until the source value converges. The convergence condition of this equation is expressed in equation (3-40).

- Initial states

$$s^1(i, j) = \frac{\beta(n, m)}{T_{i, j}(n, m)} \quad (3-38)$$

- Iterations

$$s^k(i, j) = \frac{\beta(n, m)}{T_{i, j}(n, m)} - \frac{\left[\sum_{j'=1}^{j-1} s^{k-1}(i', j') T_{i', j'}(n, m) + \sum_{j'=j+1}^N s^{k-1}(i', j') T_{i', j'}(n, m) \right]}{T_{i, j}(n, m)} - \frac{\left[\sum_{i'=1}^{i-1} \sum_{j'=1}^N s^{k-1}(i', j') T_{i', j'}(n, m) + \sum_{i'=i+1}^M \sum_{j'=1}^N s^{k-1}(i', j') T_{i', j'}(n, m) \right]}{T_{i, j}(n, m)} \quad (3-39)$$

- Iteration condition

$$s^{k+1}(i, j) = \max(s^k(i, j), 0) \quad (3-40)$$

The new solution at each iteration should satisfy the non-negativity constraint. Therefore, the source strength is set to zero if it is negative.

Beamforming method and inverse problem optimization are summarized in

Figure 3-4.

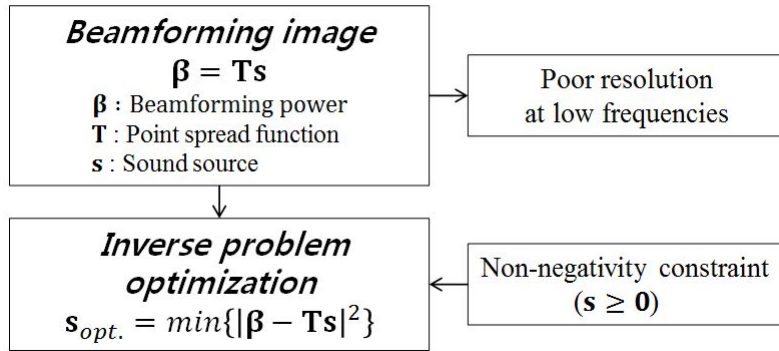


Figure 3-4. Beamforming method and inverse problem optimization

3.2 Algorithm development

In this section, the process of resolution improvement method and the algorithm development was presented. To improve resolution from the beamformer output in the prediction plane, it is important to derive point spread function. As previous mentioned, point spread function was spatial combination of weighting function and Green function. Moreover, the beamformer was generated from the point spread function and the point source. Therefore, we can derive point spread function from the noise map in the beamforming method. Then, iteration method is used to solve the inverse optimization problem. This process is summarized in Figure 3-5.

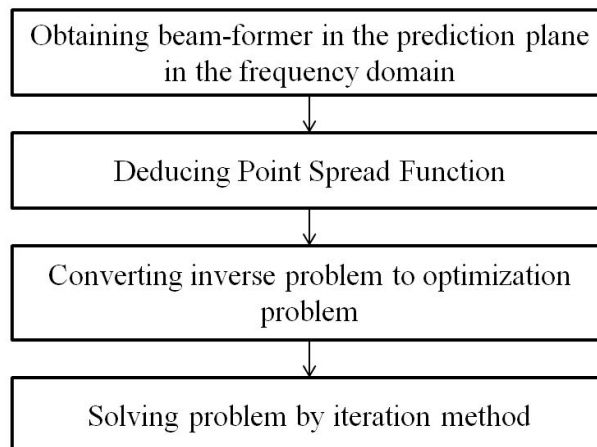


Figure 3-5. Resolution improvement process

In application of the inverse problem optimization, meaningful solution range for iteration method is made with regard. Because the rank of noise source matrix can approach one when using the iterative solution, there is no definitive limitation on the spacing or number of grid points or iteration to be used. Too fine of a distribution would require substantial solution iterative times and then only give more detail than is realistically feasible, or believable, from a beampattern which is too broad. On the other hand, too coarse of a distribution would render solution of source which would reveal less detail than needed, and also which may be aliased with resulting false images. Therefore, the solution range in the prediction should be determined for solving the inverse optimization problem.

3.3 Applications and discussions

After algorithm development, an application to high-speed trains was conducted. The high-speed train has low-frequency noise sources. For example, the pantograph and bogie sections in the high-speed train have multiple noise sources in the low frequency. The bogie sections also have multiple noise sources from the rolling noise and the turbulent noise flow in the lower frame as shown in Figure 3-6. The pantograph has rods and head which generate vortex shedding noises at the high speed and the cavity noise from the flow influx in the pantograph cover section as shown in Figure 3-7.

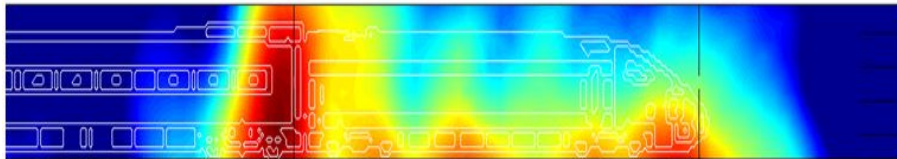


Figure 3-6 Low-frequency noise sources of leading power car (300 Hz)

(Relative level (dB): $-10 \leq$  ≤ 0)

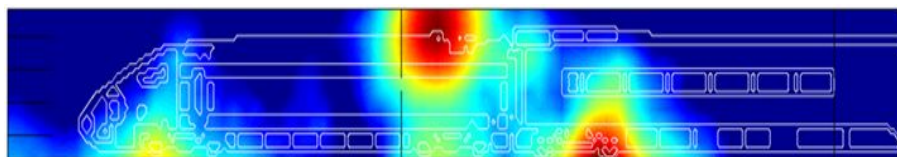


Figure 3-7 Low-frequency noise sources of trailing car (300 Hz)

(Relative level (dB): $-10 \leq$  ≤ 0)

Figure 3-8 shows beampower distribution of a high-speed train. Exact noise sources were not identified because of widely distributed images. However, we can predict the accurate source positions from the additional information of point spread function at a position in a prediction plane as shown in Figure 3-9. Point spread functions at various positions were presented in Figure 3-10.

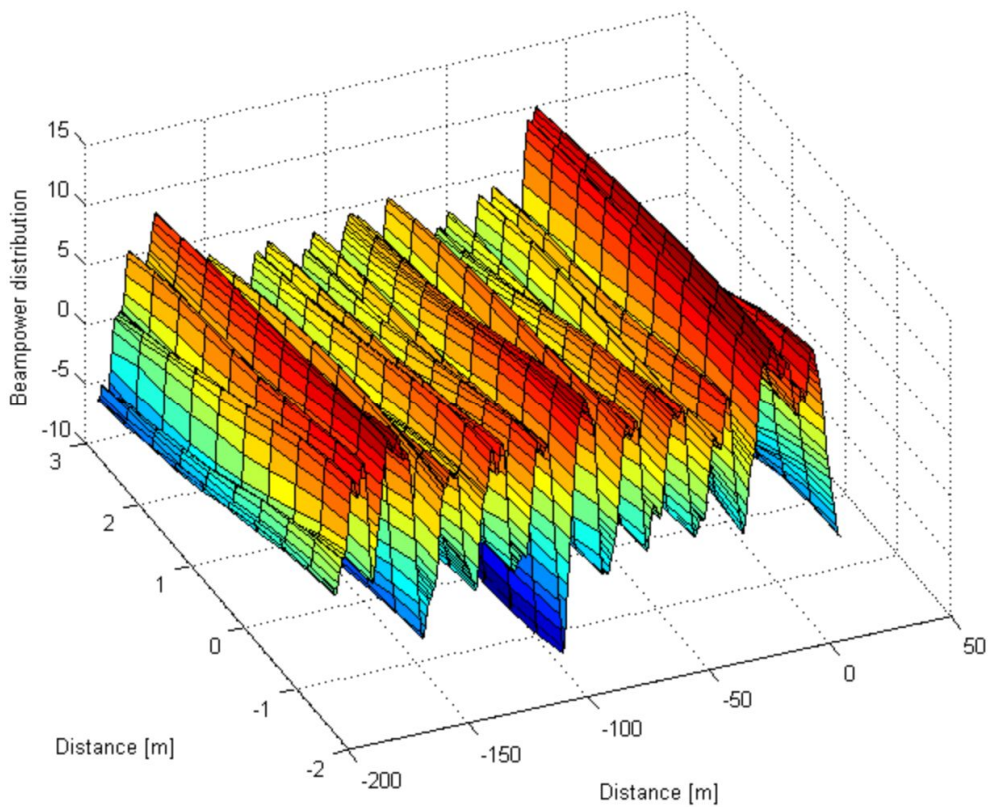


Figure 3-8 Beampower distribution of high-speed trains (300 Hz)

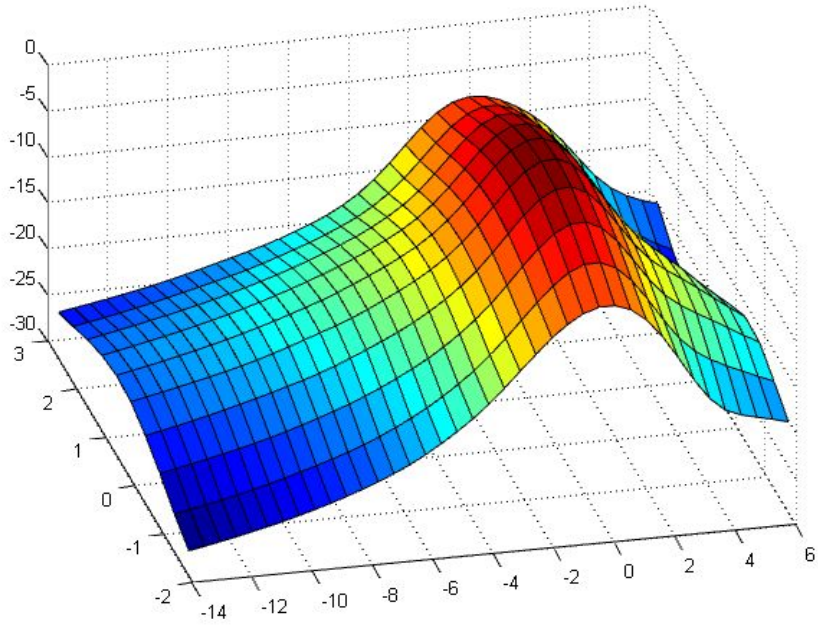
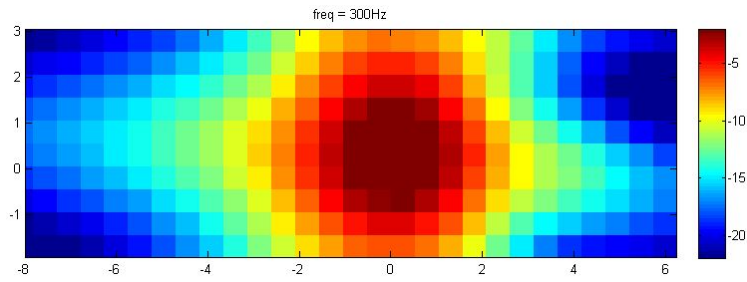
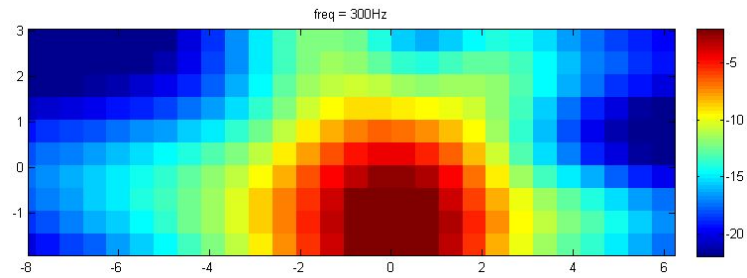


Figure 3-9 Distribution of point spread function (300 Hz)



(1) Center position



(2) Lower position

Figure 3-10 Point spread function at various positions

For applying optimization problem in the source plane, the beampower distribution in analysis region should be derived as shown in Figure 3-11. Then, iteration method using point spread function was applied. Figure 3-12 shows noise source position in initial states. By repeating iterations, improved source positions were obtained as shown in Figure 3-13.

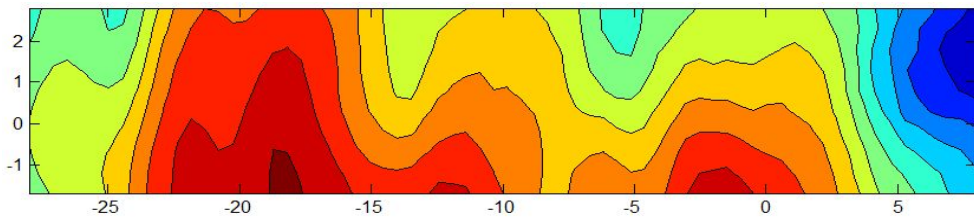


Figure 3-11 Beampower image contour of power car

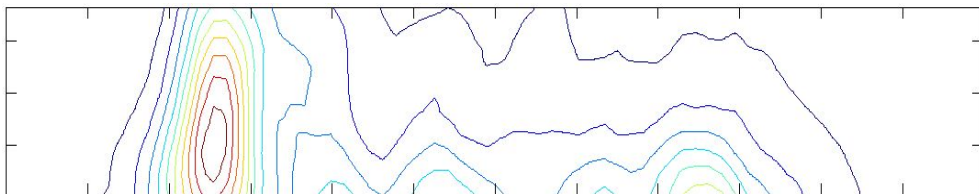


Figure 3-12 Iteration method at initial state

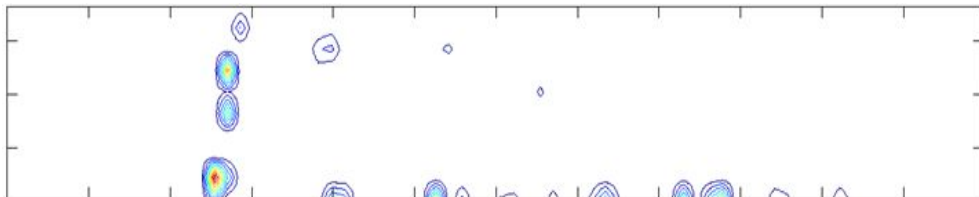


Figure 3-13 Iteration method at convergence state

In general, the number of iterations required to reach the convergence state increases at high frequencies, as shown in Figure 3-14. This means that many computations occur in the error range. In this study, 0.00001 was selected as a toleration coefficient. The narrow distribution of the point spread function and many noise sources at high frequencies are estimated to be a main reason for the increase in the number of iterations for convergence, as shown in Figure 3-15.

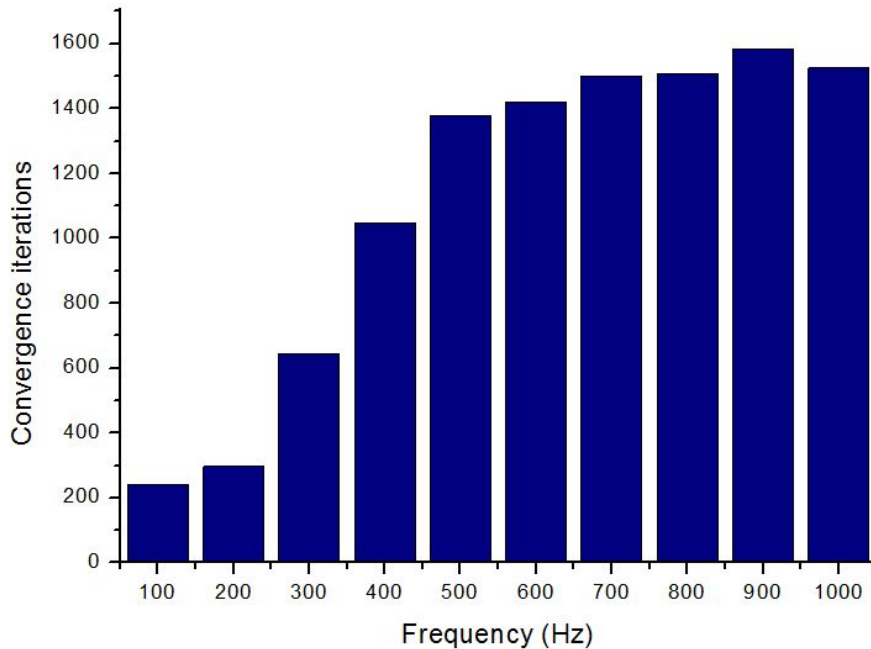
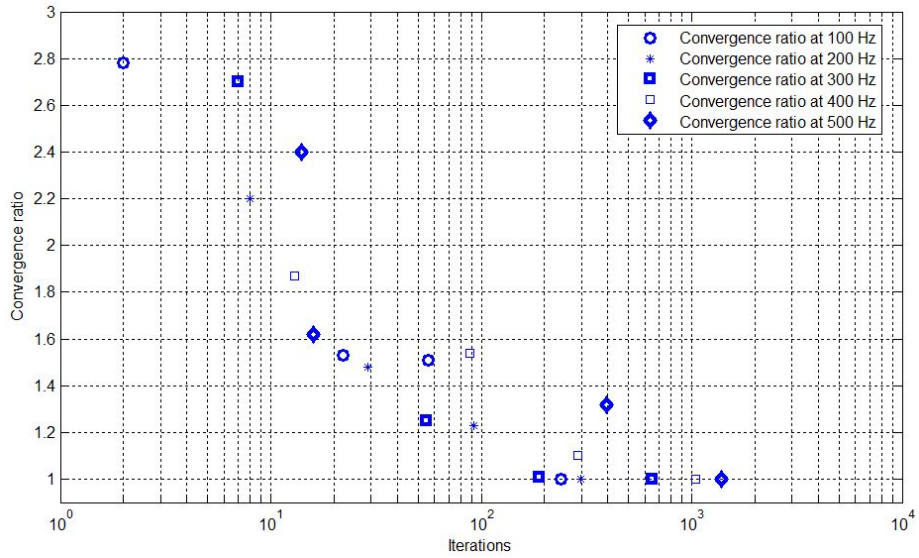
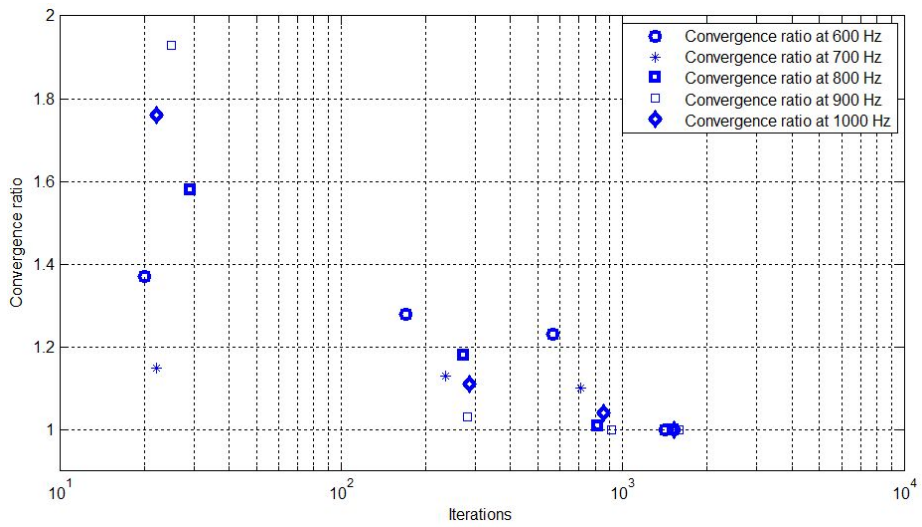


Figure 3-14 Number of iterations required for convergence at various frequencies



(1) Convergence ratio from 100 Hz to 500 Hz



(2) Convergence ratio from 600 Hz to 1000 Hz

Figure 3-15 Number of iterations for various frequencies

Noise maps obtained from the beamforming and the resolution improvement methods were compared in Figure 3-16. The results show that the noise map of the resolution improvement has higher resolution in the overall frequency. For example, the beamforming method does not provide detailed noise sources of the pantograph due to its multiple low frequency noise. However, the resolution improvement method shows that the pan head, upper and lower frames and mounts of the pantograph were specified sources positions. Moreover, the noise of the pan head was radiated until the frequency of 1000 Hz.

In addition, the rolling noise and the aerodynamic noise in the bogie area were not distinguished in the low frequency from the beamforming method. However, the resolution improvement method suggested that aerodynamic noise in the bogie was dominant noise source in the low frequency.

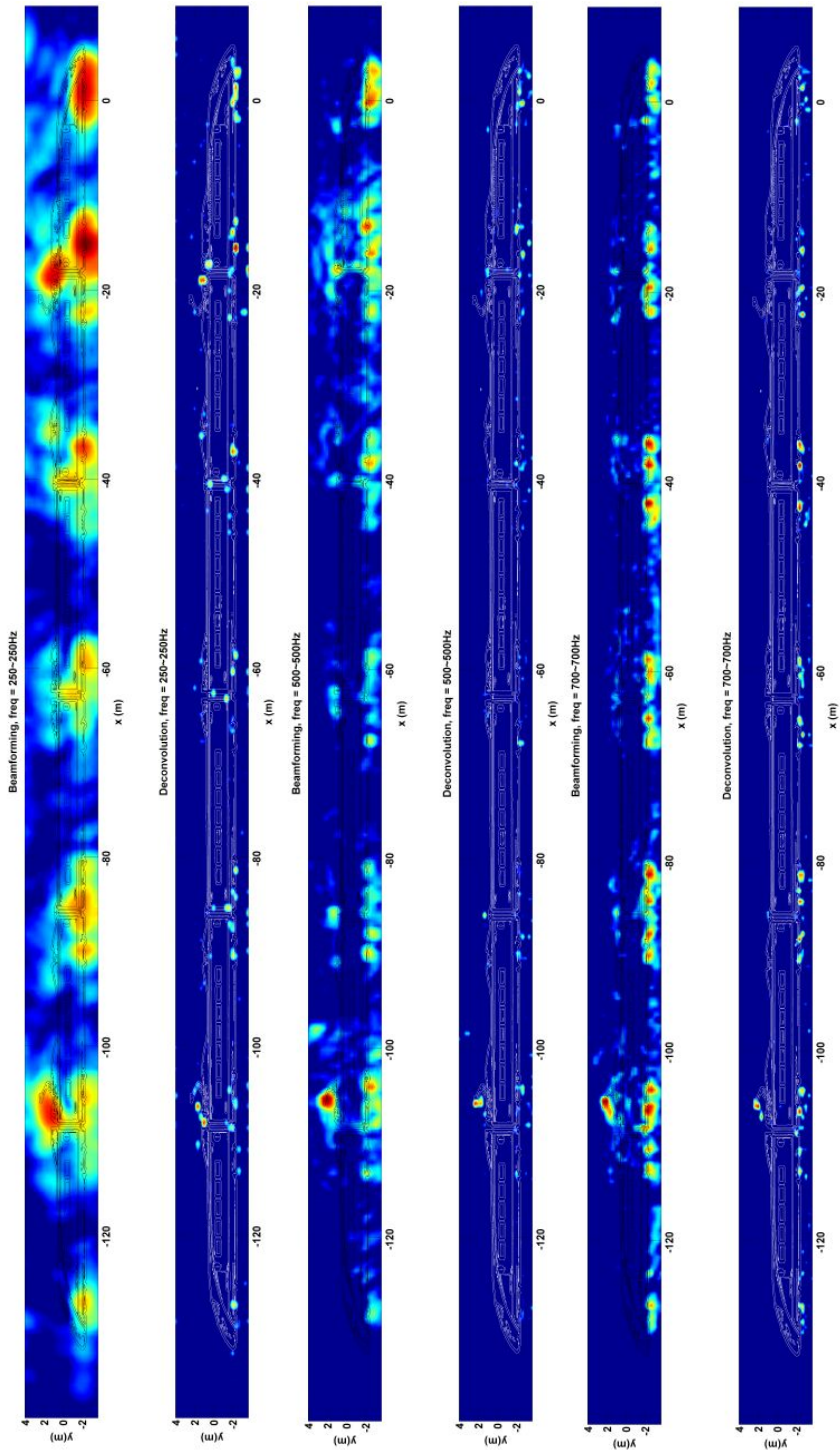


Figure 3-16 Comparison of noise maps obtained from beamforming and resolution improvement methods

(Relative level (dB): $-10 \leq$  ≤ 0)

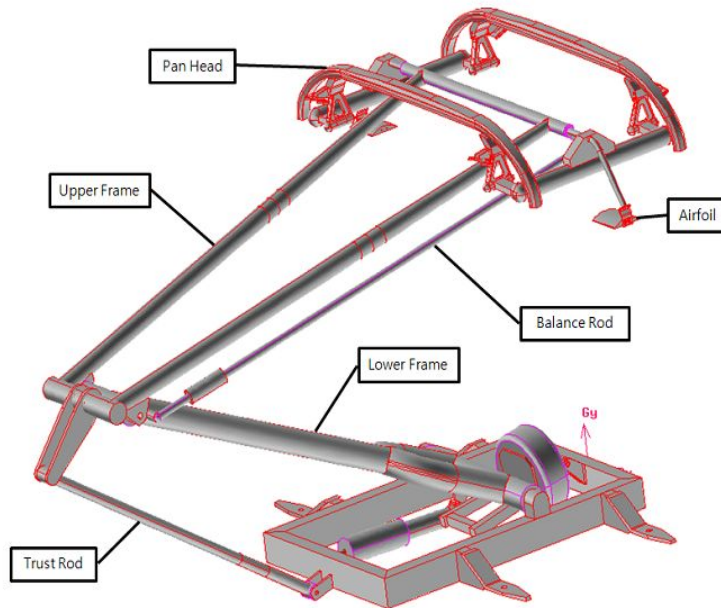


Figure 3-17 Pantograph configuration

The pantograph consists of structures such as the pan head, the upper and lower frames, the trust and balance rods, and the airfoils, as shown in Figure 3-17. The wind tunnel test results for noise source identification of the pantograph conducted by the Korea Aerospace Research Institute are shown in Figure 3-18. Without a resolution improvement technique, the detailed noise sources of the pantograph at the frequency of 1250 Hz were not obtained. At the high frequency of 3150 Hz, where the resolution was improved by the narrow main lobe in the beamforming method, the pan head was identified as the main noise source. This result was similar to the

enlarged image of the pantograph at the frequency of 700 Hz obtained from the resolution improvement method, as shown in Figure 3-19.

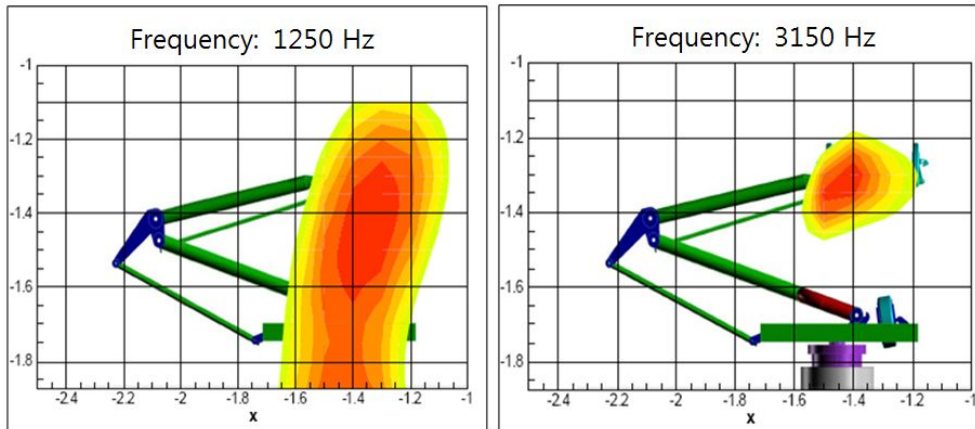


Figure 3-18 Wind tunnel test results

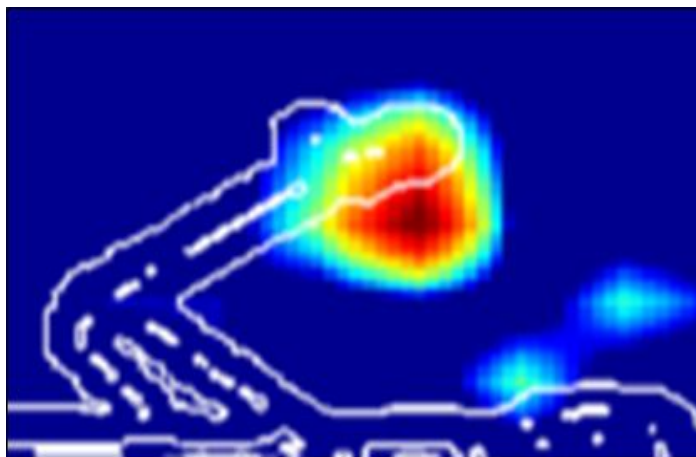
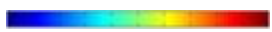


Figure 3-19 Improved resolution of pantograph (700 Hz)
(Relative level (dB): $-10 \leq$  ≤ 0)

The improved noise source positions of high-speed train were obtained and the results were summarized as shown in Table 3-1. From the research, the resolution improvement method in the low frequency was implemented. Especially, through the application to the high-speed train, the improved noise sources were identified.

Table 3-1 Improved source positions of pantograph and bogie

Position	Improved noise sources
Pantograph	Pan head
	Upper frame
	Lower frames
	Mount
Bogie	Under frame area
	Wheels

4. Characteristics deduction of main noise sources

It is important to derive the characteristics of the main noise sources in order to effectively reduce noise. For example, the noise sources in ship building are the propellers, the main equipment, the generation units, the air pressers or conditioners, the boiler, and the air blowers. When many noise sources are scattered, effective noise reduction measures can be established by deriving the characteristics of the main noise sources. In particular, we can infer the causes of the noise sources from identifying the main noise sources and deducing the characteristics of the noise sources of a high-speed vehicle, which provides effective noise reduction measures.

Rolling noise among various noises in the high-speed trains was conducted from wheel and rail contact model research. P.J.Remington built a theoretical model of the rolling noise from wheel and rail contact model [4.1, 4.2]. The fact that rolling noise was generated from the wheel and rail roughness was provided from the model. D.J.Thompson conducted simulation about sound radiation from the rolling noise and derived sound characteristics of rolling

noise [4.3-4.8]. The track wheel interaction noise software was developed from the research. In this circumstance, the theoretical model for the rolling noise is useful to derive the characteristics of the noise. However, not only roll noise but aerodynamic noise was generated in the bogie area so the theoretical model has a limitation which does not provide actual acoustic radiation from the bogie.

If the vehicle is travelling at high speed, the aerodynamic noise is a major noise source. The aerodynamic noise generated from the turbulent flow through the vehicle and increased greater than rolling noise to speed increase. Crespi *et al.* measured the boundary layer on-board the TGV high-speed train with LASER Doppler velocimetry [4.9]. N.Paradot *et al.* computed the flow around a high-speed train with a 1/5 scale model using wind tunnel experiments [4.10]. In the other hand, Lighthill conducted a research of aerodynamic noise generation from the flow [4.11]. In this research, estimating the sound radiated from a fluid flow with rigid boundaries based on the equations of motion of a gas was conducted. The sound field which would be

produced by a static distribution of acoustic quadrupoles was explained. Lighthill was stimulated by anticipation of large-scale commercial jet air travel to formulate his theory of jet noise. Curle made an extension of Lighthill's general theory of aerodynamic sound to incorporate the influence of solid boundaries upon the sound field [4.12]. J.E. Ffowcs Williams and D.L. Hawkings extended the Lighthill-Curle theory to include arbitrary convection motion [4.13]. The research laid the foundation for development of Computer fluid dynamics. However, the actual source is formed of a point source and grid sizes do not become infinite. Therefore, it is difficult to correctly implement aerodynamic noise of the high-speed train based on the computational fluid-dynamics simulations [4.14].

In order to overcome the limits of computational fluid-dynamics simulations, studies using a wind tunnel test were actively carried out. The wind tunnel test has benefits of the wind speed control and constant rate of flow for a long time for noise measurement [4.15]. C. Noger *et al.* investigated experimentally the aeroacoustic features of the pantograph recess in a low-

subsonic wind tunnel with a realistic 1/7 scale mock-up both with and without pantograph [4.16]. Rossiter conducted wind tunnel experiments on the flow over rectangular cavities at subsonic and transonic speeds [4.17]. It was suggested that the periodic component is owing to an acoustic resonance within the cavity excited by a feedback loop phenomenon. The feedback consists in the upstream propagation of pressure perturbations generated in the impingement region toward the region of maximum receptivity of the shear layer, as it separates from the upstream edge. Flow instabilities are then shed near the upstream edge. The amplification of the instabilities rapidly induces nonlinear vortices, which continue to grow due to fluid entrainment and viscous effects. During the impingement, new pressure perturbations are generated, which propagate toward the upstream direction, closing loop. The noise generated from the inter-coach spacing of the high-speed train was explained from this research [4.18]. However, wind tunnel test have limitations of missing data such as actual flow data and wheel-rail interaction of driving high-speed trains.

A sound visualization technique provides noise maps of the high-speed vehicle, which localizes noise sources. H. M. Noh *et al.* measured the noise of Korean high-speed trains at speeds ranging from 150 to 300 km/h with a microphone array [4.19]. From the analysis of the measurement data, the dominant noise sources were the front nose, pantograph, inter-coach spacing, and bogies. However, it is difficult to derive the frequency characteristics of the noise source from the sound-field visualization because the resolution of the sources is not constant over a prediction plane.

In this chapter, deduction of the characteristics of the main noise sources of a high-speed moving vehicle was presented on the basis of sound visualization technique. In section 4.1, weighting factors about the resolution changes as function of distances were derived from the array resolution analysis. In section 4.2, the noise characteristics of the main noise sources were derived from the application of the weighting factors and the frequency conversion of the measurement data. In section 4.3, the noise characteristics of the main noise sources of a high-speed train were discussed.

4.1 Array resolution analysis

Microphone array resolution changes depended on the positions between the noise sources and the measurement microphone. A microphone array system has a higher resolution when the noise source is in the center of the array plane. Thus, to derive the characteristics of the noise, it is necessary to use the measured signal from the high-resolution region. Therefore, in this section, array resolution analysis was conducted.

Time-domain analysis can be utilized for real-time identification of sound sources. The sound pressure signals received at the microphone array can be expressed as

$$\mathbf{p}(t) = [p_1(t), p_2(t), \dots, p_M(t)]^T \quad (4-1)$$

and the scan vector can be written as

$$\mathbf{w}(\theta, t) = [w_1(\theta, t), w_2(\theta, t), \dots, w_M(\theta, t)]^T \quad (4-2)$$

The time-domain representation of the beamformer output $b(\theta, t)$ in terms of $\mathbf{w}(\theta, t)$ can be derived from the inverse Fourier transform of the frequency-domain expression. The inverse Fourier transform of the frequency-

domain beamformer output gives

$$\begin{aligned}
 b(\theta, t) &= \int_{-\infty}^{\infty} [\mathbf{w}(\theta, \omega)^H \mathbf{p}(\omega)] e^{-i\omega t} d\omega \\
 &= \sum_{m=1}^M \int_{-\infty}^{\infty} [w_m(\theta, \omega)^* p_m(\omega)] e^{-i\omega t} d\omega \quad (4-3) \\
 &= \sum_{m=1}^M w_m(\theta, -t) *_t p_m(t)
 \end{aligned}$$

where the expression involving the time-domain convolution, denoted by $*_t$, is equivalent to a temporal correlation of two real-valued signals, which is defined as

$$f(-t) *_t g(t) = \int_{-\infty}^{\infty} f(\tau - t) g(\tau) d\tau = \int_{-\infty}^{\infty} f(\tau) g(\tau + t) d\tau \quad (4-4)$$

Consequently, the general description of the beamformer output is given by the sum of correlations:

$$b(\theta, t) = \sum_{m=1}^M \int_{-\infty}^{\infty} [w_m(\theta, \tau) p_m(t + \tau)] d\tau \quad (4-5)$$

The temporal correction of (4-3) can be regarded as a pressure signal $p_m(t)$ filtered by a time-reversed scan vector $w_m(\theta, -t)$ in the time domain.

In practice, the filter length of a scan vector is limited, and filtering is thus implemented by discrete-time signal processing. For a discrete time instance ($\tau = n\Delta t$), the integral of (4-5) can be rewritten as

$$b(\theta, t) = \sum_{m=1}^M \sum_{n=0}^{N-1} [w_m(\theta, n\Delta t) p_m(t + \tau)] d\tau \quad (4-6)$$

Therefore, one can consider the scan vector $w_m(\theta, n\Delta t)$ to be a finite impulse response (FIR) filter of length N .

To express (4-6) in matrix form, we define two partitioned vectors consisting of $\mathbf{w}(\tau)$ and $\mathbf{p}(t + \tau)$ at each time instance $\tau = n\Delta t$:

$$\hat{\mathbf{w}}(\theta) = \begin{bmatrix} \mathbf{w}(\theta, 0) \\ \mathbf{w}(\theta, \Delta t) \\ \vdots \\ \mathbf{w}(\theta, (N-1)\Delta t) \end{bmatrix}, \hat{\mathbf{p}}(t) = \begin{bmatrix} \mathbf{p}(t) \\ \mathbf{p}(t + \Delta t) \\ \vdots \\ \mathbf{p}(t + (N-1)\Delta t) \end{bmatrix} \quad (4-7)$$

Then, the beamformer output can be written as

$$b(\theta, t) = \hat{\mathbf{w}}(\theta)^T \hat{\mathbf{p}}(t) \quad (4-8)$$

and the corresponding beamforming power can be expressed as

$$\begin{aligned} \beta(\theta, t) &= E[|b(\theta, t)|^2] \\ &= \hat{\mathbf{w}}(\theta)^T E[\hat{\mathbf{p}}(t)\hat{\mathbf{p}}(t)^T] \mathbf{w}(\theta) \\ &= \hat{\mathbf{w}}(\theta)^T \hat{\mathbf{R}}(t) \mathbf{w}(\theta) \end{aligned} \quad (4-9)$$

The pressure vector $\hat{\mathbf{p}}(t)$ has a size of $MN \times 1$, and hence the correlation matrix defined in the time domain is given by

$$\widehat{\mathbf{R}}(t) = E \begin{bmatrix} \mathbf{p}(t)\mathbf{p}(t)^T & \cdots & \mathbf{p}(t)\mathbf{p}(t + (N-1)\Delta t)^T \\ \vdots & \ddots & \vdots \\ \mathbf{p}(t + (N-1)\Delta t)\mathbf{p}(t)^T & \cdots & \mathbf{p}(t + (N-1)\Delta t)\mathbf{p}(t + (N-1)\Delta t)^T \end{bmatrix} \quad (4-10)$$

If the measured pressure is a stationary random signal, then the expected value does not change with respect to time t . Accordingly, the time-invariant correlation matrix $\widehat{\mathbf{R}} = \widehat{\mathbf{R}}(t)$ can be derived as

$$\widehat{\mathbf{R}} = E \begin{bmatrix} \mathbf{A}_{pp}(0) & \cdots & \mathbf{A}_{pp}((N-1)\Delta t) \\ \vdots & \ddots & \vdots \\ \mathbf{A}_{pp}((N-1)\Delta t)^T & \cdots & \mathbf{A}_{pp}(0) \end{bmatrix} \quad (4-11)$$

where the auto-correlation matrix \mathbf{A}_{pp} is defined as

$$\mathbf{A}_{pp}(\tau) = E[\mathbf{p}(t)\mathbf{p}(t + \tau)^T] \quad (4-12)$$

Furthermore, if the measured pressure signal is ergodic, the temporal average can be an accurate estimator of the expected value. That is,

$$\mathbf{A}_{pp}(\tau) = \lim_{T \rightarrow \infty} \frac{1}{T} \int_0^T \mathbf{p}(t)\mathbf{p}(t + \tau)^T dt \quad (4-13)$$

where the variable T denotes the averaging period.

For the plane wave model, the inverse Fourier transform of the scan vector $w_m(\theta, t)$ is given by

$$\begin{aligned}
w_m(\theta, t) &= \frac{1}{M} \cdot \frac{1}{2\pi} \int_{-\infty}^{\infty} e^{-i\omega\Delta\tau(m-1)\sin\theta} e^{-i\omega t} d\omega \\
&= \frac{1}{M} \delta(t + \Delta\tau(m-1)\sin\theta)
\end{aligned} \tag{4-14}$$

which indicates that the measured signal $p_m(t)$ is filtered by a delta function with a certain time delay. The corresponding beamformer output reduced to

$$b(\theta, t) = \frac{1}{M} \sum_{m=1}^M p_m(t - \Delta\tau(m-1)\sin\theta) \tag{4-15}$$

shows that the scan vector shifts the array signal $p_m(t)$ with a time delay of $\Delta\tau(m-1)\sin\theta$. Therefore, all microphone signals are then in-phase, and hence the beamformer output is maximized.

In addition, if we use a frequency-invariant amplitude weighting a_m , then the scan vector will be

$$\begin{aligned}
w_m(\theta, t) &= \frac{1}{M} \cdot \frac{1}{2\pi} \int_{-\infty}^{\infty} a_m e^{-i\omega\Delta\tau(m-1)\sin\theta} e^{-i\omega t} d\omega \\
&= \frac{a_m}{M} \delta(t + \Delta\tau(m-1)\sin\theta)
\end{aligned} \tag{4-16}$$

and the corresponding beamformer output can be written as

$$b(\theta, t) = \frac{1}{M} \sum_{m=1}^M a_m^* p_m(t - \Delta\tau(m-1)\sin\theta) \tag{4-17}$$

In principal, the total beamforming power in the time domain is equivalent

to that in the frequency domain. This can be verified from Parseval's theorem:

$$\int_{-\infty}^{\infty} \beta(\theta, t) dt = \frac{1}{2\pi} \int_{-\infty}^{\infty} \beta(\theta, \omega) d\omega \quad (4-18)$$

If Parseval's theorem is applied to a signal of finite length T , then the equality can be written in terms of a Fourier series, which implies that the temporal mean of the beamforming power can be related to a discrete sum of the beamforming power in the frequency domain. That is,

$$\langle \beta(\theta, t) \rangle_t = \frac{1}{T} \int_{t_0}^{t_0+T} \beta(\theta, t) dt = \sum_{n=-\infty}^{\infty} \beta_n(\theta) \quad (4-19)$$

where $\langle \ \ \rangle_t$ indicates the temporal average, and $\beta_n(\theta)$ is the square of the Fourier series coefficient given by

$$\beta_n(\theta) = \left| \frac{1}{T} \int_{t_0}^{t_0+T} b(\theta, t) e^{i(\frac{2\pi n t}{T})} dt \right|^2 = \frac{1}{T} \beta(\theta, \omega = \frac{2\pi n}{T}) \quad (4-20)$$

For a signal $p_m(\omega)$ band-limited within $\omega \in [\omega_1, \omega_2]$, the summation of (4-19) can be further reduced to

$$\langle \beta(\theta, t) \rangle_t = \frac{2}{T} \sum_{n=n_l}^{n_h} \beta(\theta, \omega_n = \frac{2\pi n}{T}) \quad \text{with } \omega_l = \frac{2\pi n_l}{T} \text{ and } \omega_h = \frac{2\pi n_h}{T} \quad (4-21)$$

Note that the right-hand side of (4-21) is doubled to express the one-sided spectrum including the negative frequency components. Equation (4-21)

implies that the mean of the beamforming power in the domain is equivalent to the finite sum of the beamforming power at discrete frequencies.

From the summation rule of (4-21), we can see that the correlation matrix in the frequency domain can be calculated as

$$\begin{aligned}\sum_{n=n_1}^{n_h} \beta(\theta, \omega_n) &= \sum_{n=n_1}^{n_h} \{\mathbf{w}(\theta, \omega_n)^H \mathbf{E}[\mathbf{p}(\omega_n)\mathbf{p}(\omega_n)^H] \mathbf{w}(\theta, \omega_n)\} \\ &= \left[\sum_{n=n_1}^{n_h} \mathbf{w}(\theta, \omega_n)^H \mathbf{R}(\omega_n) \mathbf{w}(\theta, \omega_n) \right]\end{aligned}\quad (4-22)$$

However, designing the scan vector for every frequency of interest would require significant computational effort. If the frequency bandwidth is narrow enough, then one can design a representative scan vector for all the frequency components in the finite band. That is,

$$\begin{aligned}\sum_{n=n_1}^{n_h} \beta(\theta, \omega_n) &\approx \mathbf{w}(\theta, \omega_c)^H \left[\sum_{n=n_1}^{n_h} \mathbf{R}(\omega_n) \right] \mathbf{w}(\theta, \omega_c)^H \\ &\approx \mathbf{w}(\theta, \omega_c)^H \mathbf{R}(\omega_c) \mathbf{w}(\theta, \omega_c)^H\end{aligned}\quad (4-23)$$

where ω_c denotes an arbitrary reference frequency within the band. The correlation matrix of a narrowband signal can be considered as a superposition of matrices defined at multiple frequencies. The overall process to deal with the narrowband signal is hence similar to the single frequency case.

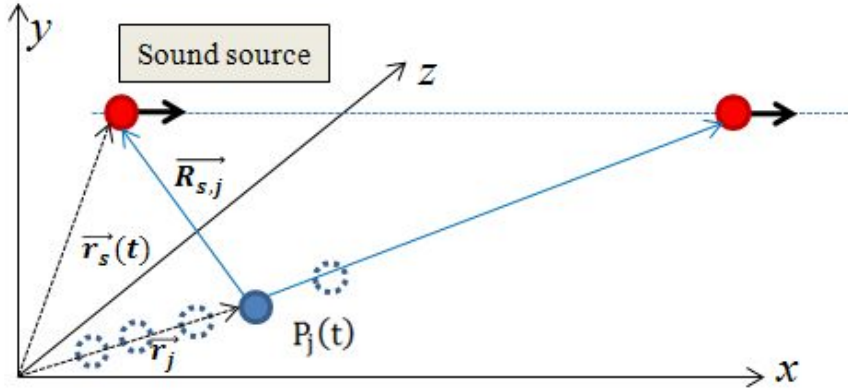


Figure 4-1 Microphone array measurement of signal from source

It is important to identify exact positions of a moving source in order to obtain the frequency characteristics of the source by using a microphone array as shown in Figure 4-1. We assumed that the microphone array is placed in a horizontal line from the rail and the high-speed train is driving on the track. The specific position in the high-speed train can be expressed as follows:

$$R_i(t) = (x_i + ut, y_i, z_i) \quad (4-24)$$

where u is the constant speed of the vehicle and (x_i, y_i, z_i) is the initial position of the specific position.

The distance (R_{ij}) from the position of the sound source and the j th microphone (x_j, y_j, z_j) can be expressed as follows:

$$R_{ij}^2(t) = \{(x_i + ut) - x_j\}^2 + \{y_i - y_j\}^2 + \{z_i - z_j\}^2 \quad (4-25)$$

The measured signal ($P_j(t)$) of the j th microphone is

$$P_j(t) = \frac{1}{R_{ij}(t)} S\left(t - \frac{R_{ij}(t)}{c}\right) \quad (4-26)$$

where c is propagation speed of sound.

Moreover, the resolution ability of the array decreases according to the distance between the source and the array, as shown in Figure 4-2. In order to compensate these decreases in resolution, weighing factors should be applied to the measured signal.

From the above equation, the beamforming output ($z_i(t)$) is the sum of the measured signals at all the microphones, as follows:

$$Z_i(t, x) = \frac{1}{M} \sum_{j=1}^M w(x) P\left(t + \frac{R_{ij}(t)}{c}\right) \quad (4-27)$$

The beampower spectrum can be calculated from the beampower by the Fourier transform.

$$Z_i(f) = \int_0^{+\infty} Z_i(t) e^{-i2\pi ft} dt \quad (4-28)$$

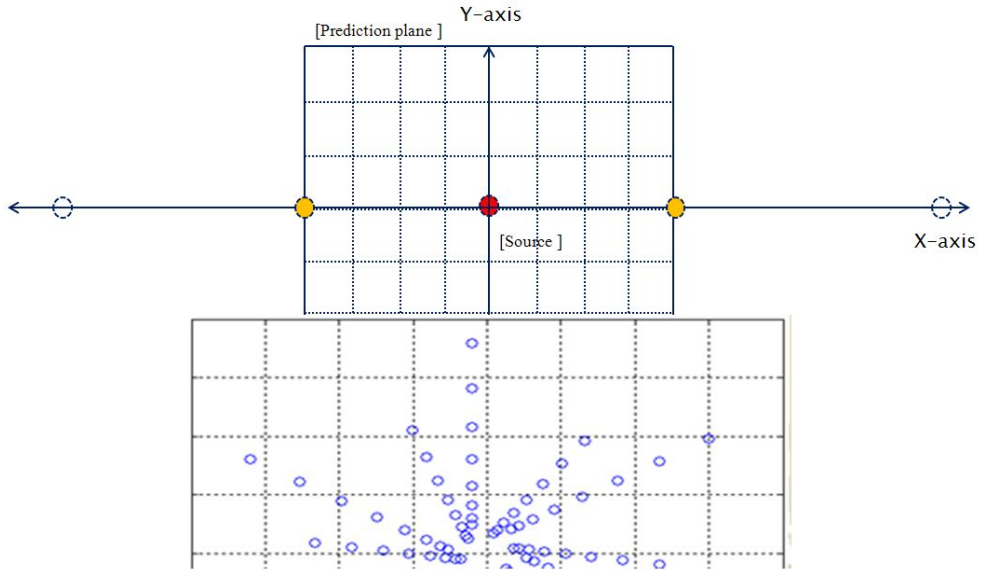


Figure 4-2 Array and prediction planes

The resolution of a beamformer describes its ability to distinguish waves incident from directions close to each other. When focusing on sources in the far field, resolution is the smallest angular separation between two plane waves that allows them to be separated, and for sources at a finite distance a practical definition of resolution is the minimum distance between two sources such that they can be separated [4.20].

Consider two plane waves with wave number vectors \mathbf{k}_1 and \mathbf{k}_2 , $|\mathbf{k}_1| = |\mathbf{k}_2| = k$, incident on a beamformer array with array pattern W as shown in Figure 4-3. Assuming unity amplitude for both plane waves, the

beamformer output is a superposition of the form:

$$B(\mathbf{k}, \omega) = W(\mathbf{k} - \mathbf{k}_1) + W(\mathbf{k} - \mathbf{k}_2) \quad (4-29)$$

The two incident plane waves of equal amplitude with wave number vectors can be resolved only if the projections $\hat{\mathbf{k}}_1$ and $\hat{\mathbf{k}}_2$ of \mathbf{k}_1 and \mathbf{k}_2 on the array plane are not within $R_K = K_{min}^0$ from each other. Here, R_K is the main-lobe width in the array pattern $W(\mathbf{K})$, and K_{min}^0 is the position of the first minimum of the array pattern.

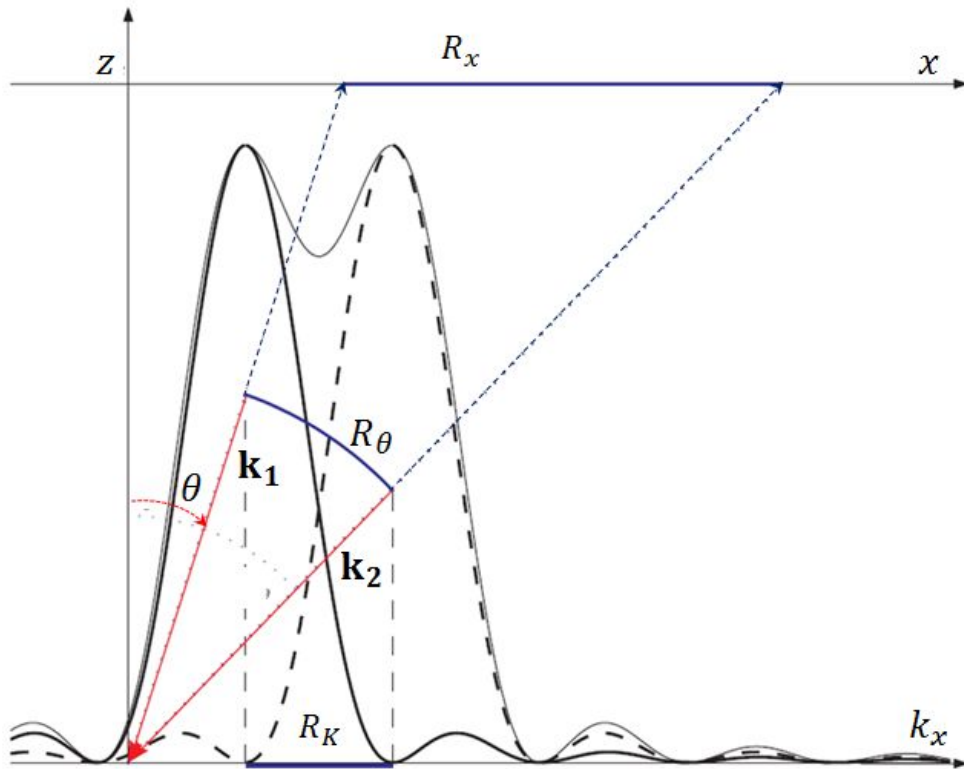


Figure 4-3 Resolution in off-axis

We have

$$|\hat{\mathbf{k}}_2 - \hat{\mathbf{k}}_1| = R_K \quad (4-30)$$

so the two plane waves are just exactly resolvable.

In the focus plane, we shall look only at the resolution in the radial direction, that is, in the direction away from the array axis. We choose to look at the resolution along the x -axis. The plane wave with wave number vector \mathbf{k}_1 is incident at an angle θ from the array axis, and the exactly resolvable plane wave with wave number vector \mathbf{k}_2 is incident at the angle $\theta + R_\theta$ from the axis, R_θ being the angular resolution in the radial direction. These two directions span the resolution R along the x -axis at the distance z from the array plane on the focus plane.

In the derivation we will now assume a very fine resolution, meaning that we can consider the resolutions in K , θ and x to be differential: $dR_K = dk_x$, $dR_\theta = d\theta$ and $dR_x = dx$. From $k_x = k \sin\theta$ we get $dk_x = k \cos\theta d\theta$ and therefore:

$$d\theta = \frac{dk_x}{k \cos\theta} \quad (4-31)$$

From the relation of $x = z \tan \theta$, we get:

$$dx = \frac{z d\theta}{\cos^2\theta} \quad (4-32)$$

and combination of the two above relations leads to:

$$dx = \frac{z dk_x}{k} \frac{1}{\cos^3\theta} \quad (4-33)$$

Finally, we replace the differential resolutions with the real finite resolutions and get:

$$R_x = \frac{z R_K}{k} \frac{1}{\cos^3\theta} \quad (4-34)$$

where R_K is the main lobe width in the array pattern and θ is the off-axis angle. The value of R_K is according to the Rayleigh criterion, given by the first null (minimum), K_{min}^0 , of the array pattern: $R_K = K_{min}^0$. The exact value depends on the positions of all microphones but a good general estimate can be calculated by considering the limiting case where we have an infinite number of transducers uniformly distributed over a line segment of length D or a circular disc with radius $D/2$. In the other words, we imagine we are able to sample the sound field at all points within the area (aperture) instead of only at a few discrete positions. In this continuous case we should use an integral

expression for the array pattern, the aperture smoothing function:

$$W(K) = \frac{1}{(2\pi)^d} \int_{|r| < D/2} w(\mathbf{r}) e^{j\mathbf{K}\cdot\mathbf{r}} d\mathbf{r} \quad (4-35)$$

Where $d=1$ for the line segment, $d=2$ for the circular aperture and $w(\mathbf{r})$ is now a continuous shading function. In this case of uniform shading, J_1 being the Bessel function of order 1:

$$W(K_x) = \frac{\sin(\frac{K_x D}{2})}{K_x/2}, d = 1 \quad (4-36)$$

$$W(K) = \frac{\pi D}{K} J_1\left(\frac{KD}{2}\right), K = \sqrt{K_x^2 + K_y^2}, d = 2 \quad (4-37)$$

Then, we define that the first zero in the array pattern corresponding to the line segment and the circular aperture occurs at:

$$K_{min}^0 = \alpha \frac{2\pi}{D} \quad (4-38)$$

where $\alpha = 1$ for the linear aperture and $\alpha \approx 1.22$ for the circular aperture.

Now, using the fact that the wave number k is related to the wavelength by

$k = 2\pi/\lambda$, we obtain the desired expression for beamformer resolution:

$$R(\theta) = \frac{\alpha}{\cos^3\theta} \frac{z}{D} \lambda \quad (4-39)$$

For on-axis incidence, $\theta = 0$, the resolution is given by:

$$R_{Axis} = \alpha \left(\frac{z}{D}\right) \lambda \quad (4-40)$$

The resolution is proportional to the wavelength and becomes better with larger aperture size, but worse with increasing array to object distance. This relation is not limited to acoustics.

Comparing the on-axis and general off-axis resolution, we notice that the ratio between them is given by:

$$\frac{R(\theta)}{R_{Axis}} = \cos^3 \theta \quad (4-41)$$

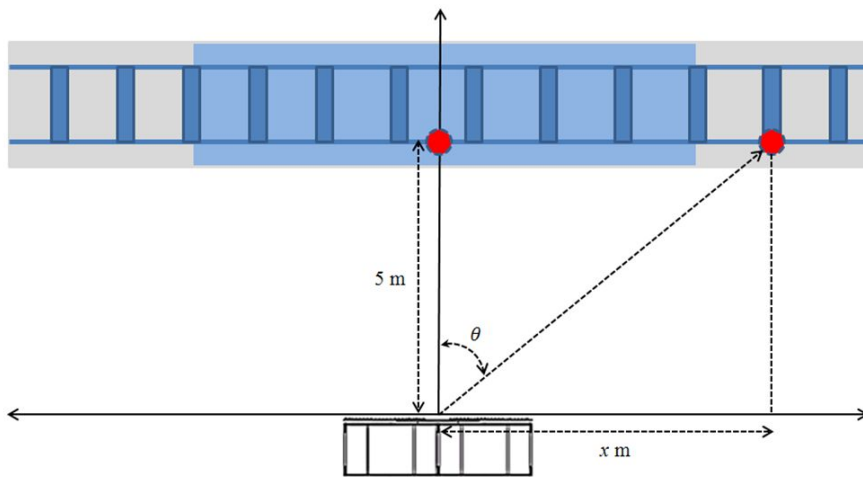


Figure 4-4 Measurement of passing-by noise

From measurement setup as shown in Figure 4-4, weighting factors can be derived as follows:

$$w(x) = \cos^3 \theta, \text{ where } \theta = \tan^{-1} \left(\frac{x}{5} \right) \quad (4-42)$$

A microphone array system has a higher resolution when the noise source is

in the center of the array plane as shown in Figure 4-5. The actual resolution of the microphone array was investigated through the array response function.

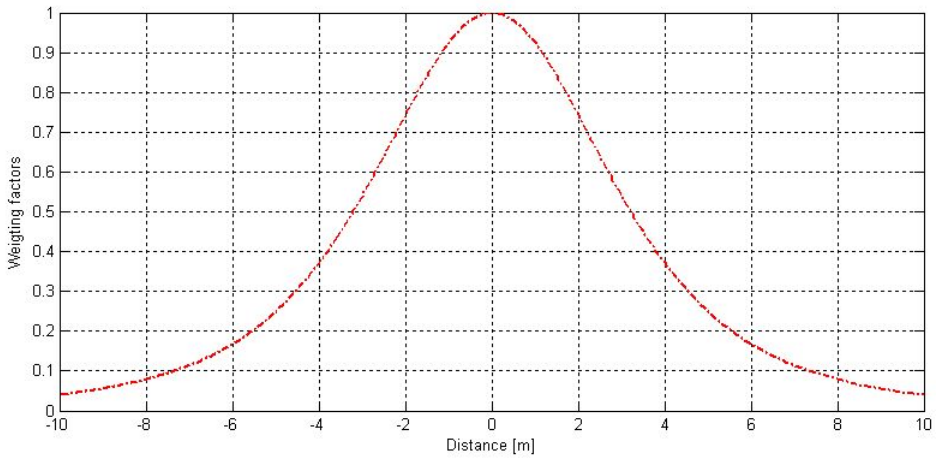


Figure 4-5 Weighting factors over distances

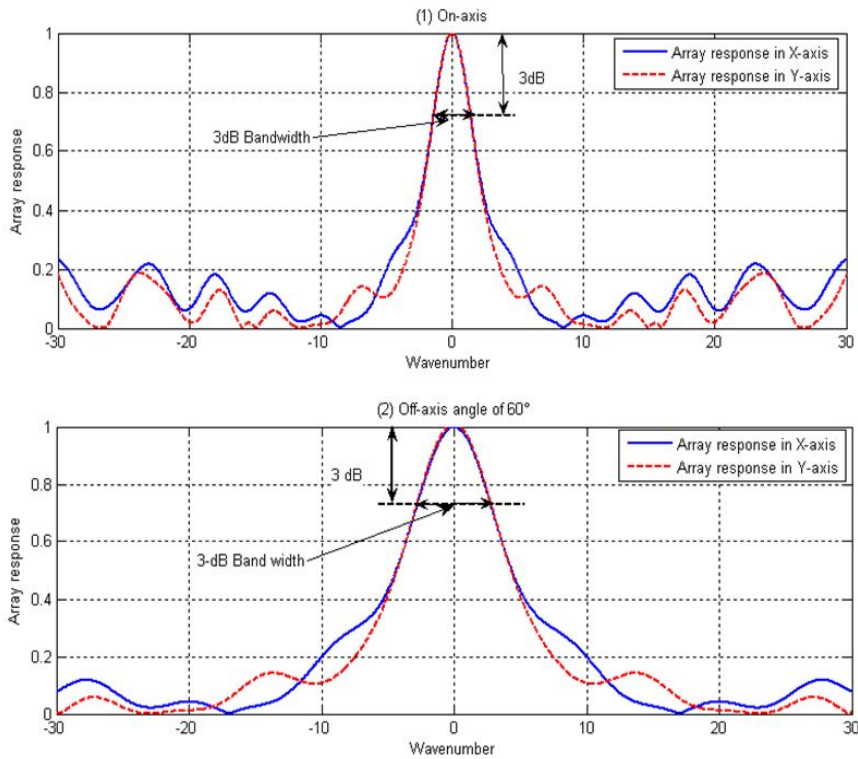


Figure 4-6 Array response function of 96-channel microphone array

We assume that the microphone array is placed in the horizontal plane (or X-Y plane) and the array response function is independent of the Z-axis. Moreover, the array response function has the maximum value of 1 at the origin of the X-Y plane as shown in Figure 4-6. Thus, to derive the characteristics of the noise, it is necessary to use the measured signal from the high-resolution region as shown in Figure 4-7.

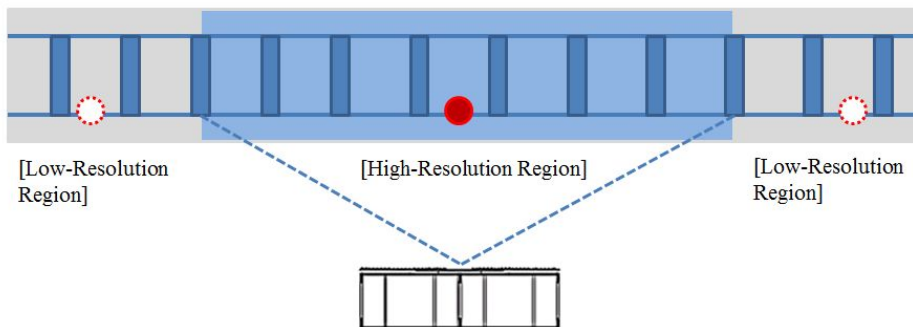


Figure 4-7 Microphone array resolution regions

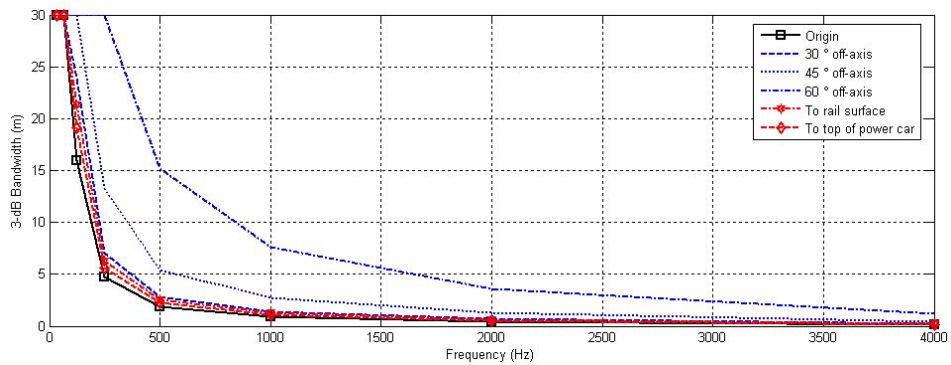


Figure 4-8 3 dB bandwidth of degrees off-axis from 0° to 60°

To investigate the high-resolution region of the designed microphone array in this study, an off-axis resolution analysis was conducted. From the resolution results at 30°, 45°, and 60°, the resolution decreased when the source was placed in an off-axis position. In particular, after 45°, the resolution fell drastically as shown in Figure 4-8.

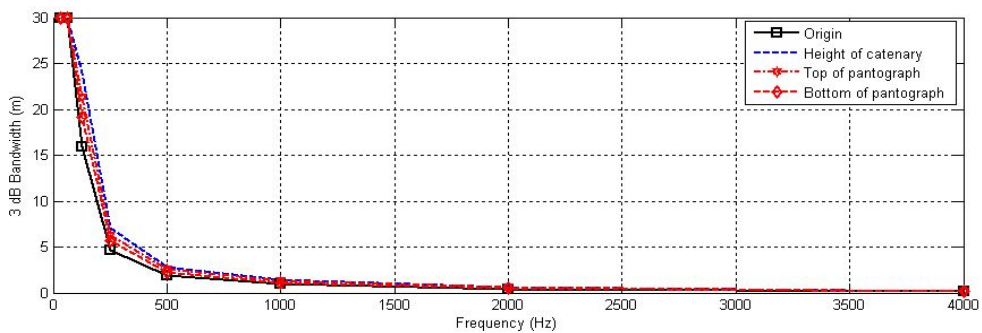


Figure 4-9 3 dB bandwidth of degrees off-axis from bottom to top

This trend was shown in the 3 dB bandwidth of degrees off-axis from bottom to top analysis. The maximum height of the high-speed train is 4.1 m and the height of the array center is 2.3 m. Therefore, the measurement range of the microphone array was +1.8 ~ -2.3 m from the array center. The resolution analysis results of both ends of the measurement range are shown. The resolution from the top of the power car to the rail surface was in the reliable region, which had better resolution by comparing to that of the 30°

angle as shown in Figure 4-9. To use the measurement data from the high-resolution region, weighting factors with high values in the high-resolution region and low values in the low-resolution region were derived.

4.2 Characteristics deduction algorithm

In this research, all noise sources are assumed monopole sources. The assumption was investigated with simulation tests about various sound radiation patterns. The sound radiation patterns can be divided into a monopole, a dipole and a quadrupole. A monopole is radiating sound waves that are only a function of the radial distance from the source such as small electric motors or pumps. A dipoles means composition of two monopoles in close proximity to each other of equal strength and oscillated 180 degree out of phase with each other and many sound sources including aerodynamic dipole sources can be models as point dipoles. A quadrupole consists of alternating positive and negative monopoles arranged on the corners of a square or a line. Directivity patterns of a dipole and a quadrupole are shown in Figure 4-10.

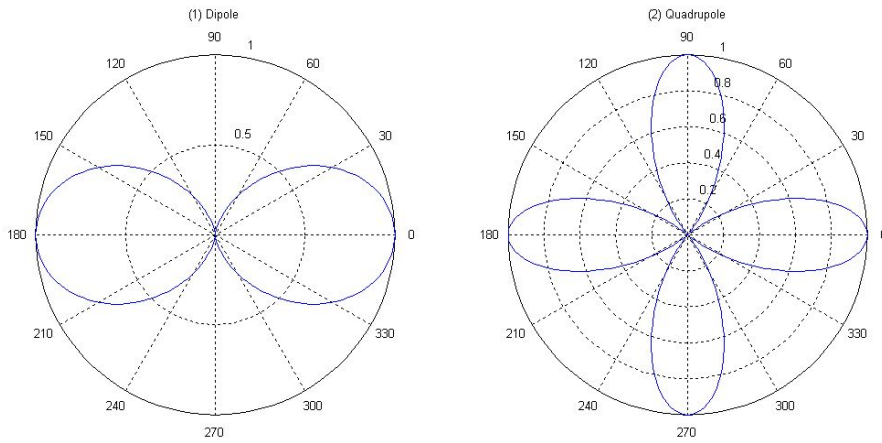


Figure 4-10 Directivity patterns of dipole and quadrupole

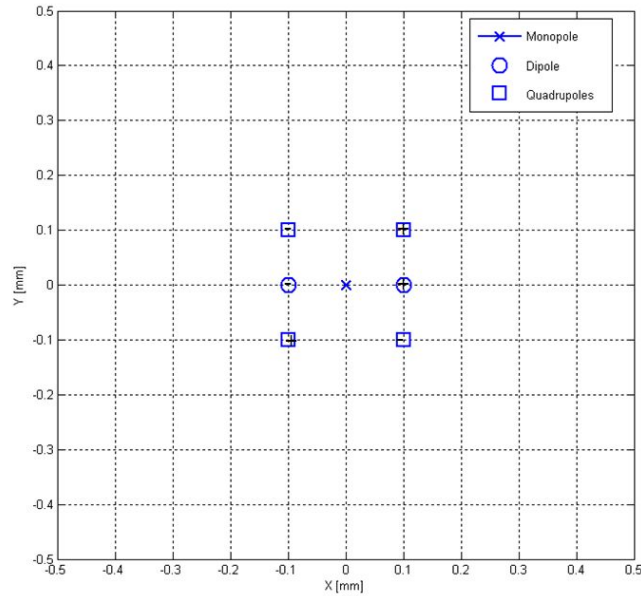


Figure 4-11 Source positions for simulations

The impacts on the microphone array depending on the source type were investigated from simulations. We assumed that sources of a monopole, a dipole, and a quadrupole radiated at the distance of 5 m from the center of the array as shown in Figure 4-11.

When the sound source emits a wave with a frequency of 2000 Hz, the 3-dB bandwidth of the monopole was the largest, as shown in Figure 4-12. In the case of the dipole source, it was confirmed that the bandwidth was reduced by approximately 0.1 m compared to the monopole, as shown in Figure 4-13. The quadrupole had the least amount of bandwidth, and its size was approximately 0.2 m lower compared to that of the monopole, as shown in Figure 4-14. This means that assuming a monopole source in the beamforming method may cause an error of approximately 0.2 m in the case of an actual quadrupole. Therefore, the weighting functions should be applied to the array response function for identifying the location of the actual sound source.

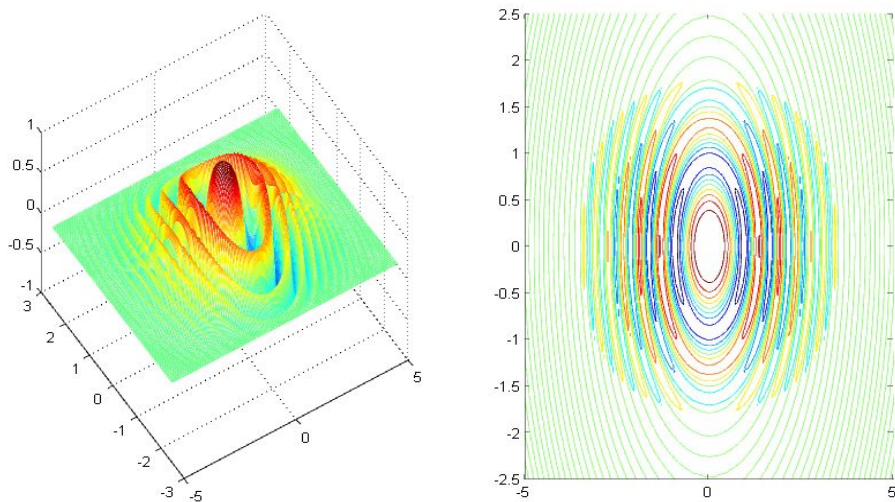


Figure 4-12 96-channel microphone array response of monopole source at frequency of 2000 Hz

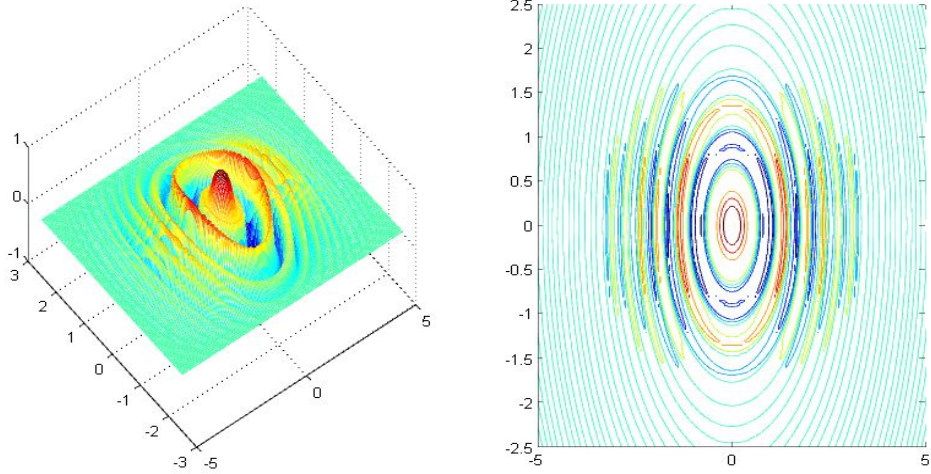


Figure 4-13 96-channel microphone array response of dipole source at frequency of 2000 Hz

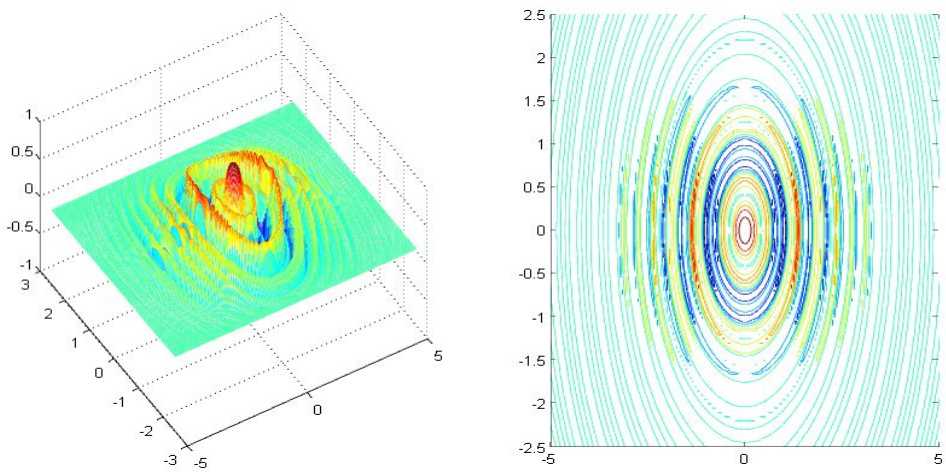
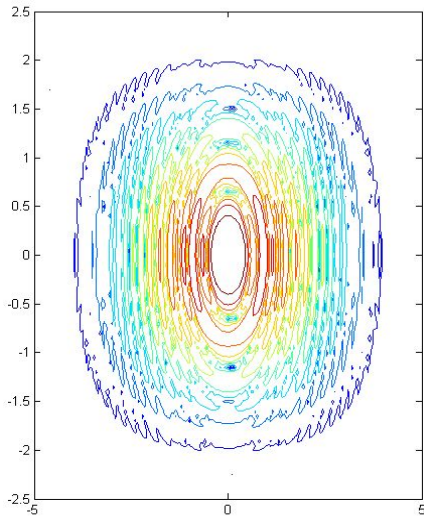
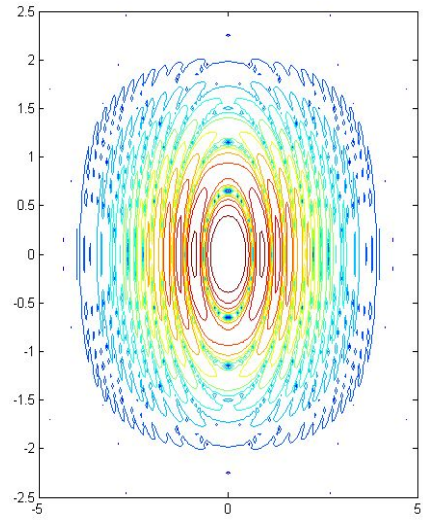


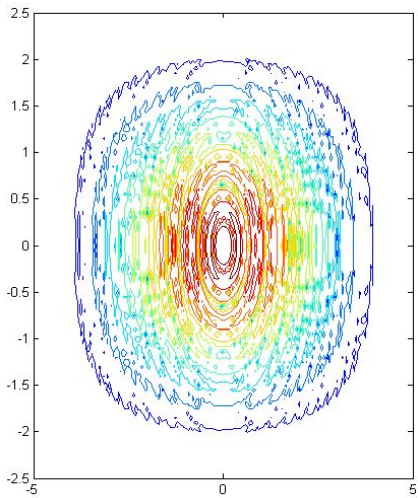
Figure 4-14 96-channel microphone array response of quadrupole source at frequency of 2000 Hz



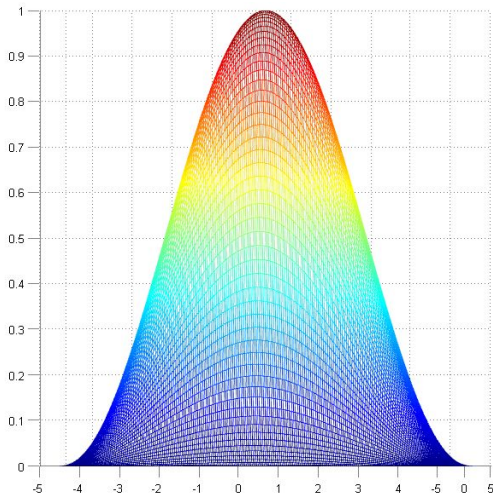
(1) Monopole



(2) Dipole



(3) Quadrupole



(4) Weighting factors

Figure 4-15 Array responses of sound source types

The radiation patterns with the applied weighting function for each array response function was investigated, as shown in Figure 4-15. The results show that the errors of the array response functions for the different source types decreased when applying the weighting function. From the simulation analysis,

the array response functions with applied weighing functions do not have significant differences for the 96-channel microphone array. Further, it was difficult to identify the source types for the high-speed vehicle; therefore, we assume that all noise sources were incoherently monopoles.

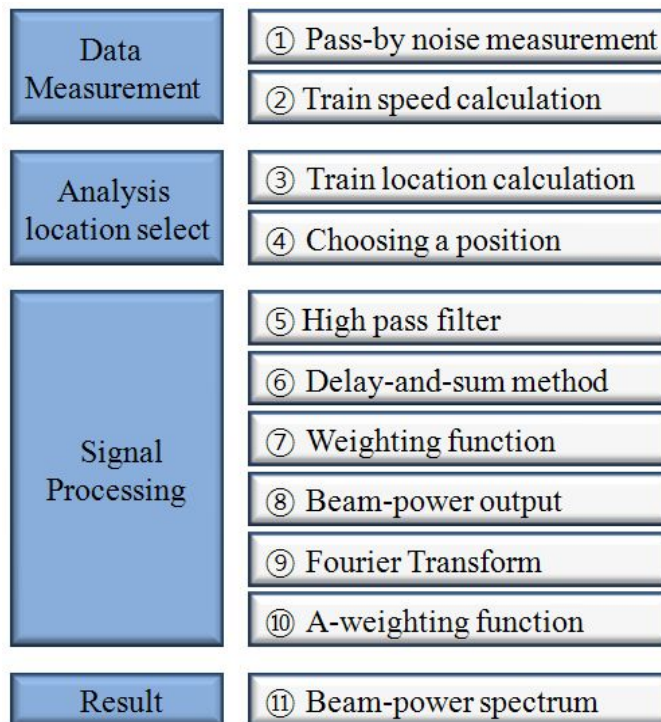


Figure 4-16 Workflow of obtaining beampower spectrum

Obtaining the beampower spectrum of the selected location could be divided into data measurement, position selection, signal processing, and results as shown in Figure 4-16.

4.3 Applications and discussions

In order to identify the characteristics of the sound source in a specific location, the vehicle pass-by noise was measured with a microphone array. A microphone was used to measure with 96-channel microphones. The overall array configuration is radial and irregular. The diameter of the array is 3.592 m, and the microphones are spaced at intervals of 0.03575 ~ 3.592 m. Moreover, nested arrays with radii of 1.75 m and 1 m and containing eight microphones each are arranged at 20° and 40° angles, respectively. Via these nested arrays, which enclose a number of measurement cables, the installation time could be considerably reduced. The 96-channel microphone array was placed at a horizontal distance of 5 m from the outside rail. The height of the center of the array was 2.3 m from the upper surface of the rail. Data measurement and analysis were conducted using PXI devices (DAQ board: PXIe-1065, controller: PXIe-8133, data steaming: NI 8260) from National Instruments.

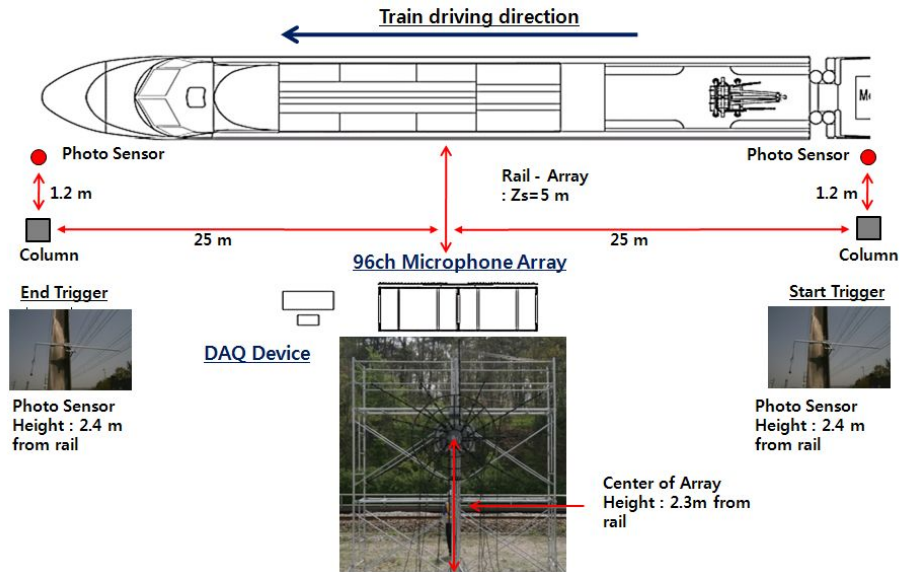


Figure 4-17 Microphone array measurement setup

In order to obtain the exact location of the sound source, it is important to identify the position and the velocity of the moving source over the time. Therefore, photoelectric sensors to measure the speed of a high-speed train were installed on two pillars of the rail. The speed was determined by calculating the pass-by time and the distance between these two pillars. The overall configuration of the measurement equipment is shown in Figure 4-17.

The main noise sources are the front nose, pantograph, inter-coach spacing and bogie areas. The noise in the front nose are generated due to the turbulence flow when the vehicle driving at the high speed. The aerodynamic noise from

the pantograph was generated by vortex shedding sound, whereas that from its cover occurred because of unsteady airflows and the pantograph cover generated noise due to turbulence flow. The noise of the inter-coach spacing was generated from the influence of cavities and mudflaps. The inflow of air into the cavity was the main noise generation mechanism. The rolling noise from the wheels and aerodynamic noise from scattering were generated in a bogie area. Therefore, in this section, the aerodynamic noise position was selected as shown in Figure 4-18. The location of main noise sources were selected based on results about noise source identification of the high-speed train.

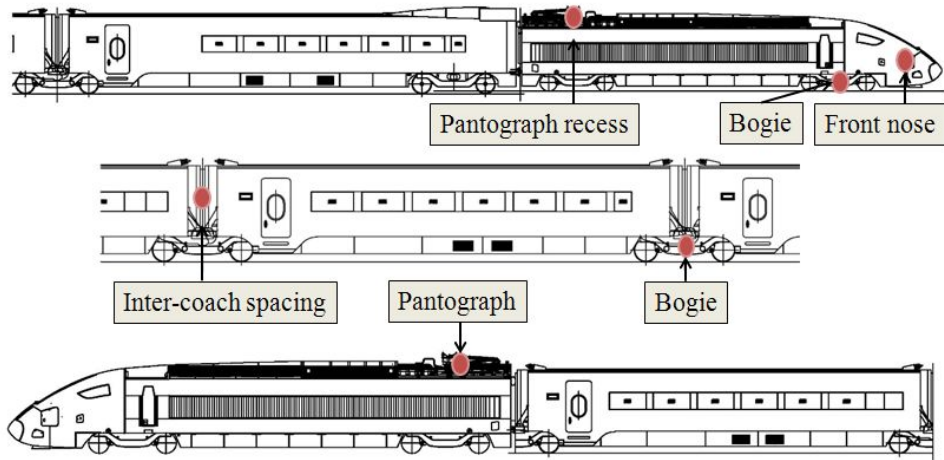


Figure 4-18 Aerodynamic noise positions of high-speed trains

Obtaining the beampower spectrum of the selected location could be divided into data measurement, position selection, signal processing. First, it was important to measure the noise and speed of the high-speed trains as shown in Figure 4-19. The measurement was conducted with a microphone array installed 5 m from the rail for a train travelling at the speed of 303.3 km/h. To remove a pressure wave, it was necessary to apply a high-pass filter of 20 Hz as shown in Figure 4-20. Then, the delay-and-sum method was applied to compensate for the positions of the microphones. The weighting function as shown in Figure 4-21, which weighted the measured signals in the high-resolution regions, was applied as shown in Figure 4-22.

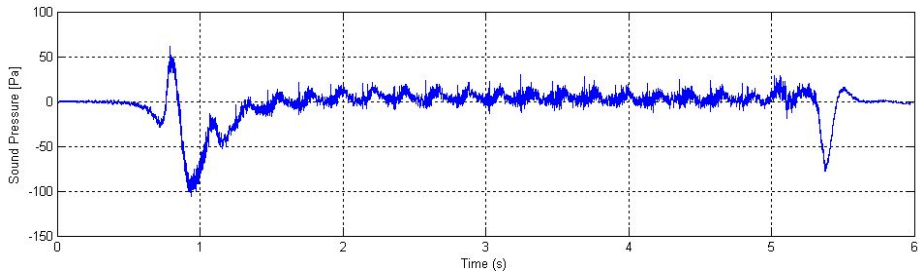


Figure 4-19 Pass-by noise data of high-speed train

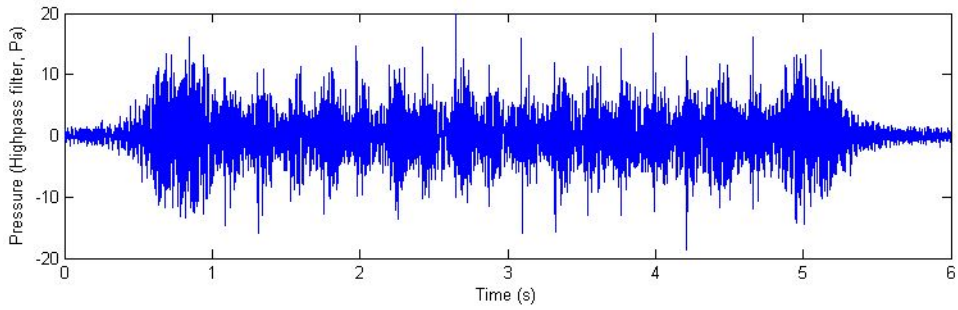


Figure 4-20 20 Hz high-pass filtered signal

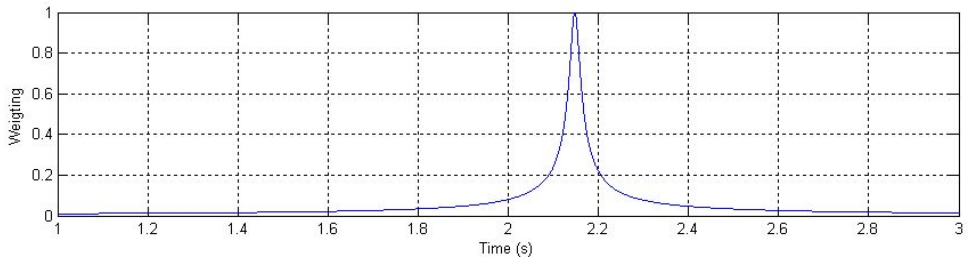


Figure 4-21 Weighting factors at inter-coach spacing

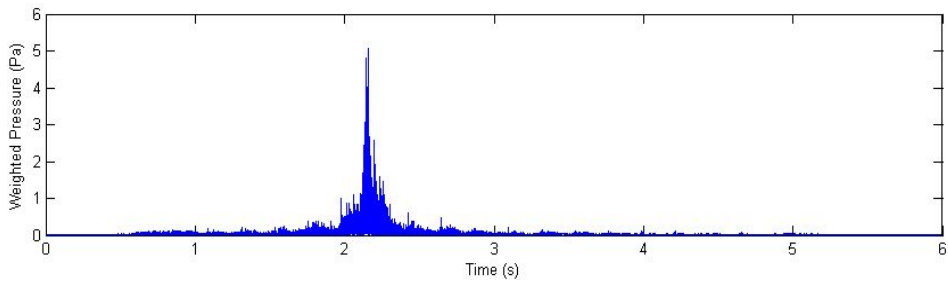


Figure 4-22 Weighted signal at inter-coach spacing

After weighting the data, the Fourier transform was applied and A-weighting was assigned to reflect the characteristics of the audio frequency. The spectrum obtained in this manner showed the characteristics of the noise generated from a specific position of the passing train. The noise characteristics were deduced from the beampower spectrum of each major noise source. The results for bogie and inter-coach are for a single bogie and an inter-coach spacing.

Most aerodynamic noise sources are located on the power cars: the area around the first bogie, the pantograph and its recess, the side walls, the access doors, the louvers, and the front windscreen. Inter-coach spacing, roof antennas, and power cables on the roof are other sources of aerodynamic noise, located on the carrier cars. The turbulent boundary layer noise which develops along the train may become important at very high speeds, 400 km/h, but there is a lack of sufficient knowledge and experimental evidence is missing. However, the two main aerodynamic sources on a high-speed train are the region around the first bogie, and the pantograph and its equipment (insulators,

recess of the pantograph).

Aerodynamic phenomena which can occur in the bogie area are complex.

Because of this complexity, it is useful to implement different kinds of tools to

improve the knowledge of the physical phenomena.

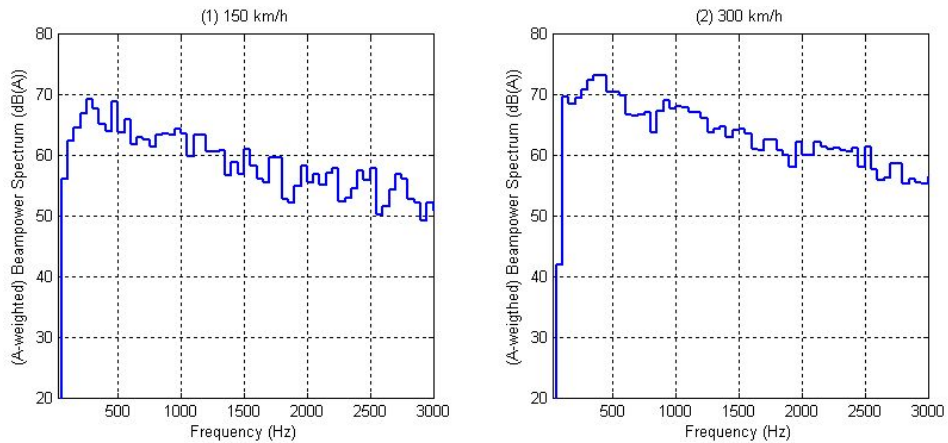


Figure 4-23 Noise characteristics of front nose of power car

The noise from the front nose of the power car was caused by the unsteady airflow induced by the surface shape variations near the leading car nose. Its main noise frequency was less than 400 Hz, and its beampower gradually decreased above this frequency, as shown in Figure 4-23.

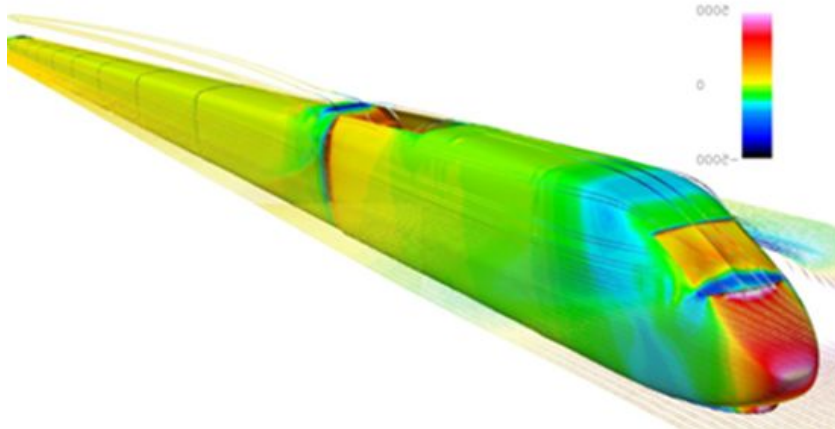


Figure 4-24 Aerodynamic drags of frontal nose of high-speed trains

The speed-up of a high-speed train causes numerical aerodynamic problems such as high level noises at the frontal area as shown in Figure 4-24 [4.21-4.22]. Therefore, the advancements of aerodynamic performance of nose are required.

Noise barriers along the track shield rolling and aerodynamic sources of bogies but do not shield aerodynamic sources on the roof such as pantographs.

As a result, pantograph noise can be significant.

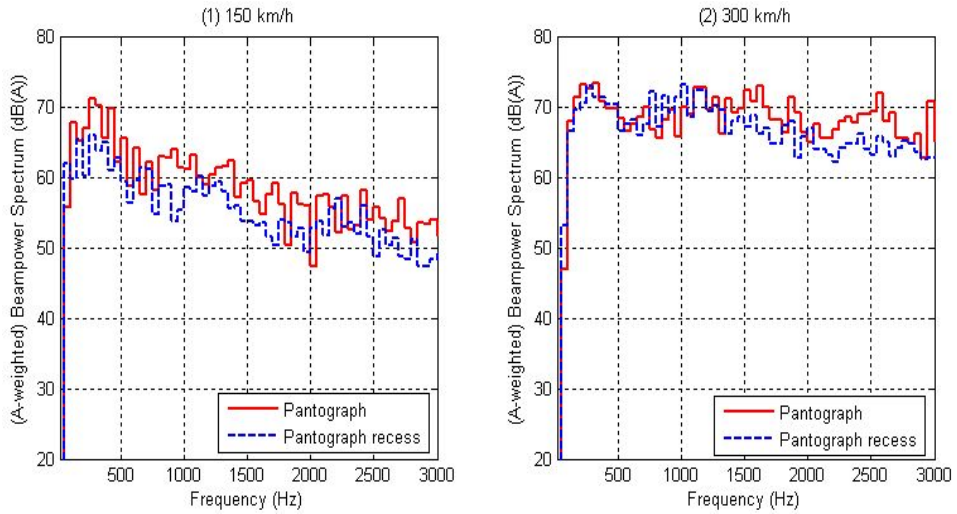


Figure 4-25 Noise characteristics of pantograph sections

One of the major parts of pantograph noise was spark noise generated when the pantograph separated from the overhead wire. Moreover, pantograph radiates only aerodynamic noise. Therefore, the low noise-structure of the pantograph should be considered.

The aerodynamic noise from the pantograph was generated by vortex shedding sound, whereas that from its cover occurred because of unsteady airflows [4.23-4.26]. Their locations were so close that it was difficult to distinguish their individual noise characteristics. Therefore, the noise characteristics of the pantograph and cover of the last trailing car and the pantograph cover and recess in the first power car were deduced. The

pantograph cover section had dominant noise regions less than 1200 Hz, whereas the pantograph area had dominant regions over the entire frequency range, as shown in Figure 4-25.

Pantograph noise generation is mainly owing to vortex shedding around cylinders of the pantograph and the physical phenomena are now quite well understood. Optimization of pantographs has mainly been carried out in Germany and in Japan. A number of experiments were carried out in wind tunnels in Germany for the optimization of cylinder shapes as well as for testing the principle of ribs which allow coherent vortex shedding to be broken up and hence reduce noise generation. Adding the noise contributions from each region of the pantograph that was investigated, the total noise level was reduced by approximately 5 dB in the wind tunnel. Unfortunately, in field tests, the overall reduction of generated noise was not as great as that. As a conclusion, the noise reduction potential for conventional pantographs is limited and new concepts should be considered, including optimization of the pantograph in interaction with its equipment such as insulators. Pantograph

noise in Japan has been reduced by installing covers on the train roof around the pantograph foot region. However, since the pantograph covers themselves generate aerodynamic noise new low-noise pantographs should be developed.

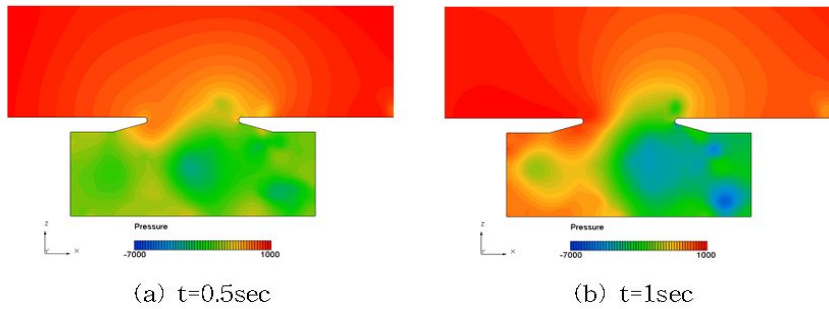


Figure 4-26 Pressure contour in inter-coach spacing

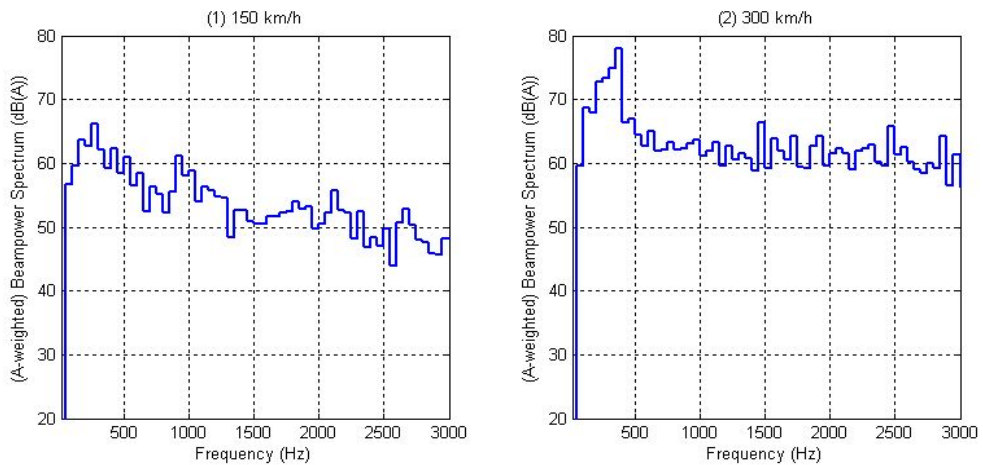


Figure 4-27 Noise characteristics of inter-coach spacing

The noise of the inter-coach spacing was generated from the influence of cavities and mudflaps as shown in Figure 4-26. The inflow of air into the cavity was the main noise generation mechanism [4.27]. Its generating

frequencies were in the low frequency region less than 400 Hz [4.28]. Moreover, it was a tonal sound, as shown in Figure 4-27. The tonal sound from the inter-coach spacing in the low frequency is consistent with previous experimental results .

Furthermore, noise mitigation measures were applied to reduce noise in the inter-coach spacing. At first, side barriers were attached to block air flow of the inter-coach spacing as shown in Figure 4-28. Then, bellow was established in the gangway for increasing transfer path loss of partitions between gangway and inter-coach spacing. Then, noise measurement was conducted with microphones. After analyzing the results, noise reductions about the methods were observed as shown in Figure 4-29. With side barriers in the inter-coach spacing, noise in the cavity was reduced by 8~10 dB at the speed of 300 km/h. This was caused by blocking the influx of air in the cavity. Moreover, with installation of bellows, the interior noise in the gangway was abated by 3~8 dB, which was caused by increasing transfer path losses between outer and interior spaces of the inter-coach spacing. Effective methods were examined for

reducing internal and outer noises in the between-car sections of a high-speed train.



Figure 4-28 Side barriers in inter-coach spacing

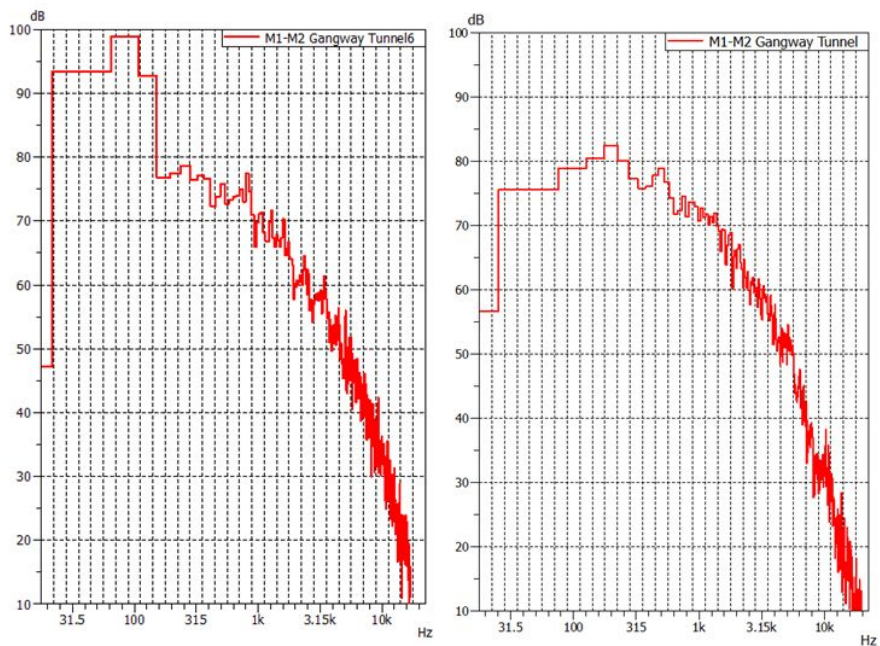


Figure 4-29 Noise reduction in inter-coach spacing

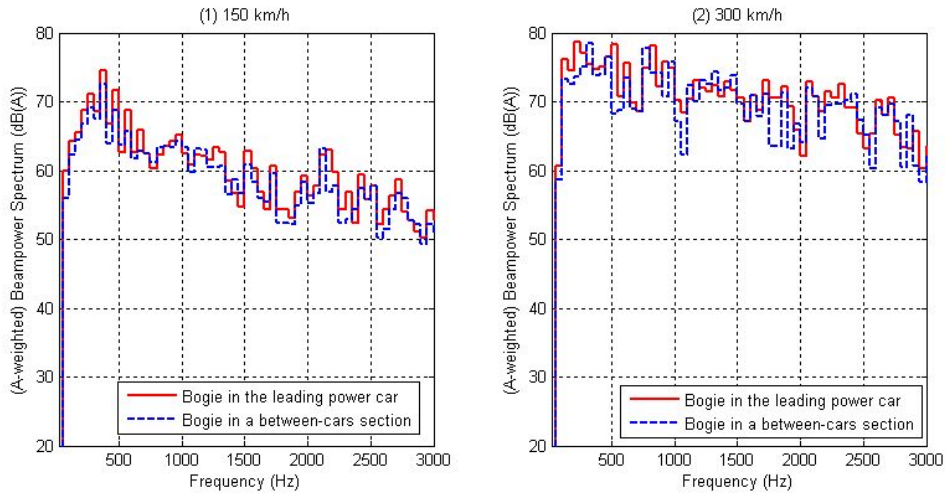


Figure 4-30 Noise characteristics of bogie sections

Finally, the noise characteristics of bogies in the leading power car and a between-cars section were derived [4.29]. The dominant noise of bogies was less than 1000 Hz as shown in Figure 4-30, and this trend is similar to experimental results. However, the rolling noise from the wheels and aerodynamic noise from scattering were generated in a bogie area. Therefore, it is difficult to derive aerodynamic noise of the bogie in the low frequency region. The noise characteristics deduction from the beampower spectrum of each major noise source was summarized in Table 4-1.

Table 4-1 Noise characteristics of main noise sources of high-speed trains at speed of 300 km/h (A-weighted Beampower (dB(A)), Center frequency (500 Hz bandwidth))

	500Hz	1 kHz	1.5 kHz	2 kHz	2.5 kHz	3 kHz
Front nose	71	68	64	62	62	55
Pantograph	70	73	71	66	68	65
Pantograph recess	67	70	68	65	63	62
Inter-coach spacing	68	63	68	62	66	62
Bogie in leading power car	77	75	72	68	64	62
Bogie in between-cars section	76	77	73	67	66	63

From the research, the new method for deducing noise characteristics was verified with moving vehicles. The validated method in this research can be applied to various fields such as equipment in the ships for obtaining effective noise mitigation measures.

5. Conclusions

5.1 Conclusions

In this study, noise source identification was conducted for a moving vehicle. Moreover, a new method for deriving the noise characteristics of the main noise source was proposed, and the method was applied to a high-speed vehicle. The major conclusions drawn from this study are as follows.

- (1) When propagated signal from an arbitrary source was measured by multiple sensors, the output signal should be adjusted according to the positions of the measured sensors.
- (2) It was confirmed that the beamforming method in the time domain was effective for compensating for the Doppler effect.
- (3) To avoid ghost images, the microphone spacing should be less than the wavelength of the frequency.
- (4) The microphone placement in the array is closely related to its resolution.

In this research, the resolution was simulated for rectangular and radial array shapes.

- (5) The maximum sound pressure emitted from the passing-by high-speed train increased with the increase in the driving speed.
- (6) The noise generation of the high-speed train increased exponentially, and the noise characteristics also changed according to the speed increase.
- (7) From the time-history of the sound pressure level during a passing-by of a high-speed train, it was confirmed that the between-car section and bogies were the dominant noise generating areas.
- (8) Both the rolling noise from the bogies and the aerodynamic noise from the pantograph and inter-coach gaps were the main noise source areas of the high-speed train with an increase in speed.
- (9) The resolution improvement in the low frequency region was confirmed by using inverse problem optimization, and this method was found to be effective through practical applications.
- (10) To improve the resolution from the beamformer output, it is important to derive the point spread function. In this dissertation, the point spread functions in the frequency domain were derived from the beampower

values in the time domain.

- (11) The main noise sources of the high-speed train were the front, pantograph, inter-coach spacing, and bogie areas.
- (12) The noise from front of the power car was caused by the unsteady airflow, and its main noise frequency was less than 400 Hz.
- (13) The pantograph cover section had dominant noise regions at frequencies less than 1200 Hz, whereas the pantograph area had dominant regions over the entire frequency range.
- (14) The generating noise frequency of the inter-coach spacing was in the low frequency region less than 400 Hz.
- (15) The noise characteristics of the bogies in the leading power car and between-car section were less than 1000 Hz.

5.2 Future works

The results of this study can be applied to the various fields through the following studies.

- (1) In this research, the characteristics of the main noise sources were determined. I suggest an analysis of the contributions of the main noise sources as future research. In order to analyze the noise contributions at a distance, the transfer function between the main noise sources and the output signal as well as the noise characteristics of the noise source are necessary. The method for obtaining the noise radiation characteristics was proposed in this research; therefore, we can conduct an analysis of the noise contributions at a specific point from the passing-by noise of the high-speed train by using the Green's function as the transfer function.
- (2) The sound visualization technique in this study can be applied to derive the noise sources in a variety of fields. In particular, effective noise reduction measures can be derived through the visualization of equipment in the marine sector.

(3) The resolution improvement technique in this study can be applied to the location search technique in a variety of fields. In particular, the research can be applied to the sophisticated navigation in the shipbuilding industry.

References

- [1.1] UIC (2011), "Evolution of maximum speed on rails", UIC 8th Training on high speed systems.
- [1.2] J. M. Wunderli (2007), "The relation between sound pressure levels of different sources of sound and the velocity of the train", PhD thesis, ETH Zurich.
- [1.3] D.J.Kang, J.W.Lee, J.H.Gu (2007), "Performance test of noise reducers installed on noise barrier", Transactions of the Korean Society for Noise and Vibration Engineering, Vol.17, No.12, pp.1139-1144.
- [1.4] K.Sakurai, K.Mori, T.Masuda (2007), "Development of a noise reduction device for shinkansen sound barriers", JR East Technical Review-No.12, pp.52-57.
- [1.5] T.Ishizuka, K.Fujiwara (2004), "Performance of noise barriers with various edge shapes and acoustical conditions", Applied Acoustics, Vol.65, pp.125-141.
- [1.6] E.V.Haaren, P.H.Van (2000),"Validation of ray acoustics applied for the modeling of noise barriers", Journal of Sound and Vibration, Vol.231, Issue 3, pp. 681-688.
- [1.7] D.J.Thompson (2009), "Railway Noise and Vibration", pp. 6-9.
- [1.8] D.J.Thompson, B.Hemsworth, N. Vincent (1996), "Experimental validation of the TWINS prediction program, Part 1: Method", Journal of Sound and Vibration, Vol.193, pp. 123-135.
- [1.9] B.Dedrichs (2003), "On computational fluid dynamics modeling of cross wind effects for high-speed rolling stock", Proceedings of the institution

of mechanical engineering, Part F. Journal of Rail and Rapid Transit, Vol.217, pp. 203-226.

- [1.10] A.Lauterbach, K.Ehrenfried, S.Kröber, T.Ahlefeldt, S.Loose (2010), "Microphone array measurements on high-speed trains in wind tunnels", Beamforming Conference.
- [1.11] N.Fremion, N.Vincent (2000), "Aerodynamic noise radiated by the intercoach spacing and the bogie of a high-speed train", Journal of Sound and Vibration, Vol.231, Issue 3, pp.577-593.
- [1.12] B.Mauclair (1990), "Noise generated by high-speed trains. New information acquired by SNCF in the field of acoustics owing to the high speed test programme", Proceedings Inter Noise, Vol.90, pp. 371-374.

- [2.1] Y.Wakabayashi, T.Kurita, H.Yamada, M.Horiuchi (2007), "Noise measurement results of Shinkansen high-speed test train", 9th International Workshop on Railway Noise.
- [2.2] N.Yamazaki, T.Takaishi, M.Toyooka, K.Nagakura, A.Sagawa, H.Yano (2007), "Wind tunnel tests on the control of aeroacoustic noise from high speed train", 9th International Workshop on Railway Noise.
- [2.3] N.Fremion, N.Vincent (2000), "Aerodynamic noise radiated by the intercoach spacing and the bogie of a high-speed train", *Journal of Sound and Vibration*, Vol.231, Issue 3, pp.577-593.
- [2.4] J.D.Maynard, E.G.Williams, Y.Lee (1985), "Near-field acoustic holography: I. Theory of generalized holography and the development of NAH", *Journal of the Acoustical Society of America*, Vol.78, Issue 4, pp.1395–1413.
- [2.5] W.A.Veronesi, J.D.Maynard (1987), "Near-field acoustic holography (NAH): II. Holographic reconstruction algorithms and computer implementation", *Journal of the Acoustical Society of America*, Vol.81, Issue 5, pp.1307–1322.
- [2.6] C.Pezerat, Q.Leclere, N.Totaro, M.Pachebat (2009), "Identification of vibration excitations from acoustic measurements using near field acoustic holography and the force analysis technique", *Journal of Sound and Vibration*, Vol.326, Issue 3-5, pp. 540-556.
- [2.7] J.H.Jeon, Y.H. Kim (2008), "Localization of moving periodic impulsive source in a noisy environment", *Mechanical Systems and Signal Processing*, Vol.22. pp. 753-759.
- [2.8] D.H.Johnson, D.E.Dudgeon (1993), "Array signal processing: concepts

- and techniques", Prentice-Hall.
- [2.9] J.J.Christensen, J.Hald (2004), "Technical review – beamforming",
Bruel&Kjeur.
- [2.10] H.Kook, G.B.Moebs, P.Davies, J.S.Bolton (2000) "An efficient
procedure for visualizing the sound field radiated by vehicle during
standardized pass-by tests", Journal of Sound and Vibration, Vol.233,
Issue 1, pp.137–156.
- [2.11] E.Bavu, A.Barry (2009), "Super-resolution imaging of active vibrational
sources using a numerical time-reversal sink", Acta Acoustica, Vol.94,
Issue 5, pp.595-606.
- [2.12] M.Fink, D.Cassereau, A.Derode, C.Prada, P.Roux, M.Tanter,
J.L.Thomas, F.Wu (2000),"Time-reversed acoustics", Report on Progress
in Physics, Vol.63, pp.1933-1995.
- [2.13] Y.Kim, P.A.Nelson (2004), "Optimal regularization for acoustic source
reconstruction by inverse methods", Journal of Sound and Vibration,
Vol.275, Issue 3-5, pp.463-487.
- [2.14] H.G.Choi, A.N.Thite, D.J.Thompson (2007), "Comparison of methods
for parameter selection in Tikhonov regularization with application to
inverse force determination", Journal of Sound and Vibration, Vol.304,
Issue 3-5, pp. 894-917.
- [2.15] Q.Leclerc (2009), "Acoustic imaging using under-determined inverse
approaches: Frequency limitations and optimal regularization", Journal
of Sound and Vibration, Vol.321, Issue 3-5, pp.605-619.
- [2.16] G.H.Golub, C.F.van Loan (1996), "Matrix computations", John Hopkins
University Press, Baltimore.

- [2.17] P.A.Nelson (2001), "A review of some inverse problems in acoustics", International Journal of Acoustics and Vibration, Vol.6, Issue 3, pp.118-134.
- [2.18] C.Hansen (1990), "Discrete Picard condition for discrete ill-posed problems", BIT Numerical Mathematics, Vol.30, Issue 4, pp.658-672.
- [2.19] P.C.Hansen (1998), "Rank-deficient and discrete ill-posed problems", SIAM, Philadelphia.
- [2.20] A.Gerard, A.Berry, P.Masson, Y.Gervais (2007), "Unsteady lift and flow velocity evaluation for subsonic fans using inverse aeroacoustic models", AIAA Journal, Vol.45, Issue 1, pp.98-109.
- [2.21] Germane-French Cooperation Deufrako Annex K (1994), "Noise sources from high-speed guided transport", Final report.
- [2.22] Germane-French Cooperation Deufrako Annex K2 (1999), "Noise sources from high-speed guided transport", Final report.
- [2.23] G.Holzl, P.Fodiman, K.P.Schmitz, M.A.Pallas, B.Barsikow (1994), "Deufrako-2: Localized sound sources on the high-speed vehicles ICE, TGV-A and TR 07", Proceedings of Inter Noise 94 Japan, pp.193-198.
- [2.24] A.Van Beek (2002), "Rail sources-state of the art", Harmonoise report HAR12TR-020118-SNCF10.
- [2.25] J.W.Choi, Y.H.Kim (1995), "Spherical beamforming and MUSIC methods for the estimation of localization and strength of spherical sound sources", Mechanical System and Signal Processing, Vol.98, Issue 4, pp. 569-588.
- [2.26] B.Barsikow, W.F.King III (1988), "On removing the Doppler frequency shift from array measurements of railway noise", Journal of

Sound and Vibration, Vol.120, pp. 190-196.

- [2.27] J.F.Hamet, M-A.Pallas, K.P.Schmitz (1994), "Deufrako-1: Microphone array techniques used to locate acoustic sources on ICE, TGV-A and Transrapid 07", Proceedings of Inter Noise 94 Japan, pp.187-192.
- [2.28] A.Nordborg, J.Wedemann, L.Willenbrink (2000), "Optimum array microphone configuration", Proceedings Inter Noise 2000, France
- [2.29] B.Barsikow (1996), "Experiences with various configurations of microphone arrays used to locate sound sources on railway trains operated by the DB AG", Journal of Sound and Vibration, Vol.193, Issue 1, pp. 283-293.
- [2.30] B.Barsikow, W.F.King III, E.Pfizenmaier (1987), "Wheel/rail noise generated by a high-speed train investigated by a line array of microphones", Journal of Sound and Vibration, Vol.118, Issue 1, pp. 99-122.
- [2.31] M.M.Boone, N.Kinneging, T.Van den Dool (2000), "Two-dimensional noise source imaging with a T-shaped microphone cross array", Journal of the Acoustical Society of America, Vol.108, pp. 2884-2890.
- [2.32] W.F.King III, D.Bechert (1979), "On the sources of wayside noise generated by high-speed trains", Journal of Sound and Vibration, Vol.66, Issue 3, pp. 311-332.
- [2.33] F.Possion, P.E.Gautier, F.Letorneaux (2008), "Noise sources for high speed trains: a review in the TGV case, noise and vibration mitigation for rail transportation systems", Notes on Numerical Fluid Mechanics and Multidisciplinary Design, Vol.99, pp. 71-77.
- [2.34] C.Mellet, F.Letournearux, F.Possion, C.Talotte (2006), "High speed

train noise emission: Lasted investigation of the aerodynamic/rolling noise contribution", *Journal of Sound and Vibration*, Vol.293, Issue 3-5, pp. 535-546

[2.35] Sound View Instruments (2010), "Designing a microphone array system for noise measurements on high-speed trains", KRRRI Technical Note.

[2.36] T.Kitagawa, D.J.Thompson (2006), "Comparison of wheel/rail noise radiation on Japanese railways using the TWINS model and microphone array measurements", *Journal of Sound and Vibration*, Vol.293, Issue 3-5, pp. 469-509.

- [3.1] K.Shin, J.K.Hammond (2008), "Fundamentals of signal processing for sound and vibration engineers", John Wiley & Sons.
- [3.2] T.Brooks, W.Humphreys (1999), "Effect of directional array size on the measurement of airframe noise components", AIAA paper 99-1958.
- [3.3] M.Mosher, M.E.Watts, M.Barnes, J.Bardina (1999), "Microphone array phased processing system (MAPPS): phased array system for acoustic measurements in a tunnel wind", SAE paper 1999-01-5576.
- [3.4] S.Oerlemans, P.Sijtsma (2002), "Determination of absolute levels from phased array measurements using spatial source coherence", Technical Report NLR-TP-2002-226, National Aerospace Laboratory NLR.
- [3.5] U.Michel, S.Funke (2008), "Noise source analysis of an aero-engine with a new inverse method sodix", AIAA paper 2008-2860.
- [3.6] B.Van Veen, K.Buckley (1988), "Beamforming: a versatile approach to spatial filtering", IEEE Signal Processing Magazine, Vol.5, Issue 2, pp. 4-24.
- [3.7] H.Kim, M.Viberg (1996), "Two decades of array signal processing research, the parametric approach", IEEE Signal Processing Magazine, pp. 67-69.
- [3.8] W.S.Liggett Jr. (1972), "Passive sonar processing for noise with unknown covariance structure", The Journal of the Acoustical Society of America, Vol.51, Issue 1, pp. 24-30.
- [3.9] R.Roy, A.Paulraj, T.Kailath (1986), "ESPRIT-a subspace rotation approach to estimation of parameters of cisoids in noise", IEEE Transactions on Acoustics, Speech and Signal Processing, Vol.34, Issue 5, pp. 1340-1342.

- [3.10] J.Capon (1969), "High resolution frequency wave number spectrum analysis", *Processing of the IEEE*, Vol.57, Issue 8, pp. 1408-1418.
- [3.11] J.Li, P.Stoca, Z.Wang (2003), "On robust capon beamforming and diagonal loading", *IEEE Transactions on Signal Processing*, Vol.51, Issue 7, pp. 1702-1715.
- [3.12] R.A.Gramann, J.W.Mocia (1995), "Aeroacoustic measurements in wind tunnels using adaptive beamforming methods", *Journal of the Acoustic Society of America*, Vol.97, pp. 3694-3701.
- [3.13] D.Long (2003), "Acoustic source location in wind tunnel tests via subspace beamforming", *AIAA paper 2003-269*.
- [3.14] Z.Wang, J.Li, P.Stoica, T.Nishida, M.Sheplak (2004), "Constant-beamwidth and constant-powerwidth wideband robust Capon beamformers for acoustic imaging", *Journal of the Acoustical Society of America*, Vol.116, Issue 3, pp.1621-1631.
- [3.15] R.Shimidt (1986), "Multiple emitter location and signal parameter estimation", *IEEE Transactions on Antennas and Propagation*, Vol.34, Issue 3, pp. 276-280.
- [3.16] R.P.Dougherty, R.W.Stoker (1998), "Sidelobe suppression for phased array aeroacoustic measurements", *AIAA paper 98-2242*.
- [3.17] Y.Wang, J.Li, P.Stoica, M.Sheplak, T.Nishida (2004), "Wideband RELAX and wideband CLEAN for aeroacoustic imaging", *Journal of the Acoustical Society of America*, Vol.115, Issue 2, pp.115-757.
- [3.18] P.Sijtsma (2007), "CLEAN based on spatial source coherence", *AIAA paper 2007-3436*.

- [3.19] T.F.Brooks, W.M.Humphreys (2004), "A Deconvolution approach for the mapping of acoustic sources (DAMAS) determined from phased microphone arrays", AIAA paper 2004-2954.
- [3.20] T.F.Brooks, W.M.Humphreys (2006), "Extension of DAMAS phased array processing for spatial coherence determination (DAMAS-C)", AIAA paper 2006-2654.
- [3.21] R.Dougherty (2005), "Extension of DAMAS and benefits and limitations of deconvolution in beam forming", AIAA paper 2005-2961.
- [3.22] K.Ehrenfried, L.Koop (2007), "Comparison of iterative deconvolution algorithms for the mapping of acoustic sources", AIAA Journal, Vol.45, Issue 7, pp. 2005-2961.
- [3.23] T.Yardibi, J.Li, P.Stoica, L.Cattefesta III (2008), "Sparsity constrained deconvolution approaches for acoustic source mapping", Journal of the Acoustical Society of America, Vol.123, Issue 5, pp.123-2631.
- [3.24] T.Suzuki (2006), "Identification of multiple noise sources in low Mach number jets near the peak frequency", The Journal of the Acoustical Society of America, Vol.119, Issue 6, pp. 3649-3659.
- [3.25] T.Suzuki (2008), "Generalized inverse beam-forming algorithm resolving coherent/incoherent, distributed and multipole sources", AIAA paper 2008-2954.
- [3.26] J.W.Choi, Y.H.Kim (1995), "Spherical beamforming and MUSIC methods for the estimation of localization and strength of spherical sound sources", Mechanical System and Signal Processing, Vol.98, Issue 4. pp. 569-588.
- [3.27] P.Stoica, R.Moses (1997), "Introduction to spectral analysis", Prentice-

Hall, Upper Saddle River, NY.

- [3.28] E.Sarradj (2010), "A fast signal subspace approach for the determination of absolute levels from phased microphone array measurements", Journal of Sound and Vibration, Vol.329, Issue 9, pp. 1553-1569.
- [3.29] J.Bardsley, J.Merikosiki, R.Vio. (2008), "The stabilizing properties of nonnegative constraints in least-squares image reconstruction", International Journal of Pure and Applied Mathematics, Vol.43. No.1, pp.95-109.
- [3.30] J.Nocedal, S.J.Wright (1999), "Numerical optimization", Springer.
- [3.31] C.L.Lawson, R.J.Hanson (1974), "Solving least squares problems", Prentice-Hall.

- [4.1] P.J.Remington (1987), "Wheel/rail rolling noise, 1:Theoretical analysis", Journal of the Acoustical Society of America, Vol.81, pp. 1805-1823.
- [4.2] P.J.Remington (1987), "Wheel/rail rolling noise, 2:Validation of the theory", Journal of the Acoustical Society of America, Vol.81, pp. 1824-2832.
- [4.3] D.J.Thompson (1990), "Wheel-rail noise: theoretical modeling of the generation of vibrations", PhD thesis, University of Southampton.
- [4.4] D.J.Thompson (1993), "Wheel-rail noise generation, Part 1: Introduction and interaction model", Journal of Sound and Vibration, Vol.161, pp.387-400.
- [4.5] D.J.Thompson (1993), "Wheel-rail noise generation, Part 2: Wheel vibration", Journal of Sound and Vibration, Vol.161, pp.401-419.
- [4.6] D.J.Thompson (1993), "Wheel-rail noise generation, Part 3: Rail vibration", Journal of Sound and Vibration, Vol.161, pp.421-446.
- [4.7] D.J.Thompson (1993), "Wheel-rail noise generation, Part 4: Contact zone and results", Journal of Sound Vibration, Vol.161, pp.447-466.
- [4.8] D.J.Thompson (1993), "Wheel-rail noise generation, Part 5: Inclusion of wheel rotation", Journal of Sound and Vibration, Vol.161, pp.467-482.
- [4.9] Crespi, R.Gregoire and P.Vinson (1994), "Laser Doppler velocimetry measurements and boundary layer survey on-board the TGV high speed train", Proceeding of World Congress on Railway Research, Paris.
- [4.10] N.Paradot (2001), "Etudes numérique et expérimentale de la résistance a l'avancement d'un train a grande vitesse", PhD thesis, University of Poitiers.
- [4.11] M.J.Lighthill (1952), "On sound generated aerodynamically, 1. General

- theory", Proceedings of the Royal Society of London, A211, 564.
- [4.12] N.Curle (1995), "The influence of solid boundaries upon aerodynamic sound", Proceedings of the Royal Society of London, A231, pp. 505-514.
- [4.13] Ffowcs, Hawking (1969), "Sound generated by turbulence and surface in arbitrary motion", Philophysical Transactions of the Royal Society, A261(1151), pp. 321-342.
- [4.14] E.Le Devehat, C.Talotte, and A.Dugardin (1996), "Aerodynamic noise reduction using a CFD approach based on the prediction of the turbulence production area", MIRA International conference on Vehicle Aerodynamics, Coventry, UK.
- [4.15] T.J.Muller (2002), "Aeroacoustic measurements", Springer, Berlin.
- [4.16] C.Noger, J.C.Patrat, J.Peube, and J.L.Peube (2000), "Aeroacoustical study of the TGV pantograph recess", Journal of Sound and Vibration, 231, pp. 563-575.
- [4.17] Rossiter (1964), "Wind tunnel experiments on the flow over rectangular cavities at subsonic and transonic speeds", Aeronautical Research Council Reports and Memoranda, Technical Report 3438.
- [4.18] N.Yamazaki and T.Takaishi (2007), "Wind tunnel tests on reduction of aeroacoustic noise from car gaps and bogie sections", Quarterly report of RTRI, Railway Technical Research Institute, Tokyo, Japan, 48, pp. 229-235.
- [4.19] H.M.Noh, J.H.Cho, S.Choi, S.Y.Hong (2012), "Noise source localization on high-speed trains by using a microphone array", Journal of the Korean Society for Railway, Vol.15, No.1, pp. 23-28.
- [4.20] Bruel & Kjaer (2004), "Technical Review No.1-Beamforming".

- [4.21] H.Kwon, D.Lee, J.Baek (2000), "An experimental study of aerodynamic drag on high-speed Train", *KSME International Journal*, Vol.14, No.11, pp. 1267-1275.
- [4.22] V. V. Vytla, P. G. Huangy and R. C. Penmetsaz (2000), "Response surface based aerodynamic shape optimization of high speed train nose", 48th AIAA Aerospace Sciences Meeting, Orlando, USA, 4-7 Jan 2000.
- [4.23] T. Kurita, M. Hara, H. Yamada, Y. Wakabayashi, F. Mizushima, H.Satoh and T. Shikama (2009), "Reduction of pantograph noise of high-speed trains," *International Symposium on Speed-up, Safety and Service Technology for Railway and Maglev Systems 2009 (STECH'09)*, Niigata, Japan.
- [4.24] Y. Wakabayashi, T. Kurita and M. Horiuchi (2008), "Development of pantograph noise insulating panels", *JR EAST Technical Review-No.12*.
- [4.25] B.S.Holme, J.B.Dias, B.A.Jaroux, T.Sassa, Y.Ban (1997), "Predicting the wind noise from the pantograph cover of a train," *International Journal for Numerical Methods in Fluids*, Vol. 24, pp. 1307-1319.
- [4.26] T. Kurita, M. Hara, H. Yamada, Y. Wakabayashi, F. Mizushima, H.Satoh and T. Shikama (2009), "Reduction of pantograph noise of high-speed trains," *International Symposium on Speed-up, Safety and Service Technology for Railway and Maglev Systems 2009 (STECH'09)*, Niigata, Japan, 6.16-19.
- [4.27] H. Kook, L. Mongeau (2002), "Analysis of the periodic pressure fluctuations induced by flow over a cavity", *Journal of Sound and Vibration*, Vol.251. Issue 5, pp. 823-846.
- [4.28] M. Inagaki, O. Murata and T. Kondoh (2002), "Numerical prediction of

fluid resonant oscillation at low Mach number", AIAA Journal, 40(9), pp.1823-1829.

[4.29] B.Hemsworth (1979), "Recent developments in wheel/rail noise research", Journal of Sound and Vibration, 66, pp. 103-112.

국문초록

본 연구에서는 고속철도 차량의 주행 시 발생하는 소음을 바탕으로 주요 소음원의 위치를 특정하고, 각 주요 소음원의 음향특성을 도출하는 연구를 수행하였다. 고속철도 차량의 소음원을 도출하기 위해서 빔형성 방법에 기초한 새로운 마이크로폰 어레이를 설계하였다. 어레이의 형상과 분해능에 대한 시뮬레이션을 수행하였으며, 고속철도 차량의 운행 환경을 고려한 효과적인 어레이 형상에 대한 검토를 수행하였다. 설계된 어레이를 바탕으로 다수의 음원을 가진 주행체에 대한 음장가시화 알고리즘을 개발하였으며, 특정 위치에 음원을 부착한 차량을 통해서 검증을 수행하였다. 검증된 방법을 고속철도 차량에 적용하여 전두부, 팬터그래프, 차량 연결부, 차량 하부가 주요 소음원임을 확인하였다. 빔형성 방법은 저주파 영역에서 어레이의 분해능이 떨어지는 한계를 가지고 있으며, 팬터그래프에서는 저주파 소음원들이 분해능보다 가까운 거리에 존재하여 세부적인 소음원을 도출하지 못한다. 이를 해결하기 위해서 개선된 음장가시화 알고리즘을 역문제 최적화를 바탕으로 적용하였다. 특히, 해의 수렴성을 높이기 위해서 빔파위에 대한 변수의 양수화를 적용하였으며, 역문제 방법을 고속철도 차량에 적용하기 위한 반복식을 도출하였다. 본 연구를 통해 기존의 빔형성 방법으로는 명확한 구분이 불가능했던 고속철도 차량의 팬터그래프의 소음원을 분리하였다. 또한 각 주요 소음원에 대한 소음

특성을 도출하는 연구를 수행하였다. 설계된 어레이의 거리에 따른 분해능 저감을 적용한 가중치 함수를 통해서 분해능이 높은 영역에서 높은 가중치를 가질 수 있도록 하였다. 도출된 가중치 함수를 측정 신호에 적용하고, 주파수 변환을 통해서 주요 소음원에 대한 특성을 도출하였다. 본 연구를 통해서 다음과 같은 결론을 도출하였다. 차량의 전두부에서 발생하는 소음은 주로 저주파 영역임을 확인하였다. 그리고 팬터그래프에서는 열린 상태에서 접힌 상태보다 고주파 영역에서 소음이 존재함을 확인하였다. 차량 연결부에서는 저주파 영역에서 토널 소음이 발생함을 확인하였다. 차량 하부에서는 차륜과 레일의 접촉에 의한 소음과 공력에 의한 유동 소음으로 인해서 전 주파수 영역에서 높은 소음이 발생함을 확인하였다. 끝으로 본 연구에서 도출된 주요 소음원에 대한 음향특성을 바탕으로 효과적인 소음저감방안을 제시하였다.

주요어 : 고속철도차량, 마이크로폰 어레이, 빔형성, 역문제 최적화, 음향특성도출, 소음저감방안

학 번 : 2009-30282